UCRL-ID-120829

Evaluated Cross-Section Libraries and Kerma Factors for Neutrons Up to 100 MeV on ^{12}C

M. B. Chadwick
M. Blann
L. Cox
P. G. Young
M. Meigooni

April 11, 1995

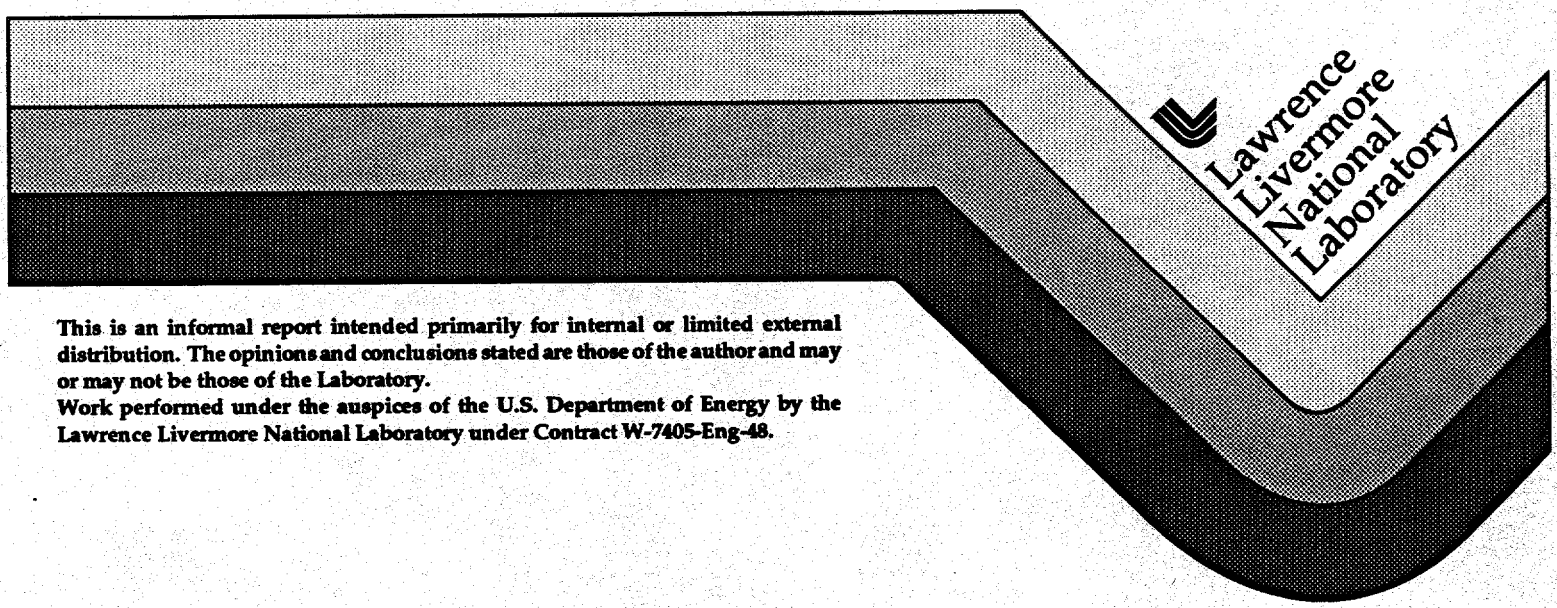

Work performed under the auspices of the U.S. Department of Energy by the Lawrence Livermore National Laboratory under Contract W-7405-Eng-48.

DISCLAIMER

Portions of this document may be illegible in electronic image products. Images are produced from the best available original document.

April 11, 1995

Evaluated cross-section libraries and kerma factors for neutrons up to 100 MeV on ^{12}C

M. B. Chadwick, M. Blann, L. Cox
Nuclear Data Group, Lawrence Livermore National Laboratory, Livermore, CA 94550

P.G. Young
Theoretical Division, Los Alamos National Laboratory, Los Alamos, NM 87545

A. Meigooni
University of Kentucky, Department of Radiation Medicine, Lexington, KY 40536

Abstract

A program is being carried out at Lawrence Livermore National Laboratory to develop high-energy evaluated nuclear data libraries for use in Monte Carlo simulations of cancer radiation therapy. In this report we describe evaluated cross sections and kerma factors for neutrons with incident energies up to 100 MeV on ^{12}C; in subsequent reports we shall describe our high-energy libraries for neutrons on ^{14}N, ^{16}O, ^{31}P and ^{40}Ca, as well as accelerator collimator and shielding materials. The aim of this effort is to incorporate advanced nuclear physics modeling methods, with new experimental measurements, to generate cross section libraries needed for an accurate simulation of dose deposition in fast neutron therapy.

The evaluated libraries are based mainly on nuclear model calculations, benchmarked to experimental measurements where they exist. We use the GNASH code system, which includes Hauser-Feshbach, preequilibrium, and direct reaction mechanisms. The libraries tabulate elastic and nonelastic cross sections, angle-energy correlated production spectra for light ejectiles with A$\leq$4, and kinetic energies given to light ejectiles and heavy recoil fragments. The major steps involved in this effort are: (1) development and validation of nuclear models for incident energies up to 100 MeV; (2) collation of experimental measurements, including new results from Louvain-la-Nueve and Los Alamos; (3) extension of the Livermore ENDL formats for representing high-energy data; (4) calculation and evaluation of nuclear data; and (5) validation of the libraries. We describe the evaluations in detail, with particular emphasis on our new high-energy modeling developments. Our evaluations agree well with experimental measurements of integrated and differential cross sections. We compare our results with the recent ENDF/B-VI evaluation which extends up to 32 MeV. We also compare kerma factors resulting from our evaluated microscopic cross sections with measurements, providing an important integral benchmarking of the libraries. The evaluated libraries are described and illustrated in detail.

GH

Contents

List of Tables

List of Figures

Evaluated cross-section libraries and kerma factors for neutrons up to 100 MeV on ^{12}C

M. B. Chadwick, M. Blann, L. Cox
Nuclear Data Group, Lawrence Livermore National Laboratory, Livermore, CA 94550

P.G. Young
Theoretical Division, Los Alamos National Laboratory, Los Alamos, NM 87545

A. Meigooni
University of Kentucky, Department of Radiation Medicine, Lexington, KY 40536

Abstract

A program is being carried out at Lawrence Livermore National Laboratory to develop high-energy evaluated nuclear data libraries for use in Monte Carlo simulations of cancer radiation therapy. In this report we describe evaluated cross sections and kerma factors for neutrons with incident energies up to 100 MeV on ^{12}C; in subsequent reports we shall describe our high-energy libraries for neutrons on ^{14}N, ^{16}O, ^{31}P and ^{40}Ca, as well as accelerator collimator and shielding materials. The aim of this effort is to incorporate advanced nuclear physics modeling methods, with new experimental measurements, to generate cross section libraries needed for an accurate simulation of dose deposition in fast neutron therapy.

The evaluated libraries are based mainly on nuclear model calculations, benchmarked to experimental measurements where they exist. We use the GNASH code system, which includes Hauser-Feshbach, preequilibrium, and direct reaction mechanisms. The libraries tabulate elastic and nonelastic cross sections, angle-energy correlated production spectra for light ejectiles with $A \leq 4$, and kinetic energies given to light ejectiles and heavy recoil fragments. The major steps involved in this effort are: (1) development and validation of nuclear models for incident energies up to 100 MeV; (2) collation of experimental measurements, including new results from Louvain-la-Nueve and Los Alamos; (3) extension of the Livermore ENDL formats for representing high-energy data; (4) calculation and evaluation of nuclear data; and (5) validation of the libraries. We describe the evaluations in detail, with particular emphasis on our new high-energy modeling developments. Our evaluations agree well with experimental measurements of integrated and differential cross sections. We compare our results with the recent ENDF/B-VI evaluation which extends up to 32 MeV. We also compare kerma factors resulting from our evaluated microscopic cross sections with measurements, providing an important integral benchmarking of the libraries. The evaluated libraries are described and illustrated in detail.

1 Introduction

The Lawrence Livermore National Laboratory Medical Applications Project is developing an all-particle Monte Carlo transport code for calculating and optimizing absorbed dose in cancer radiotherapy [1]. This code, called PEREGRINE, transports neutrons, photons and charged particles in a fully coupled manner, and can be used for simulating the effects of radiation beams on the dose delivered to a patient. The transport is performed through a three-dimensional mesh obtained from a CT-scan of the patient, and the calculated dose distributions can be used to optimize the dose delivered to a tumor.

For this project, neutron cross sections on biologically important elements are needed for incident energies up to 70 MeV, the clinical energy currently being used in most fast neutron therapy centers. In this report we describe work performed by the LLNL Nuclear Data Group to extend the Livermore evaluated nuclear data libraries from 20 MeV up to 100 MeV, for ^{12}C. In subsequent reports we will describe our evaluated libraries for neutrons on ^{14}N, ^{16}O, ^{31}P, and ^{40}Ca, as well as structural materials used in accelerator collimators and shields. Additionally, we shall describe the extension of these libraries up to 250 MeV, for incident neutrons and protons, for proton radiation therapy applications.

Most modern fast neutron therapy facilities use a ^{9}Be(p,n) source reaction, which produces a broad spectrum of neutrons with energies up to 70 MeV. In a recent (1992) review of the status of nuclear data for use in neutron therapy [7], White *et al.* emphasized that with the exception of hydrogen, sufficiently accurate nuclear data does not yet exist in this energy range to allow neutron therapy to reach its full potential. Since standard man consists (by mass) of hydrogen (10%), carbon (18%), nitrogen (3%), and oxygen (65%), and various trace elements (4%), an accurate understanding of neutron nuclear reactions on carbon is essential. As natural carbon consists of only 1.1% ^{13}C, the present work for ^{12}C can be used for natural carbon. Our work aims to improve the evaluated nuclear data for carbon, by using results from recent experimental measurements and developments in model calculation capabilities, to produce data libraries which can be utilized in radiation transport calculations.

Since there are only a few experimental measurements of neutron reactions on biologically-important elements for energies between 20 and 100 MeV, we have based our evaluations mainly on the results of nuclear model calculations, benchmarked to measurements where they exist. To do this, we have developed and applied the GNASH modeling code [3], which uses Hauser-Feshbach theory for equilibrium decay and preequilibrium models for fast-particle emissions. Our theoretical efforts, described in Sec. 3, have concentrated on improvements to the modeling of reaction processes that become important at higher energies, particularly multiple preequilibrium emission, angular momentum effects in preequilibrium reactions, and a physical

basis for continuum angular distribution systematics. We have also developed the ALICE modeling code [4] for modeling biologically-important reactions by using improved level densities and optical models, and including a phenomenological model for preequilibrium deuteron emission.

With these nuclear model codes, as well as a version of GNASH that we have developed which implements the Feshbach-Kerman-Koonin quantum mechanical preequilibrium theory (FKK-GNASH), we have compared calculated cross section predictions with experimental measurements. These comparisons, described in Ref. [5], allowed us to assess the capabilities of these different codes, and assess the uncertainties involved in the model's predictions. With the ALICE code we were able to easily and quickly produce calculated cross sections which describe the measurements fairly well [5]. The GNASH and FKK-GNASH calculations required a more detailed input (such as low-lying nuclear levels, inelastic cross sections from coupled-channels calculations, *etc.*), and also generally described the available measurements well. From these comparisons we have selected the GNASH code for generating our evaluated libraries, since this code allows the most detailed description of the reactions, and explicitly includes the effects of low-lying nuclear level spacings on the calculated spectra. We have, however, pre-evaluated the primary preequilibrium spectra for the various ejectile types by considering the results of the GNASH, FKK-GNASH, and ALICE calculations as well as experimental data. These pre-evaluated spectra are then used as an input into our GNASH calculations for producing the evaluated libraries. This new approach to nuclear data evaluation maintains the advantages of using a model code to generate the libraries (such as ensuring energy and flux conservation), while optimizing the agreement with the experimental measurements where they exist.

Instead of using evaluated nuclear data libraries above 20 MeV, many previous radiation transport analyses use nuclear modeling and transport codes to calculate the nuclear reactions "on the fly" at higher energies, and only use evaluated cross section libraries when the energy drops below 20 MeV. But often the physical assumptions used in these calculations are not valid until the incident energy exceeds a few hundred MeV. In particular, the approximations made in intranuclear cascade (INC) calculations are suspect at energies below 100 MeV. In contrast, our approach is to generate evaluated cross section libraries up to 100 MeV, using the most recent and accurate nuclear models and codes which are extensively benchmarked to experimental measurements. By carefully ensuring that the model calculations are consistent with the existing measured cross sections, state of the art evaluated libraries can be produced over the whole energy range. Additionally, the libraries can be easily modified as new experimental measurements or improved models become available.

Considerable effort has been devoted to validation of the cross section libraries, to

ensure that they represent an accurate description of the existing experimental measurements, while providing a comprehensive and consistent description of all reaction decay channels. In Sec. 6 we show our evaluated results compared to existing experimental cross section measurements. Furthermore, we compare the kerma (an acronym for *kinetic energy released in matter*) calculated from our microscopic cross section evaluations with experimental kerma values. Such integral benchmarking provides a stringent check on the accuracy of our evaluated libraries, and since they are being used for calculating absorbed dose an accurate description of the kerma is essential.

In Sec. 5 we describe a new ENDL format suitable for high-energy data libraries in which the angle-energy correlated inclusive emission spectra are tabulated. We have transformed the existing Livermore ENDL evaluated libraries (for energies below 20 MeV) into this new production cross section format, and have matched the old and new libraries at 20 MeV to produce evaluated libraries data from zero to 100 MeV. The ENDL libraries below 20 MeV developed by Howerton [6] have been shown to provide an excellent description of measured total kerma factors [6, 7] and have been extensively used and benchmarked in radiation transport calculations.

In Sec. 2 we describe our general evaluation methods, and compare our approaches to those of previous calculational analyses of reactions on biologically-important elements above 20 MeV. We describe how the methods used in this work differ from those used in other existing evaluations (evaluated libraries above 20 MeV that can be utilized in transport calculations have been produced by Axton *et al.* [8, 9], Brenner and Prael [10], Pearlstein [11], and Young *et al.* (1990)). Section. 3 presents a detailed description of the nuclear theory and models we use. We emphasize new theoretical capabilities that we have developed for an improved modeling of high-energy reactions. In Sec. 4 we describe our method for calculating kerma factors, particularly the approach we have implemented for determining the nonelastic recoil kerma based on energy balance. In Sec. 5 we describe the new ENDL formats which are suitable for high-energy evaluated nuclear data. In Sec. 6 we give a detailed description of the results of our evaluation, including comparisons with experimental measurements of total, reaction, and elastic cross section, angle-integrated and double-differential emission spectra, and kerma factors. In Sec. 7 we compare our results for various exclusive reactions compared with measurements and with the results of the ENDF/B-VI evaluation, which extends up to 32 MeV. We argue that in the 20-32 MeV region some of the ENDF/B-VI evaluation cross sections are unjustified, and the resulting ENDF/B-VI total kerma factor is too high. A summary and a description of directions and needs for future work are given in Sec. 8.

2 Evaluation Methods

2.1 Evaluation Techniques Used in This Work

2.1.1 General features of the evaluated libraries

For incident energies above 20 MeV the number of possible exclusive reactions following the interaction of a neutron with a carbon nucleus becomes very large. Rather than representing each possible reaction separately, we tabulate only the corresponding inclusive emission spectra of the particles which need to be transported in the Monte Carlo calculations (gammas, and light particles with $A \leq 4$), as well as the total kinetic energy given to heavier charged particles which is assumed to be deposited locally. This representation of the data is adequate for Monte Carlo calculations of radiation transport and absorbed dose. In the future, if applications such as microdosimetry require a description of the energy deposited by all types of nonelastic recoils, we can extend the libraries to include this information.

The libraries are fully angle-energy correlated, and describe the emission spectra at various angles, all in the laboratory frame of reference, facilitating straightforward comparisons with measurements. Tabulating the inclusive production cross sections in evaluated files above 20 MeV was first introduced in the Los Alamos evaluations [12], and is recommended by the Nuclear Energy Agency of the OECD in its intermediate energy data activities [13]. We have omitted triton and helium-3 emission reactions since measurements show these cross sections to be small. This does not imply that our calculated total kerma factor will be underestimated, since kinetic energy to these channels gets redistributed. Trial calculations confirmed this, for including triton emission did not significantly change our total calculated kerma factors.

The evaluations are based mainly on model calculations using the GNASH code system [3], benchmarked to available experimental data. But other reaction model codes were also used in this work: optical model calculations were performed with the ECIS79 [14] and SCAT2 [15] codes; and when evaluating preequilibrium cross sections we considered the results from the ALICE [4], GNASH [3], and FKK-GNASH [16] codes. There are a number of advantages to using nuclear theory and model calculations to produce evaluated cross section libraries: (1) The model input parameters can be adjusted (within the uncertainty ranges to which they are known) to optimize agreement with experimental data at incident energies where measurements have been made. The calculations then provide a useful way to interpolate and extrapolate to other energies; (2) Model calculations enable evaluated libraries to be generated for all reaction products in a fully consistent way, automatically conserving energy, unitarity, spin, and parity; and (3) The large amount of information needed in the evaluated files to describe the production cross sections of different ejectile

types at various incident and emission energies, and angles, can easily be generated from the results of model calculations. As well as enabling the branching ratios for all the (large number of) decay sequences to be calculated, the model calculations automatically incorporate the effects of Q-values and nuclear structure.

2.1.2 Experimental data used in the evaluation

There are only a limited number of experimental measurements of inclusive emission spectra for neutrons on ^{12}C in the 20-100 MeV range: the UC-Davis group has measured charged-particle production cross sections at incident neutron energies of 27, 40 and 60 MeV. [17, 18]; the Louvain-la-Neuve group have recently measured charged-particle production cross sections for ^{12}C at 43, 63, and 73 MeV [19]; and the Los Alamos group have measured alpha production cross sections for ^{12}C using the white neutron source at LAMPF/WNR, for energies up to 40 MeV [20]. There are also (unpublished) Los Alamos $(n, xn\gamma)$ measurements by Auchampaugh and Wender [21] at 60 MeV which we used to benchmark our gamma-production calculations. Additionally, we have made use of the Bertrand and Peelle (p, xp) measurements [22] on ^{12}C at 40 and 60 MeV, since at the higher emission energies (above the Coulomb-barrier) charge independence implies that these cross sections should be similar to those for (n, xn) reactions. We show these various experimental data sets in Secs. 6.3 – 6.6, compared with our evaluations.

There are numerous experimental measurements of the total, elastic, and reaction cross sections, and we show these in Sec. 6.1. The optical model parameters we use have been optimized to describe these data. Full details of these measurements are given in Sec. 3.2. However, we note here that our work has benefitted significantly from the recent high-accuracy total cross section measurements by Finlay et al. [23] at Los Alamos.

Table I below summarizes the experimental data used in this evaluation, in some cases pointing to other places in this report where the data is shown in more detail.

2.1.3 Major steps involved in the evaluations

Some of the major steps involved in this evaluation work are:

Experimental data:

- A significant amount of unpublished (to date) experimental data was obtained from J. Romero of UC-Davis [26](angle-integrated production data from their measurements), R. Haight, S. Sterbenz and T. Lee of Los Alamos National Laboratory [27] (alpha production data), and J.P. Meulders of Louvain-la-Neuve [28](charged-particle production data). This data was utilized in addition to those summarized in Table I

Reaction type	Citation to experimental measurement
Total	See Fig. 5
Elastic	See Table V
Nonelastic	See Table VI
Inelastic neutron scattering	See Figs. 30, 31
Charged particle production	27, 40, 61 MeV UC-Davis data [17, 18] (Figs. 14-20)
	43, 63, 73 MeV Louvain-la-Neuve data [19] (Figs. 14-20)
Alpha particle production	20-40 MeV Los Alamos data [20] (Figs. 14-20)
Gamma-ray production	60 MeV Los Alamos measurement [21], see Fig. 22
$(n, n'3\alpha)$	Antolkovic [24], see Fig. 28
$(n, 2n)$	See Fig. 29
Spallation data	Harrison *et al.* [25] 75 MeV proton data, see Fig. 13
(p, xp)	Bertrand and Peelle [22], see Fig. 21

Table I: Summary of experimental cross section data guiding this evaluation

Model calculations and evaluation:

- Perform optical model analyses for n, p, d, α projectiles and generate elastic and inelastic (coupled-channels) scattering cross sections and particle transmission coefficients.
- Build a database of low-lying nuclear levels for all nuclides which can be produced, for use in Hauser-Feshbach and preequilibrium calculations.
- Perform level density analyses for all nuclides that can be populated, to match continuously a continuum statistical level density description on to the experimental low-lying levels.
- Perform preequilibrium reaction calculations using a variety of nuclear models for comparison purposes: the exciton model (using GNASH); the hybrid model (using ALICE); and the FKK theory (using FKK-GNASH). On the basis of these calculations, and measured cross sections, evaluate the primary preequilibrium spectra.
- Use the GNASH code to generate production cross sections based on primary and multiple preequilibrium, and sequential equilibrium decays using Hauser-Feshbach theory.
- Use the Kalbach systematics [29] to give inelastic angular distributions, and transform the double-differential cross sections to the laboratory frame assuming 2-body kinematics.

- Generate ENDL format cross section and average energy deposition library files.

Benchmarking and validation:

- Compare evaluations against all existing experimental measurements of cross sections and kerma factors.
- Use graphical computational tools to visualize the (large amount of) evaluated data.

2.2 Comparison With Previous Calculational Approaches

A number of previous papers have presented calculations of neutron reactions with carbon above 20 MeV. Here we briefly discuss these works and compare the calculational methods used with our approach. Kerma factors resulting from these calculated cross sections are described in detail in Sec. 6.7, where we compare them with our calculated kerma factors, and with experimental measurements.

Calculations that have been performed can be classified into four categories: (1) Intranuclear cascade calculations (INC) with either an evaporation or a Fermi break-up description of compound nucleus decay (included here is work of Alsmiller and Barish [30], Behrooz and Watt [31], Brenner and Prael [10], Morstin *et al.* [32], and Wells [33]); (2) Preequilibrium model calculations with direct reactions and a Hauser-Feshbach or Weisskopf-Ewing (evaporation) description of compound nucleus decay (included here is the present work, and those of Dimbylow [34], Herling *et al.* [35] and Young *et al.* [12]), and the various preliminary model calculations we described in Ref. [5] ; (3) methods currently being implemented by Watanabe *et al.* [36] using a Monte Carlo simulation code where decay branching ratios must be input and adjusted to optimize agreement with experiments (similar to Antolkovic's approach [37]); and (4) extrapolations of evaluated nuclear data bases, originally containing data up to 20 MeV (the work of Caswell *et al.* [38], and Axton [8]).

The INC methods in category (1) above have in many cases provided a useful tool to analyze reactions above 20 MeV. While the physical assumptions made in these models do not hold well below 100 MeV, numerous analyses have shown that they can provide a surprisingly good description of experimental measurements at these energies. However, of the above-mentioned INC calculations, many were performed prior to the UC-Davis experimental measurements, and it is only the (very comprehensive) work by Brenner and Prael [10] which makes comparisons with experimental charged-particle production cross sections and spectra. As we will describe in more detail later, the Brenner and Prael calculations agree rather well with the UC-Davis measurements when a direct pick-up contribution was added to their INC predictions, though their total kerma for neutrons on carbon appears somewhat too

low. They did not include elastic scattering or inelastic coupled-channels scattering to low-lying collective states in their analyses, and did not present results for gamma-ray production.

Category (2) above includes calculations that use Hauser-Feshbach theory with preequilibrium and direct reaction corrections, as used in this work. Dimbylow [34] modeled neutron reactions on a range of biologically-important nuclei, for incident energies to 60 MeV. An early version of the GNASH code was used, and the model calculations were compared against the UC-Davis cross section and kerma measurements. Even though details of the preequilibrium spectral shapes were often not described well, the resulting kerma factors were modeled fairly accurately. The calculations performed by Herling and Bassel [35] used similar techniques, though their results compared poorly with measurements. More recently, Young *et al.* [12] performed model calculations using the GNASH code for a range of target nuclei (including carbon and oxygen), for incident neutron and proton energies to 100 MeV. The GNASH code was developed and benchmarked for modeling reactions up to 100 MeV. Our work has made use of these developments, though further improvements (described in this report) have been made since then. The scale of the Los Alamos project prohibited large-scale comparisons with experimental production cross sections on carbon and oxygen. Also, the energy depositions (kerma) from these libraries were not described since their use was primarily for modeling the transported particles.

The method of Watanabe *et al.* [36], noted in (3) above, takes the neutron detector simulation code SCINFUL and applies Monte Carlo techniques to determine break-up cross sections. This approach uses experimental cross section measurements as an input to determine the branching ratios for the various possible decay sequences. Results from the analysis were presented at the 1994 conference on Nuclear Data for Science and Technology at Gatlinburg. To date, calculated charged-particle production cross sections and emission spectra for incident energies above 20 MeV have not been reported. It will be easier to assess the usefulness of this method once such results are presented. The kerma factors reported agree well with those obtained from the UC-Davis measurements [18], though they overpredict the direct total kerma measurements of Schrewe [39].

The works in category (4) above (Caswell *et al.* [38] and Axton [8]) extended the evaluated ENDF libraries beyond 20 MeV, using results from optical model analyses to obtain the total, elastic, and nonelastic cross sections. But as the authors themselves attest, many of the partial nonelastic cross section extrapolations are not based on either model calculations or experimental data and must be considered speculative. The total kerma resulting from these calculations significantly overestimates measurements in the 20-30 MeV range, and we therefore conclude that model calculations provide a more accurate determination of cross sections and energy depositions here. The recent report by Axton [8] detailing his evaluation up to 32 MeV is extremely

comprehensive, and is a useful source of references to experimental measurements. Later, in Sec. 7, we compare our evaluation against Axton's work, which has been incorporated into the ENDF/B-VI evaluation together with the work of Fu and Perey below 20 MeV [9].

In addition to these works, a recent evaluation by Pearlstein [11] for neutrons on carbon for energies up to 10 GeV has been included into the ENDF/B-VI "high-energy" evaluated libraries. This evaluation is based mainly on the ENDF/B-VI evaluation below 32 MeV, and uses the LAHET INC code with Fermi break-up to generate the higher energy data.

It is worth addressing here a criticism that Brenner *et al.* [41] have made of evaporation models for light nuclei. They argued that non-statistical features in light-nuclei (such as the wide-spacing of levels which extends up to a relatively high excitation energy) makes the use of statistical level density expressions in evaporation models inappropriate. Instead, they use a Fermi break-up model which partitions the break-up mechanisms according to phase space estimates. Our present work uses a Hauser-Feshbach equilibrium decay prescription in which low-lying nuclear levels are specifically accounted for using modern nuclear level schemes including spins and parities. As we describe in Sec. 3.5.2, a statistical level density expression is only used when the nuclear excitation energy is sufficiently high for it to be valid (see, for instance, Fig. 3). Therefore our approach does include a detailed description of the nuclear structure specific to each nuclide, and is not subject to Brenner's criticism. The good agreement that we present in Sec. 6 between our calculations and measured emission spectra supports the validity of our approach. In Ref. [5] we presented some calculations using the ALICE code, which applies preequilibrium and evaporation theories, and uses a statistical level density description at all energies. These calculations often accounted for measurements well, and indicate that such statistical descriptions often describe data more accurately than one might expect.

A recent international code intercomparison [42] organized by the Nuclear Energy Agency (NEA) of the Organization for Economic Cooperation and Development (OECD) assessed the accuracy of various codes that can be used for modeling nuclear reactions above 20 MeV. Participants calculated (p, xn) and (p, xp) reactions on lead and zirconium targets, for a range of incident energies between 25 MeV and 1 GeV, and the results were compared against experimental double-differential emission spectra. This intercomparison concluded that the most accurate codes for describing reactions below 250 MeV are GNASH, FKK-GNASH, and ALICE - the modeling codes that we use in this work. This provides further confidence in the modeling techniques that we use to generate the libraries.

Unlike many of the above works (with the exception of Brenner and Prael, and Dimbylow) our work provides comprehensive comparisons with experimental emission spectra and kerma factors. We also benefit from additional new measurements from

Los Alamos and Louvain-la-Neuve with which we can benchmark our calculations.

3 Nuclear Theory and Model Developments

3.1 Introduction

In this section we describe the nuclear reaction models used to describe the break-up processes following the interaction of a fast neutron with a light nucleus. We emphasize new developments that we have made for improved modeling of reactions at energies up to 100 MeV.

The nuclear models initially incorporated into the GNASH code were developed and optimized for analyses below 20 MeV. A recent program at Los Alamos [12] extended the applicability of these models up to 100 MeV, concentrating upon extensions of optical model analyses to higher energies, nuclear level densities for higher excitation energies, and improved preequilibrium modeling with the semiclassical exciton model. In recent years through a Livermore – Los Alamos collaboration, we have further improved the GNASH high-energy modeling capabilities. Our development efforts have centered upon the inclusion of multiple preequilibrium processes [43], a new theory for including angular momentum effects in preequilibrium reactions [44] which is important for correctly predicting discrete gamma-ray production cross sections, and we have developed the quantum mechanical multistep theory of Feshbach, Kerman, and Koonin (FKK) [45] for use in nuclear data applications [16, 46, 47, 48, 49].

As a means of introducing the various nuclear reaction models we use, we show in Fig. 1 our calculated angle-integrated neutron emission spectrum at 80 MeV. This illustrative example shows the contributions from primary and multiple preequilibrium processes, as well as the total inclusive spectrum. For clarity we do not show the elastic scattered neutrons. The impact of compound nucleus emission at lower energies, and direct inelastic neutron scattering at high energies on the total inclusive spectrum is also clear. This spectrum is not, in fact, part of our evaluated library since the library cross sections are all in the laboratory frame of reference. The results in Fig 1 come from our GNASH calculation, in the channel energy frame (the center of mass kinetic energy of ejectile plus residual nucleus), before it is transformed into the lab.

We note some features of the various contributing reaction mechanisms seen in Fig 1. At the highest emission energies, the importance of neutron inelastic scattering to the 2+ (4.4 MeV) and 3- (9.6 MeV) is evident, and we describe in Sec. 3.2 how we calculate these cross sections using a coupled-channel optical model. The long hard tail in the neutron spectrum is due mainly to primary preequilibrium emission, described in Sec. 3.3, though multiple preequilibrium emission, described in Sec. 3.4. also results in a significant amount of high-energy ejectiles. At low energies, the large increase in the spectrum comes from evaporation (compound nucleus) processes. modeled using the Hauser-Feshbach theory (see Sec. 3.5. The structure seen at the

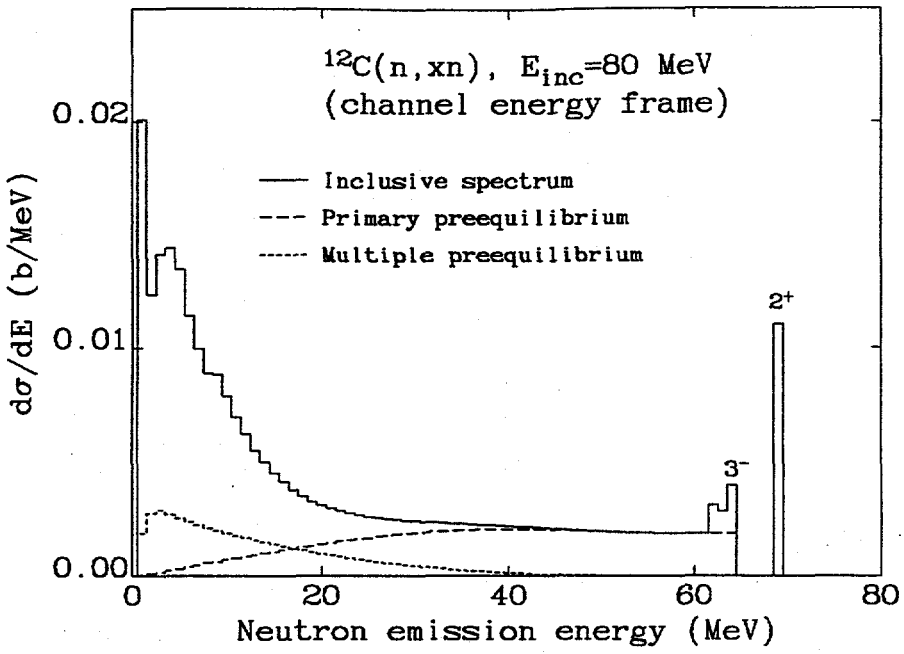

Figure 1: Calculated 80 MeV ^{12}C(n,xn) angle-integrated emission spectrum, with contributions from primary and multiple preequilibrium emission. Direct scattering to the 2+ (4.4 MeV) and 3- (9.6 MeV) states are particularly evident.

lowest and highest energies is a direct consequence of our use of experimental nuclear level information. The peak seen in the emission energy bin at 1 MeV comes mainly from the decay of nuclei in low-lying states by equilibrium neutron emission, with much of the contribution coming from the $^9Be^* \rightarrow 2\alpha + n$ reaction.

3.2 Optical Models for Elastic and Inelastic Scattering

Elastic scattering of neutrons on target nuclei results in high-energy neutrons with strongly forward-peaked angular distributions, and a moving recoil nucleus. An accurate description of these processes is important for two reasons: (1) the recoil nucleus deposits its kinetic energy within a short range and contributes to the kerma; and (2) the high-energy neutrons must be tracked in Monte Carlo transport simulations to account for their future interactions with matter. We determine elastic scattering cross sections using optical model analyses, which are also needed for generating transmission coefficients, inverse cross sections, and wavefunctions in the equilibrium and preequilibrium calculations.

Kinematical considerations show [50] that the fraction of the total incident energy converted to kinetic energy of the recoil is inversely proportional to the target nucleus mass, and decreases with increasing forward-peaking of the angular distribution. Since tissue materials are composed of predominantly light nuclei, the importance of elastic recoil kerma to the total energy deposition is significant. In carbon at an incident energy of 20 MeV it accounts for approximately 15 % of the total kerma. As the incident energy increases, the increasing forward peaking of elastic scattering results in a decreasing elastic recoil kerma. Since the recoil kerma factor is quite sensitive to the elastic angular distributions, it is important to use an optical potential that accurately describes these distributions.

We have implemented the coupled-channel optical potential similar to that developed by Meigooni *et al.* for neutrons with energies above 20 MeV [51]. This deformed potential couples the 0^+, 2^+ (4.4 MeV), 4^+ (14.1 MeV), and 3^- (9.6 MeV) states in ^{12}C, using an external form-factor input in the ECIS79 code [14]. A rotation-vibration model is assumed for the coupling interaction [51], and we use relativistic kinematics. Below 20 MeV we use a spherical optical model which has been optimized to fit reaction cross section data, which is important for obtaining accurate transmission coefficients for our Hauser-Feshbach calculations. From 10–20 MeV we use the Los Alamos spherical potential ^{12}C [52], and from 10-20 MeV we use the spherical potential developed by Dimbylow [53]. The transition energies between these different potentials were chosen to result in a reaction cross section than changes continuously.

In addition to neutrons, optical potentials are also needed for the other ejectiles for calculating transmission coefficients for their decay. Proton potentials were obtained from the neutron potentials using the Lane model isospin transformation [54], namely $(N-Z)/A \rightarrow -(N-Z)/A$, with a Coulomb correction to the real central potential of $0.4Z/A^{1/3}$. Potentials for deuterons and alphas up to high energies were obtained using the method of Watanabe, as implemented by Madland [55]. This work modifies the Perey proton potential [56] to produce composite-particle potentials using simple physical arguments about the dependence of the potential upon the

number of constituent nucleons.

Comparisons of these optical potential predictions with measured total, reaction, and elastic scattering cross sections are shown in Sec. 6.1.

^{12}C+n coupled-channel potential for $E \geq 20$ MeV

Potential	Well-Depth	Geometry
$V_V(E)$	$50.78 - 0.34E$	$r_V = 1.22, a_V = 0.478 + 0.0043E$
$W_V(E)$	$15.5[1 - 2/(1 + \exp((E-20)/25))]$	$r_V = 1.22, a_V = 0.478 + 0.0043E$
$W_D(E)$	$\exp(0.094E)$ $(20 < E < 21\text{MeV})$	$r_D = 1.25, a_D = 0.27$
	$10.29 - 0.145E$ $(21 \leq E \leq 71$ MeV$)$	$r_D = 1.25, a_D = 0.27$
	0 $(E \geq 71$ MeV$)$	$r_D = 1.25, a_D = 0.27$
$V_{s.o.} = 6.20, r_{s.o.} = 1.05, a_{s.o.} = 0.55; \beta_2 = -0.61, \beta_4 = 0.05$		

^{12}C+n spherical potential (Dimbylow, 1980) for $10 \leq E \leq 20$ MeV

$V_V(E)$	$(10.35E - 1432.5)/30$	$r_V = 1.23, a_V = 0.6$
$W_g(E)$	$-(0.3E + 195)/30$	$r_g = 1.22, a_g = 1.2$
$V_{s.o.} = 7.0, r_{s.o.} = 1.23, a_{s.o.} = 0.6$		

^{12}C+n spherical potential (Young *et al.*, 1990) for $E \leq 10$ MeV

$V_V(E)$	$49 - 0.2E + 0.00008E^2$	$r_V = 1.35, a_V = 0.6$
$W_V(E)$	$-2.7 + 0.135E$	$r_V = 1.35, a_V = 0.7$
$W_D(E)$	$2.5 + 0.125E$	$r_V = 1.26, a_V = 0.45$
$V_{s.o.} = 7.0, r_{s.o.} = 1.3, a_{s.o.} = 0.66$		

Table II: Optical model parameters for neutrons on carbon. All potential parameters are given in units of fm, and MeV. Subscripts "V" and "D" denote Wood-Saxon and derivative Wood-Saxon shapes, respectively, and the subscript "g" used in the Dimbylow potential denotes a surface Gaussian form factor. The coupled channel potential above 20 MeV uses externally-inputted form-factors to couple the rotational-vibrational interactions [51].

3.3 Preequilibrium Reaction Developments

3.3.1 Introduction

Preequilibrium reactions occur when the projectile neutron interacts with the target nucleus in one or more scatterings, often ejecting a particle with a relatively high energy. The experimental measurements of charged-particle producing neutron reactions between 20 and 70 MeV from UC Davis, Louvain-le-Neuve, and Los Alamos, clearly show the importance of preequilibrium emission. In addition to nucleons, preequilibrium cluster particles (particularly deuterons, and alphas) are prevalent. An accurate description of preequilibrium spectra is essential for determining the energy deposition and the kerma. In this section we describe new model developments

which we have made to enable the calculation and evaluation of preequilibrium processes for energies up to 100 MeV.

We have performed model calculations using three different preequilibrium theories for comparison purposes (see Ref. [5]: the semiclassical hybrid model (as implemented in the ALICE code); the semiclassical exciton model (in the GNASH code); and the quantum mechanical theory of Feshbach, Kerman, and Koonin (FKK) (in the FKK-GNASH code). We describe these calculations below, and how on the basis of model calculations and experimental measurements we have evaluated the primary preequilibrium spectra (i.e. processes resulting from the first-emitted preequilibrium particle).

3.3.2 The Feshbach-Kerman-Koonin Theory

The FKK theory [45] has been widely implemented in nuclear reaction calculations over the last decade, and we have undertaken a program to apply this theory for nuclear data evaluation work for incident energies up to 200 MeV [46, 47, 48, 5]. This has entailed developing a system of preequilibrium FKK codes, which determine multistep direct (MSD) and multistep compound (MSC) processes, that can be used in the FKK-GNASH code to perform fully quantum-mechanical nuclear reaction calculations.

The FKK multistep direct mechanism is based on an extension of DWBA calculations for particle-hole creation into the continuum region, and describes the forward-peaked contribution to preequilibrium spectra. The 1-step MSD cross section is given by

$$\frac{d^2\sigma(E,\Omega \leftarrow E_0,\Omega_0)}{d\Omega dE}_{1-step} = \sum_J \frac{(2J+1)}{(2I+1)(2i+1)} \sum_{S_f=0}^{1} \frac{1}{(2S_f+1)}$$

$$\times \sum_{S=|I-S_f|}^{I+S_f} \sum_{l=|J-S|}^{J+S} \rho(1p,1h,U,l) \Big\langle \Big[\frac{d\sigma(E,\Omega \leftarrow E_0,\Omega_0)}{d\Omega}\Big]_l^{DWBA} \Big\rangle. \quad (1)$$

$\rho(1p,1h,U,l)$ is the density of $1p1h$ states with energy U and angular momentum l. The density of states for a p-particle h-hole system can be partitioned into the energy-dependent density multiplied by a spin distribution, $\rho(p,h,E,l) = \omega(p,h,E)\ R_n(l)$. We use the finite well depth restricted Williams [57] expression,

$$\omega(p,h,E) = \frac{g^n}{p!h!(n-1)!} \sum_{j=0}^{h} \binom{h}{j} (-1)^j (E - A_{ph} - j\epsilon_F)^{n-1} \Theta(E - A_{ph} - j\epsilon_F), \quad (2)$$

where $n = p + h$, and we take the single particle spacing as $g = A/13$. The Pauli-blocking factor is $A_{ph} = [p^2 + h^2 + p - 3h]/4g$ and ϵ_F is the Fermi energy which we

take as 40 MeV. The Θ-function is unity if its argument is greater than zero, and zero otherwise. A Gaussian angular momentum distribution is assumed,

$$R_n(l) = \frac{2l+1}{2\sqrt{2\pi}\sigma_n^3}\exp\left[-\frac{(l+1/2)^2}{2\sigma_n^2}\right], \tag{3}$$

with the Gruppelaar/Facchini recommended spin cut-off, $\sigma_n^2 = 0.24nA^{2/3}$ [58]. $\left\langle\left[\frac{d\sigma(E,\Omega\leftarrow E_0,\Omega_0)}{d\Omega}\right]_l^{DWBA}\right\rangle$ is the average of DWBA cross sections exciting $1p1h$ states of energy U consistent with angular momentum and parity conservation. The $1p1h$ states are obtained from a spherical Nilsson model. We calculate the DWBA form factors for the various transitions with DWUCK4 [59] using a Yukawa potential of range 1 fm, and strength V_0.

Multistep contributions are obtained by convoluting 1-step cross sections since on-shell and random matrix element approximations are made,

$$\frac{d^2\sigma^{(N)}(E,\Omega\leftarrow E_0,\Omega_0)}{d\Omega dE} = \frac{m}{4\pi^2\hbar^2}\int d\Omega_{N-1}\int dE_{N-1}E_{N-1}$$

$$\times\ \frac{d^2\sigma^{(1)}(E,\Omega\leftarrow E_{N-1},\Omega_{N-1})}{d\Omega dE}\ \frac{d^2\sigma^{(N-1)}(E_{N-1},\Omega_{N-1}\leftarrow E_0,\Omega_0)}{d\Omega_{N-1}dE_{N-1}}, \tag{4}$$

The MSC mechanism is important for incident energies up to about 30 MeV, and below this energy we developed a model for linking the MSC and MSD processes [16], which we found to be necessary for obtaining the correct magnitude of preequilibrium emission.

In order to assess the applicability of the FKK theory for modeling nucleon-induced reactions, we have analyzed experimental emission spectra and angular distributions for a range of reactions which include: 25, 45, 80 and 160 MeV (p,xn) and (p,xp) reactions on ^{90}Zr and ^{208}Pb [43, 48, 60]; 14, 20, and 26 MeV (n,xn) and (n,xp) reactions on ^{93}Nb [16]; 14 MeV (n,xn) reactions on ^{179}Hf [44]; and a range of proton and neutron induced reactions on medium-mass target nuclei for energies up to 26 MeV [61]. These FKK-GNASH analyses showed that the FKK theory is able to describe measured spectra well in most cases. There is a tendency, however, to underpredict backward-angle cross sections at the higher incident energies [43], and for this reason in this evaluation work we apply the Kalbach-systematics [29] for describing the angular variations of the emission spectra. These analyses also enabled us to determine the systematical variation of the residual interaction strength, which is a parameter in the theory.

To implement the FKK theory for preequilibrium calculations of reactions on light nuclei, some modifications were made to our codes: (1) the number of partial waves used in the calculations was reduced to 6, since the small nuclear size results in fewer

angular momentum states being important; (2) the wide-spacing of the single-particle levels required us to increase the energy-averaging width in the MSD calculations to obtain results which varied smoothly with emission energy. Physically this can be justified on the basis of the finite widths of the states, and the fact that nuclear deformations result in a splitting of degenerate spherical states and a reduction of the single-particle spacings.

In Fig. 2 we show the variation of the nucleon-nucleon effective interaction strength with incident energy that we obtain. The systematic difference between this parameter for (n,n') and (n,p) reactions is due to the fact that our calculations use a 1-component formalism, so that differences in accessible state densities, as well as differences in the n-n and n-p interaction strengths, are absorbed into the extracted residual-interaction strength parameter, which must be considered "effective". The variation with energy seen in Fig. 2 is similar to that found in our analyses [16, 43] of other preequilibrium reactions, and the values shown are consistent with the mass-dependence noted by Demetriou, Kanjanarat, and Hodgson, in Ref. [62].

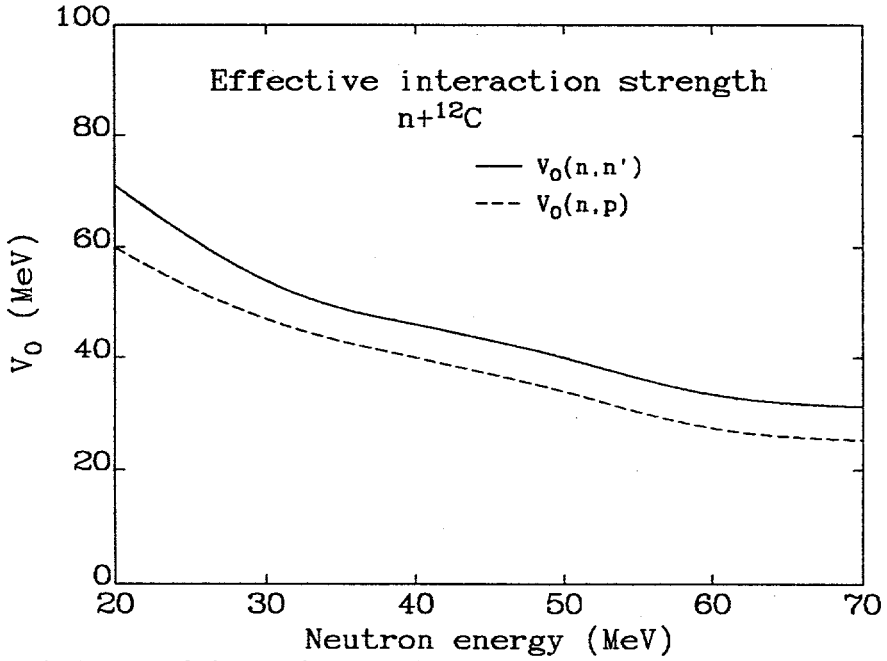

Figure 2: Variation of the nucleon-nucleon residual interaction strength with incident energy.

3.3.3 The Exciton Model

The semiclassical exciton model, as formulated by Kalbach, has been applied extensively in GNASH calculations for incident energies up to 200 MeV [63, 64, 65]. Full

details of the formalism can be found in Ref. [3]. Here, we describe a recent modification to the preequilibrium calculations which allows for a more accurate description of angular momentum effects.

The spin distribution of residual nuclei following preequilibrium reactions impacts upon observables which are sensitive to angular momentum effects, such as the relative production of discrete gamma ray in the residual nuclei. We have improved the preequilibrium calculations in the GNASH code by developing new theories for determining these distributions, for both the FKK and the exciton models [44]. These model developments were tested by analyzing LAMPF/WNR measurements of $(n, xn\gamma)$ reactions for incident energies up to 200 MeV [64] and isomer production in 14 MeV neutron reactions [44].

We showed in Ref. [44] how the exciton model spin dependence of residual nuclei can be obtained from the quantum mechanical FKK MSD results in Eqs. (1,4) by (a) Replacing the l-dependent DWBA matrix elements by l-independent global energy averaged values (ultimately obtained by detailed balance); (b) Assuming an energy-angle factorization of the DWBA matrix elements; and (c) Realizing that the resulting convolution of $1p1h$ densities yield $NpNh$ densities. This gives an exciton model spin distribution of residual nuclei from a preequilibrium stage N, $P_N(J)$,

$$P_N(J) = \frac{(2J+1)}{(2I+1)(2i+1)} \sum_{S_f=0}^{1} \frac{1}{(2S_f+1)} \sum_{S=|I-S_f|}^{I+S_f} \sum_{l=|J-S|}^{J+S} R_n(l), \qquad (5)$$

where $n = p + h = 2N$ and the notation follows that of Eq. (1), and $\sum_J P_N(J)$=1. If the FKK assumption of zero spins is made, this reduces to $P_N(J) = (2J+1)R_n(J)$. But using exact spins, and in particular coupling in the target spin, results in a spin distribution boosted to higher spins than obtained with the zero-spin approximation.

3.3.4 The Hybrid Model

The hybrid model for preequilibrium reactions, as implemented in the ALICE code [4], has been used in many different analyses of nuclear reactions for incident energies up to 250 MeV. Some recent calculations are described in Ref. [5] where we presented results for neutron reactions on biologically-important elements.

In order to optimize the model calculations for reactions on biologically important elements, we have made a number of modifications to the ALICE code: (1) Rather than use internally-calculated inverse cross sections, we read in pre-calculated inverse cross sections for all residual nuclei based on the optical model calculations described in Sec. 3.2; (2) Pre-calculated nuclear level densities are also read in, based on a Gilbert-Cameron model with the level density parameters determined so that the continuum description matches the density of observed low-lying levels, for all resid-

ual nuclei; (3) We included a phenomenological model for describing preequilibrium deuteron emission, which cannot be neglected for these reactions.

We have also developed a version of ALICE which calculates recoil energies of the residual nuclei, which can be used for determining nonelastic recoil kerma. Even though the evaluated libraries described in this report were generated with the GNASH code, and nonelastic recoil kerma determined with the energy-balance method described in Sec. 4, the ALICE recoil calculations were very useful for benchmarking these calculations.

3.3.5 Evaluation of Primary Preequilibrium Spectra

We described our preequilibrium model calculations of reactions on biological nuclei in Ref. [5], where we compared results based on the above three models with experimental measurements. The various calculations gave rather similar results, and described the measurements fairly well. Preequilibrium alpha emission, which we calculated with the cluster model of Kalbach [3, 66], also described measurements well. We found that preequilibrium deuteron emission was the hardest mechanism to describe accurately: the cluster model of Kalbach gave a reasonably accurate integrated deuteron cross section and average energy, but in some cases the spectral shape deviated from the measurements.

For the present work we have evaluated the primary preequilibrium particle emission spectra using the above model calculations, modified to better agree with measurements in certain cases. We achieved this by modifying the GNASH code so that pre-evaluated primary preequilibrium spectra for n, p, d, and α particles can be read from an input tape. We have not relied solely on results from model calculations since an accurate description of the fast particle emissions is critical for correctly determining dose deposition, and our comparisons with measurements, particularly for deuteron emission, show that the model's accuracy can be limited. When evaluating the preequilibrium spectra we considered:

- Experimental measurements of the emission spectra, where they exist.
- Results obtained from model calculations, using both the FKK, hybrid, and exciton models [5].
- Constraints arising from flux conservation (unitarity) [43].
- Systematics first reported by Kalend *et al.* [67] indicating that preequilibrium (p, xp) differential spectra are about twice as high as (p, xn) (due to a factor of 2 in the accessible phase space). From these systematics we can infer that (n, xn) differential spectra should be about twice those for (n, xp) in the preequilibrium regime.

Since experimental emission spectra are comprised of processes arising from a number of reaction mechanisms: primary preequilibrium; multiple preequilibrium; and compound nucleus decay; our evaluation of the primary component was optimized by an iterative calculational procedure. As well as providing a basis for many of the preequilibrium spectra evaluations, the model calculations enable interpolations and extrapolations to energies where measurements do not exist.

3.4 Multiple Preequilibrium Emission

Contributions from multiple preequilibrium emission (MPE) processes (where more than one particle is emitted through a preequilibrium mechanism) become important for incident energies above 50 MeV. The GNASH code has been benchmarked against experimental measurements for incident energies up to 200 MeV, and the importance of multiple preequilibrium emission has been demonstrated. When modeling the LAMPF/WNR ^{208}Pb$(n, xn\gamma)$ measurements for incident neutrons up to 200 MeV [64], we showed that MPE has a dramatic impact on excitation functions of the residual nuclei that are produced. Also, our calculations for the NEA intermediate-energy code intercomparison for proton reactions on ^{90}Zr and ^{208}Pb [42, 43, 60, 65], for incident energies up to 160 MeV, showed the importance of multiple preequilibrium emission for describing inclusive emission spectra while simultaneously satisfying unitarity.

We use the generalized MPE theory which we presented in Ref. [43] to determine nucleon MPE. The angle-integrated spectrum of multiple preequilibrium emission is then given as a sum of contributions from each preequilibrium stage N (where p=h=N before emission),

$$\frac{d\sigma_{mul}^{(N,j)}}{dE} = \sum_{i=\pi,\nu} \int_{U=E+B}^{U_{max}} \frac{d\sigma^{(N,i)}}{dU} \left[\frac{\omega(1p,0,E+B)\omega(p-1,h,U-E-B)}{p\,\omega(p,h,U)} R_N^{i,j} \right] T_j(E)\, dU \tag{6}$$

where E is the emission energy, i labels the type of primary-emitted particle [π = proton, ν = neutron], and j labels the multiple preequilibrium particle type. $d\sigma^{(N,i)}/dU$ is the differential cross section of p-h states after primary preequilibrium emission of a nucleon of type i from stage N as a function of residual nucleus energy. The transmission coefficient $T_j(E)$ is the probability that the continuum particle j escapes with an energy E, and we take this from a Gamov penetrability factor. The quantity in the square brackets represents the probability of finding a particle j at an energy $(E+B)$ inside a p-h exciton configuration of energy U, based on the equiprobability assumption. $R_N^{i,j}$ accounts for neutron-proton distinguishability and is the probability of finding a nucleon of type j in the exciton class N after primary emission of type i. Since we consider only one emission in the multiple preequilibrium process, these numbers yield unity when summed over j for a given i, N. Blann's method

(Eqs. (9,10) of Ref. [68]) is used to determine these values, using a ratio of the n-p to n-n or p-p cross sections of 3:1.

For incident neutron energies above 50 MeV we found that MPE is essential for reproducing the magnitude of preequilibrium spectra, while conserving the reaction flux. When modeling reactions on carbon at the higher energies, the MPE mechanism is also important for correctly describing the magnitude of alpha emission: nucleon MPE processes suppress the cross section for the 3α break-up process and prevent an overprediction of alpha production.

3.5 Equilibrium Emission

3.5.1 Hauser-Feshbach Theory

The GNASH code uses Hauser-Feshbach theory to calculate equilibrium emission of particles and gamma rays, conserving angular momentum and parity in an open-ended sequence of decay chains. As the incident energy increases, the number of different reaction pathways increases and it becomes impractical to consider all decay possibilities. Furthermore, since many of the decay sequences contain a negligibly small amount of cross section, it is unnecessary to explicitly calculate them; instead, we performed trial calculations to determine the most important reaction pathways and ignore paths that contain < 1 mb of cross section. We explicitly model the decay of carbon isotopes ranging from ^{13}C to ^{9}C, boron isotopes from ^{12}B to ^{8}B, beryllium isotopes from ^{11}Be to ^{7}Be, lithium isotopes from ^{8}Li to ^{5}Li, and helium isotopes from ^{7}He to ^{5}He. We included gamma, neutron, proton, deuteron, and alpha particle decay channels. Experimental measurements of t and ^{3}He emission [17, 19] show them to be very small decay processes.

Our treatment of equilibrium emission differs from that of Brenner and Prael [17, 10], who used a Fermi break-up model. That approach partitions the decay fragments statistically according to their phase-space probability and allows for three-body (and higher order) fragmentation mechanisms. In contrast, our Hauser-Feshbach calculations describe the fragmentation process in terms of sequential two-body compound-nucleus decays. For instance, one of the important $^{12}\mathrm{C}(n, n'3\alpha)$ break-up mechanisms is modeled in our calculations firstly as an inelastic neutron scattering, followed by alpha emission, followed by the break-up of the beryllium residual nucleus into two alpha particles. [1] As will be shown in Sec. 6, it is clear that our Hauser-Feshbach calculations describe experimental measurements well. Use of the Hauser-Feshbach theory also has the advantage (like the Fermi break-up method) of incorporating non-statistical nuclear structure effects on the emission spectra, due to the wide-spacing

[1] The example here describes just one of the decay sequences that can result in 3α production. We do include all the other possible 3α break-up mechanisms.

of low-lying discrete levels.

In order for the GNASH code to be able to correctly describe the sequential decay processes in light nuclei, a number of modifications were made to the code. GNASH determines the emission spectra of the light $A < 4$ ejectiles, but in the decay schemes of light nuclei the "residual" nucleus must also be added into the ejectile spectra if its mass is ≤ 4. An example is the decay of ^{5}Li$\rightarrow \alpha + n$, where both tha alpha particle and the neutron must be added into the ejectile spectra.

3.5.2 Level densities and discrete levels

We determine nuclear level densities within the GNASH code using the Ignatyuk model [69], as implemented by Arthur *et al.* [12]. This model uses a Gilbert-Cameron type level density expression (constant temperature plus Fermi-gas), but unlike the original Gilbert-Cameron model it includes an energy-dependent Fermi-gas level density parameter. This allows for the physically-expected behavior of a washing out of shell effects with increasing excitation energy, and enables level densities to be determined with increased accuracy in these high-energy calculations. The energy-dependent Fermi-gas parameter is given by

$$a(U) = \alpha[1 + (1 - \exp(-\gamma \mathrm{U})\delta \mathrm{W} \ / \mathrm{U}] \qquad (7)$$

where α is the asymptotic value at high energies given by $\alpha/A = \eta + \beta A$, with $\eta = 0.1375$ and $\beta = -8.36 \times 10^{-5}$ as obtained by Arthur [12] in a fit to resonance s-wave data, and $\gamma = 0.054$. Shell effects are included in the term δW which is determined from the difference between the experimental (Wapstras 1988 compilation [70]) and liquid-drop expression results. Pairing energies were obtained from the Cook systematics with the Los Alamos extensions to light nuclei from Ref. [52].

The above continuum level density formulation is matched continuously onto discrete low-lying levels at the lower excitation energies. Experimental discrete level information is specified up to an excitation energy below which the experimental measurements were judged complete. Discrete level information (energy, spin, parity, gamma-ray branching ratios) is tabulated for each nuclide in a GNASH input tape, which is based on a number of different sources including the Livermore file [71], the ENSDF file, and the Ajzenberg-Selove compilations [72]. For each nucleus we performed a level-density analysis and determined the excitation energy below which we judged the level data complete. Table III below lists the number of discrete levels used, and the matching energy, for the residual nuclides that can be produced (many of which are unstable). As an example of our results, in Figs. 3 and 4 we show the experimental cumulative number of levels matched on to our continuum statistical description, for ^{12}C and ^{12}B respectively.

Nucleus identification (1000Z+A)	Number of low-lying levels included	Excitation energy for matching to continuum
6013	10	9.190
6012	8	12.162
6011	12	8.724
6010	5	7.180
6009	2	3.330
5012	14	6.138
5011	22	12.057
5010	25	8.895
5009	4	3.005
5008	3	3.090
4011	7	3.990
4010	10	9.465
4009	6	5.531
4008	14	20.250
4007	6	10.300
4006	2	2.505
3010	1	0.000
3009	5	6.955
3008	8	7.385
3007	8	9.940
3006	6	5.792
3005	1	0.000
3004	3	4.100
2009	1	0.000
2008	1	0.000
2007	1	0.000
2006	4	16.450
2005	2	6.000

Table III: For the various nuclides that can be produced we list the number of low-lying discrete levels included in our calculations, along with the matching excitation energy (in MeV) above which we used the Ignatyuk continuum level density description.

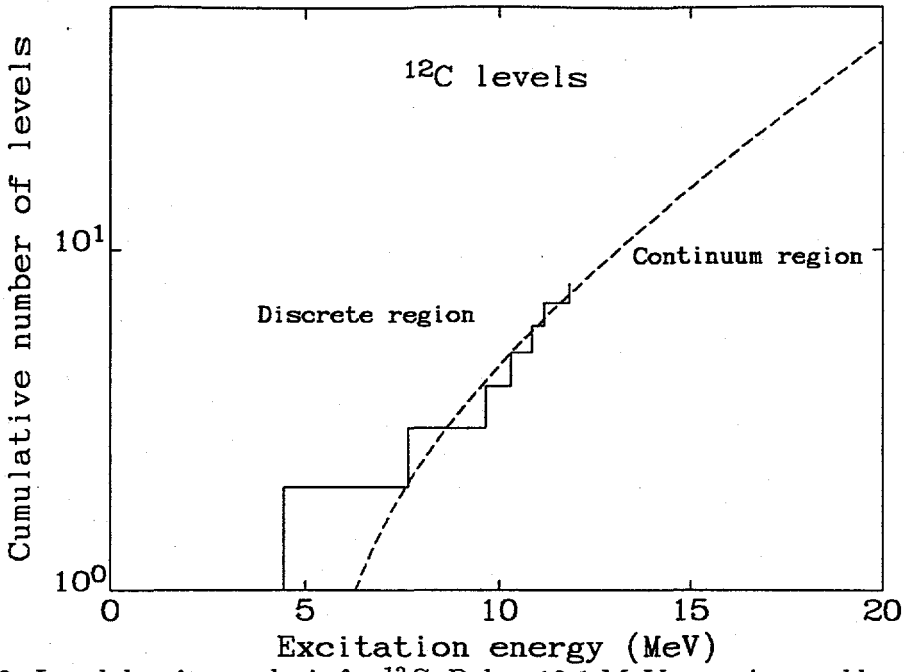

Figure 3: Level density analysis for ^{12}C. Below 12.1 MeV experimental levels are used, and above this energy we use a statistical description.

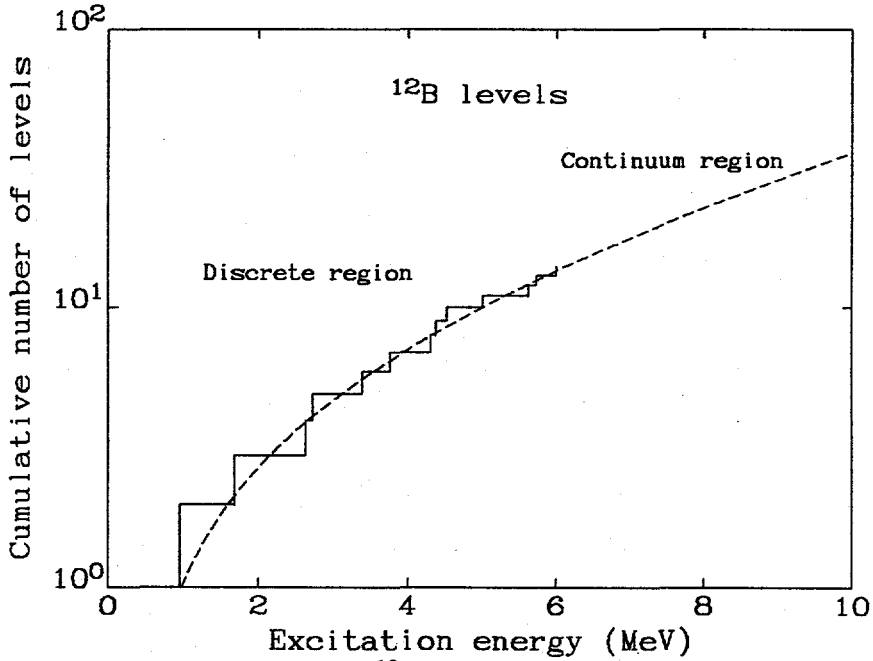

Figure 4: Level density analysis for ^{12}B. Below 6.1 MeV experimental levels are used, and above this energy we use a statistical description.

3.5.3 Gamma-Ray Strength Functions

Gamma-ray transmission coefficients were obtained from the generalized Lorentzian model of Kopecky and Uhl [73]. This model modifies the Brink hypothesis [74] by including an energy-dependent giant resonance width from Fermi-liquid theory. The giant resonance formulation of Kopecky and Uhl was used for E1, E2 and M1 radiation.

Even though photonuclear data on light elements shows strong nuclear structure effects, we obtained Lorentzian parameters approximating the ground-state absorption for use in the above model. Since the photoproton cross section on ^{12}C is large (and exceeds the photoneutron cross section), the Dietrich and Berman compilations of photoneutron data cannot be used to obtain the total photoabsorption cross section. Instead, these cross sections were taken from the Fuller evaluation [75], which is based upon absorption measurements by Ahrens *et al.* [76].

Our calculated photon production spectra are comprised of both discrete gamma-ray lines from gamma-decays in the residual nuclei, and a statistical continuum contribution from competition with particle decay at higher excitation energies. We assume that the gamma rays are emitted isotropically.

3.6 Continuum angular distributions

The angle-energy correlation of emitted particles is obtained by applying the phenomenological systematics of Kalbach [29]. In the absence of an underlying theoretical description of the systematical properties of continuum angular distributions, Kalbach developed phenomenological parameterizations by analyzing over 900 data sets of nucleon- and alpha-induced reactions, for incident energies up to 600 MeV. Since these systematics generally describe measurements well, apply to many different projectile/ejectile types, and are computationally straightforward to apply, they have been widely used with considerable success in nuclear data evaluation work. They apply a forward-peaked angular distribution to the preequilibrium contribution and a symmetric-about-90^0 contribution to the equilibrium contribution. As Kalbach points out, the success of her parameterization rests upon the basic functional form of an exponential in $\cos\theta$ to describe the forward peaking.

Recently we have developed a theoretical model of preequilibrium angular distributions which provides a physical basis for the Kalbach systematics [77]. Using state densities with linear momentum and explicitly conserving momentum in the preequilibrium cascade we showed that preequilibrium angular distributions have the functional form of the Kalbach-systematics. The $\cos\theta$ dependence comes from the cosine formula in the vector addition of momenta and the exponential dependence comes from the Gaussian distribution of momentum states (related to the Gaussian angular

momentum dependence). Furthermore, our work provides a straightforward theoretical expression for the a-parameter which governs the extent of forward-peaking that Kalbach obtained from systematics, and includes angle-energy correlations for all orders of scattering. Our work does not supersede that of Kalbach – while it has been successfully applied to nucleon reaction angular distributions up to 100 MeV, more research is needed for a description of alpha and deuteron reactions. Rather, our work provides a physical basis for Kalbach's systematics and provides further confidence in their validity.

4 Methods for Calculating KERMA

4.1 Introduction

It is essential that the libraries accurately describe the kerma (kinetic energy given to charged particles) if they are to be successfully used in transport calculations of absorbed dose. Indeed, an important aspect to the validation of the libraries is that they should be consistent with measured kerma values. In this section we describe the methods we use to obtain the partial kerma factors for the light particles, as well as the elastic and nonelastic recoils. We discuss in detail a method, first reported by Romero *et al.* [78], that we have implemented for determining the nonelastic recoil kerma. The ENDL libraries tabulate individually the average kinetic energy depositions to the light ($A \leq 4$) particles. They also tabulate the sum of kinetic energies given to the nonelastic recoil products. The various heavy nuclide cross sections and energies are not individually represented in the libraries since their small range allows us to assume a local energy deposition.

The partial kerma factor for a certain secondary charged-particle type is obtained from the product of the cross section (in b) and the average energy (in MeV), in units of b.MeV/atom. To convert to the SI unit of Gy.m^2 (where 1 Gray (Gy) = 1J/1Kg) we multiply by 0.804044 $\times 10^{-15}$, which is the product of three factors: the number of atoms per kg of ^{12}C (6.0221367 / 12) $\times$ 10^{26}; J/MeV (1.60217733 $\times 10^{-13}$); and m^2/b (10^{-28}).

4.2 Kerma to Light ($A \leq 4$) Ejectiles

Obtaining average energy depositions for the light particles from our GNASH calculations is a straightforward matter. GNASH calculates emission spectra of the light particles in the channel energy frame (the total kinetic energy of the ejectile plus residual nuclide in the center-of-mass frame). By assuming two-body kinematics, and using channel-energy angular distributions from the Kalbach systematics, these spectra are transformed into the laboratory frame and average laboratory energy depositions are obtained. The assumption of two-body kinematics is clearly not valid for the lower emission energies, where many sequential decays contribute, though we expect the errors introduced by using this assumption to be small. When the production cross section σ_i of the i^{th} ejectile type is measured in barns, and the average emission energy E^i_{av} is measured in MeV, the partial kerma for a carbon target is given by $0.804\sigma_i E^i_{av}$, in units of f Gy m^2 (where 1 fento, 1f $=10^{-15}$).

4.3 Kerma to Elastic Recoils

The kerma given to ^{12}C recoils in elastic scattering is significant, especially at the lower energies. For instance at 20 MeV, according to our evaluations it amounts to about 15% of the total kerma, but drops to only about 2% at 100 MeV. Our libraries tabulate elastic scattering cross sections in the center-of-mass frame, and from these the average energies given to the emitted neutron and the ^{12}C recoil in the laboratory frame can be determined. The accuracy of this calculation rests upon the accuracy of the evaluated elastic angular distributions, and since our optical model calculations generally describe the measurements very well, we are fairly confident of the accuracy of our results. We use relativistic two-body kinematics to determine these average energies and kerma factors. However, our results agree closeley those obtained using a simple non-relativistic expression noted by Bach and Caswell [50],

$$E_{av}^{lab} = \frac{2AE_{inc}^{lab}}{(A+1)^2}\overline{(1-\cos\theta_{c.m.})}, \tag{8}$$

where E_{av}^{lab} is the average energy of the recoil, the target mass A is 12 here, E_{inc}^{lab} is the incident neutron energy, and the average is performed over the center-of-mass elastic angular distribution.

4.4 Kerma to Heavy (A >4) Non-Elastic Recoils

It is a more difficult task to obtain energy depositions to the nonelastic recoils. This is because the GNASH code normally provides only the production cross sections of the recoils, and not their kinetic energies. It does this because fluxes for different reaction pathways leading to the same recoil nuclide are summed together, to simplify the computations, before possible decays of that recoil are considered. For this reason, details of the various recoil kinetic energies are lost. While there does exist a version of GNASH (run with an auxiliary code RECOIL [79]) which follows all heavy recoil decays in a fully exclusive manner and calculates recoil energies, this code becomes impractical to use for energies much above 20 MeV where many break-up channels open up.

Since we do not need the kinetic energies given to individual recoils, but only the total kinetic energy given to them, we can apply energy and baryon conservation to determine this quantity [78]. Knowing the incident projectile energy, the energies of the light ejectiles, and the production cross sections of the products, energy-mass conservation will determine the nonelastic recoil kinetic energies. In inclusive reaction analyses the total Kerma factor K is given by

$$\frac{1}{N}K = \sum_{i\leq 4}\sigma_i E_i^{av} + \sum_{i>4}\sigma_i E_i^{av} + \sigma_{el}E_{el}^{av} \tag{9}$$

where σ_i is the inclusive production cross section of the ith particle type, with average kinetic energy E_i^{av}. The constant N is the number of nuclei of the element per gram, and for a kerma factor defined in units 10^{-15} Grays m^2, with σ_i in barns and E_i^{av} in MeV units, N=0.804 for carbon. In Eq. (9) we partition the kerma into contributions from light particles ($i \leq 4$), nonelastic recoils ($i > 4$), and elastic scattering recoils $\sigma_{el}E_{el}^{av}$. Baryon number conservation implies that

$$\sum_i A(i)\sigma_i = (1 + A_{tgt})\sigma_R, \tag{10}$$

where $A(i)$ is the mass number of the ith product, A_{tgt} is the atomic weight of the target, and σ_R is the reaction cross section. Eq. (10) is particularly useful for analyses based on inclusive-reaction emission spectra, and can be considered to be analogous to the exclusive-reaction flux conservation requirement that the sum of partial cross sections should add to the total reaction cross section. Energy conservation for a projectile with lab energy E_{inc} and mass m_{inc} implies that

$$\sum_i \sigma_i(E_i^{av} + m_i c^2) + \sigma_\gamma E_\gamma^{av} = (E_{inc} + m_{inc}c^2 + m_{tgt}c^2)\sigma_R, \tag{11}$$

where m_i is the mass of the ith product nuclide, and σ_γ and E_γ^{av} are the production cross section and average energy of the gamma rays. Since $m_i = A(i) + \Delta m_i$, where Δm_i is the mass excess, Eqs. (10,11) can be combined to give an energy sum rule

$$\sum_i (E_i^{av} + \Delta m_i)\sigma_i + \sigma_\gamma E_\gamma^{av} = \sigma_R(E_{inc} + \Delta m_{inc} + \Delta m_{tgt}). \tag{12}$$

Solving this equation for the nonelastic recoil kerma yields

$$\frac{1}{N}K_{i>4} \equiv \sum_{i>4} \sigma_i E_i^{av} = \sigma_R(E_{inc}+\Delta m_{inc}+\Delta m_{tgt}) - \sigma_\gamma E_\gamma^{av} - \sum_{i\leq 4}(E_i^{av}+\Delta m_i)\sigma_i - \sum_{i>4} \Delta m_i \sigma_i \tag{13}$$

All the quantities on the right hand side of this equation can be obtained from our GNASH calculations, allowing nonelastic recoil kerma to be deduced. When Romero *et al.* [78] used this type of analysis to estimate non-elastic recoil kerma, they had to make assumptions about the neutron and gamma emission channels which were not measured in their experiment. But since our model calculations provide a full description of these channels our implementation of this method does not suffer from any such uncertainties. We have checked that our calculations are consistent with flux conservation defined in Eq. (10) – differences of only a few percent are seen due to our neglecting some of the decay pathways of minimal importance to make the computations tractable. When implementing Eq. (13) we correct for these small differences to prevent small errors in calculated product masses being converted into large recoil kinetic energies.

The above method provides useful information on the kinetic energies of the nonelastic recoils. It is, however, possible that inaccuracies in other parts of the model calculations would introduce errors into the inferred nonelastic recoils, and for this reason we have evaluated the nonelastic recoil kerma based on information obtained from other model calculations in addition to results from this energy balance method. Specifically, we have developed a version of the ALICE code which calculates recoil kerma factors, and there are also Brenner and Prael values published in Romero's article [78]. From these results we have evaluated the nonelastic kerma values that are shown in Table IX.

5 New ENDL formats for high-energy data

We have developed a new Livermore ENDL format suitable for representing higher-energy nuclear data. This format represents the double-differential inclusive emission spectra of the light ($A \leq 4$) ejectiles, and the average kinetic energies given to these light ejectiles as well as the heavy ($A > 4$) recoils, in the laboratory frame of reference. This format differs from the usual procedure in evaluated data files below 20 MeV where each exclusive reaction is described separately. At higher energies the number of such break-up possibilities increases rapidly, and it becomes impractical to tabulate them all separately. Moreover, many applications (including dose deposition calculations in radiotherapy for which these libraries are designed) do not need exclusive reaction information.

We do not specifically tabulate cross section information for the production of heavy ($A > 4$) recoil nuclides since their very short range allows us to assume a local energy deposition. Instead we represent the average kinetic energy per interaction (i.e. the product of the multiplicity and the average energy) deposited by these recoil nuclei. This quantity is obtained directly from our calculated nonelastic recoil kerma, as described below and in Sec. 6.7.

The double-differential emission spectra of the light ejectiles are fully angle-energy correlated. This means that for each emission angle we tabulate a separate emission energy spectrum, accounting for the fact that angular distributions at different emission energies often differ from each other significantly. For instance, angular distributions at low emission energies often show only a small amount of forward-peaking in the laboratory frame, but at high emission energies the importance of preequilibrium and direct reactions results in strongly forward-peaked angular distributions. Below we describe the various ENDL files that we use to describe this information, for a given incident energy.

Production cross section files for light ejeciles:-

i0 file the reaction cross section (in barns)

i1 file the (lab) angular distribution for all emission energies added together as a function of the cosine of the emission angle, normalized to unity, for ejectile type i

i3 file the (lab) emission spectrum for each of the above angles, normalized to unity, for ejectile type i

i9 file the multiplicity for production, defined as the ratio of the production cross section to the reaction cross section, for ejectile type i

Average kinetic energy files for light ejeciles:-

i10 file the average (lab) kinetic energy per reaction, for ejectile type i. This is related to the partial kerma factor (in units of f Gy m^2) for ejectile i by $0.804/K_i\sigma_R$

Average kinetic energy file for heavy nonelastic ejeciles:-

i11 file Average (lab) kinetic energy per reaction for all heavy nonelastic ejectiles. This is related to the partial kerma factor (in units of f Gy m^2) for nonelastic recoil nuclides by $0.804/K_{i>4}\sigma_R$

Total kinetic energy available to ejectiles:-

i12 file the sum of the individual i10 files, the i11 file, and the incident (lab) energy

Elastic scattering files:-

i0 file the integrated neutron elastic scattering cross section (in barns)

i1 file the (c.m.) angular distribution of the neutron elastic scattering nomalized to unity, as a function of the cosine of the scattering angle

i10 file the average (lab) energy given to the neutron in elastic scattering

i11 file the average (lab) energy given to the carbon recoil in elastic scattering

Note that in the case of elastic scattering we represent the angular distributions in the c.m. frame, which can be done more compactly than in the lab frame (since different c.m. angles have different laboratory energies). Additionally, the c.m. to lab transformation is unambiguous since this is a 2-body reaction. We use relativistic kinematics to determine the average laboratory energies of the neutron and elastic carbon recoil.

The production cross sections following inelastic reactions, however, are all tabulated in the laboratory frame of reference. This facilitates direct comparisons with experimental cross sections and kerma factors without the need to first process the evaluated data into the laboratory frame. This is particularly advantageous for reactions on carbon, where the effects of the c.m. to lab transformations are significant due to its small atomic mass. The unit-normalized angular and energy distributions are used to facilitate linear-linear interpolations to angles and energies not tabulated. The double-differential production cross section (in units of b/MeV-sr) for ejectiles type i with incident energy E_{inc} and emission energy E is obtained from

$$\frac{d^2\sigma(E_{inc},E)}{dEd\Omega} = \frac{1}{2\pi} i0(E_{inc}) \cdot i9(E_{inc}) \cdot i1(E_{inc},\Omega) \cdot i3(E_{inc},\Omega,E). \qquad (14)$$

We have evaluated cross sections for the high-energy library on an incident energy grid of 20, 21, 22, 23, 24, 25, 27, 30, 35, 40, 50, 60, 70, 80, 90, and 100 MeV. Cross sections at other energies are obtained by linear-linear interpolation. We believe that this grid allows an adequate representation of the higher energy cross sections, taking into account the uncertainties in the data. Of the above incident energies, comprehensive production cross section measurements were available at 27, 40, 43, 61, 63, and 73 MeV.

At 20 MeV we have matched the new library onto the existing ENDL library (energies below 20 MeV). To do this, we converted the low-energy ENDL library into the inclusive production cross section format, producing a single library for incident energies from zero to 100 MeV.

6 Results and Comparisons With Experiments

6.1 Total, Elastic, and Reaction Cross Sections

In this section we describe the evaluated total, elastic, and reaction cross sections for neutrons on carbon, based on our coupled-channel optical model calculations. In Ref. [5] we showed how these calculations provide a very good description of available experimental data. There is excellent agreement between the total cross section that we calculate and the measurements, except at energies below 35 MeV where the calculation overestimates the data by about 2%. In this case we apply a small renormalization to the elastic cross sections to remove this discrepancy. The cross sections are shown in Table IV below. We are able to neglect the (very small) differences between the reaction cross section and the nonelastic cross section, and treat these two quantities as being equivalent, since compound elastic cross sections are negligible at the energies considered.

Energy (MeV)	Total	Elastic	Reaction	Inel. 2+	Inel. 3−	inel. 4+
20	1507	1016	491	105	36	4
23	1404	922	482	86	29	3
27	1357	904	453	64	25	2
30	1295	861	434	55	20	2
35	1204	798	406	43	16	1
40	1111	728	383	35	13	1
50	946	603	343	24	9	1
60	812	504	308	18	7	1
70	704	428	276	14	5	0
80	612	368	244	11	4	0
90	540	317	223	8	3	0
100	485	262	223	6	3	0

Table IV: Evaluated total, elastic, and reaction cross sections (in mb) for n+^{12}C for various laboratory neutron energies. Also shown are the (coupled-channels) inelastic scattering cross sections to the 2+ (4.4 MeV), 3− (9.6 MeV), and 4+ (14.1 MeV) states in ^{12}C.

In Fig. 5 we show the evaluated total cross sections compared with experimental measurements, taken from the Brookhaven National Nuclear Data Center CSISRS file. When evaluating the total cross sections for neutrons on carbon most weight was given to the recent measurements by Finlay *et al.* [23] at the LAMPF/WNR Los Alamos white neutron source facility, which have a reported uncertainty of less than 1%. We show our evaluation compared to only the Finlay *et al.* data in Fig. 6.

There are a number of differential elastic scattering cross section measurements

in the 20-100 MeV region [80, 81, 82, 83, 84, 85, 86]. In Table V we present these experimental measurements and we compared to our evaluation in Fig. 7. Where the original authors published values for the integrated cross sections we use their values. We describe below our procedure for integrating differential data in other cases. To integrate the elastic DeVito 40 MeV data [82] we used the Meigooni "best individual fit spherical parameters" (p. 91 of Ref. [87]) in a SCAT2 optical model calculation, since the calculated angular distribution described the differential data very well (see Fig. V-1 of Ref. [87]). This yields a value for the elastic cross section at 40 MeV which is 38 mb higher than Axton's evaluation [8], and we believe our result is more reliable since Axton's assumption of an angular distribution decreasing at the same rate for angles greater than 95 degrees underestimates the back-angle emission. Likewise, since our coupled-channel calculation at 65 MeV described the Hjort *et al.* [83] differential data very well (see Fig. 8), we used the integrated elastic cross section from our calculation. Also, for the 28.15 MeV differential elastic data of Yamanouti *et al.* [84] we used our coupled-channel fit to the data to provide the integrated elastic cross section since it compared well with the measured angular distribution.

In Fig. 8 we show some of these differential data compared with our evaluations. It is evident that the coupled-channel analysis provides a good representation of the measurements, which span a large fraction of the energy range that we are analyzing. Additionally, proton elastic scattering measurements at 30, 46, and 65 MeV [88, 89, 90] provide a useful further check on the optical model analyses. As described in Sec. 3.2, the potential for proton scattering was obtained from the neutron potential by applying Coulomb and isospin transformations. Our calculations shown in Fig. 9 again show good agreement with the experimental data, which is particularly notable since the proton data were not used in any of the potential parameter searches.

Experimental reaction cross sections are compared with our evaluation in Fig. 10. There is a significant spread in the measurents, which we list in Table VI. Some of the experimental reaction cross section values shown in Fig. 10 were obtained by subtracting experimental elastic cross sections from the total (Finlay) cross sections, as indicated in Table VI. While our evaluation describes these measurements well, the uncertainty in the reaction cross section is about 5% at the lower energies, increasing to about 10% at the higher energies.

In Figures 30 and 31 of Sec. 7 we show our calculated coupled-channels inelastic scattering to the 2+ (4.4 MeV) and 3- (9.6 MeV) states in carbon, compared with measurements. Rather than represent scattering to these states separately in the libraries, for simplicity we add their angle-integrated cross sections into the neutron production cross section file (and use the Kalbach systematics to obtain angular distributions).

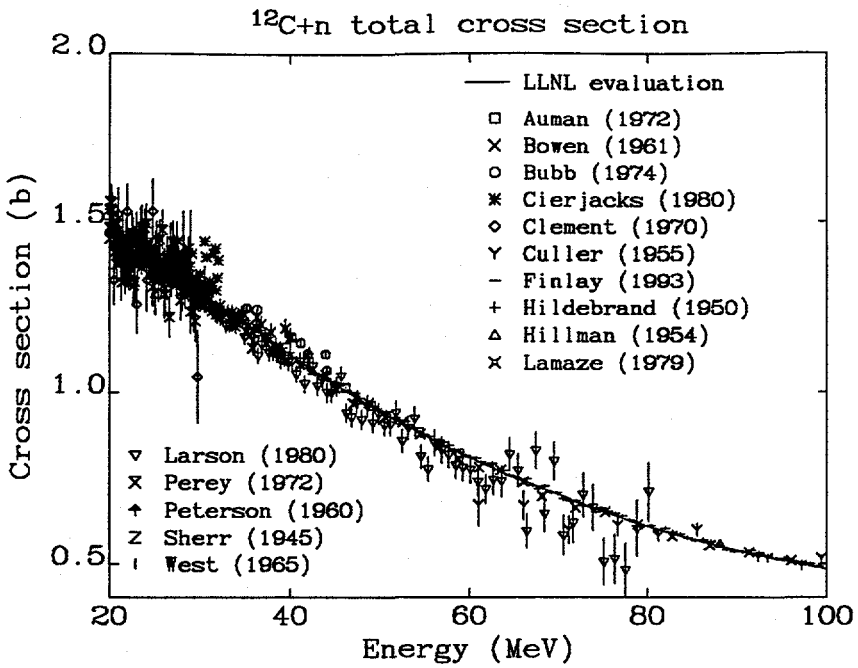

Figure 5: Total cross section for neutrons on carbon. The experimental data were taken from the Brookhaven NNDC CSISRS file.

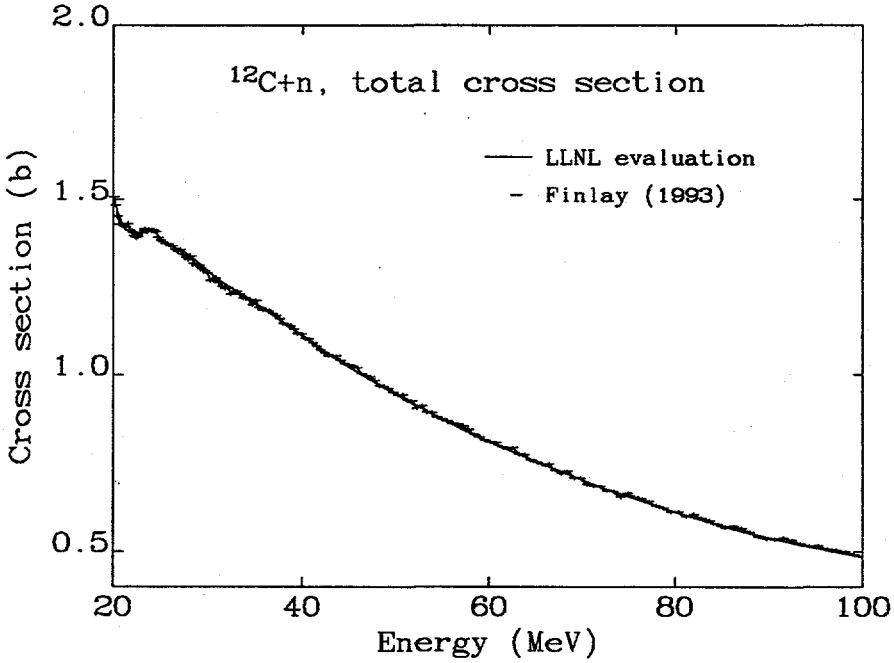

Figure 6: Total cross section for neutrons on carbon compared with experimental data of Finlay *et al.* [23].

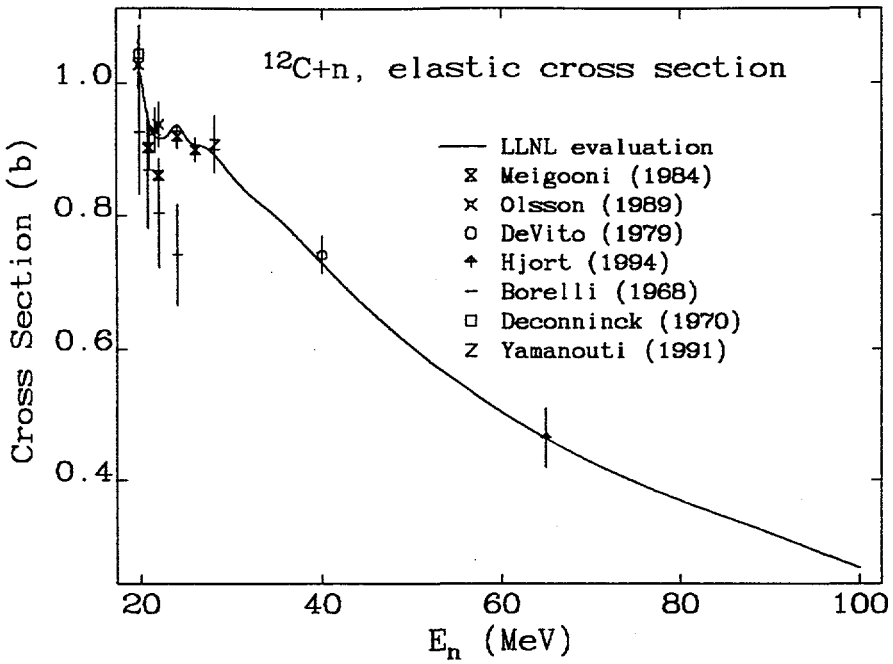

Figure 7: Elastic cross section for neutrons on carbon. The experimental data are given in Table V.

Reference	Energy (MeV)	Elastic cross section (b)
Boreli *et al.* (1968)[a] [85, 8]	20.8, 22.0, 24.0	0.869 ± 0.089, 0.804 ± 0.083, 0.741 ± 0.076
DeVito (1979) [82][b]	40.0	0.741 ± 0.029
Hjort *et al.* (1994) [83][b]	65.0	0.464 ± 0.046
Meigooni *et al.* (1984) [81]	20.8, 22.0, 24.0, 26.0	0.903±0.018, 0.861±0.017, 0.921 ± 0.018, 0.900 ± 0.018
Olsson (1989) [80]	20.9, 21.6, 22.0	0.904 ± 0.033, 0.929 ± 0.034, 0.938 ± 0.034
Yamanouti (1992) [84][b]	28.15	0.908 ± 0.043

[a] Axton interpolated values, p. 47 of Ref. [8]

[b] optical model fit used to obtain integrated elastic cross section (see text)

Table V: Experimental integrated elastic cross section measurements.

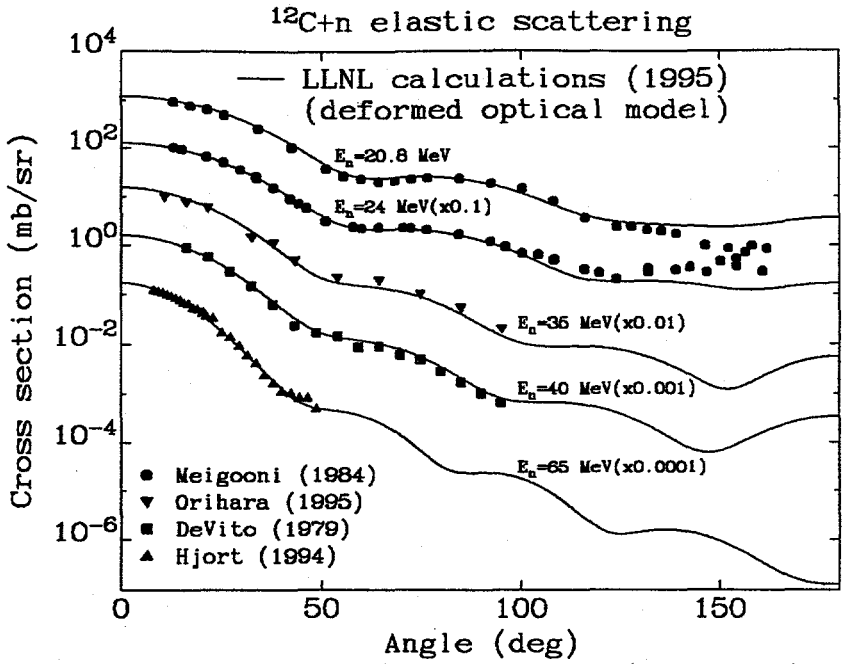

Figure 8: Differential elastic scattering cross sections (c.m. frame) for neutrons on carbon, compared with experimental measurements [81, 82, 83].

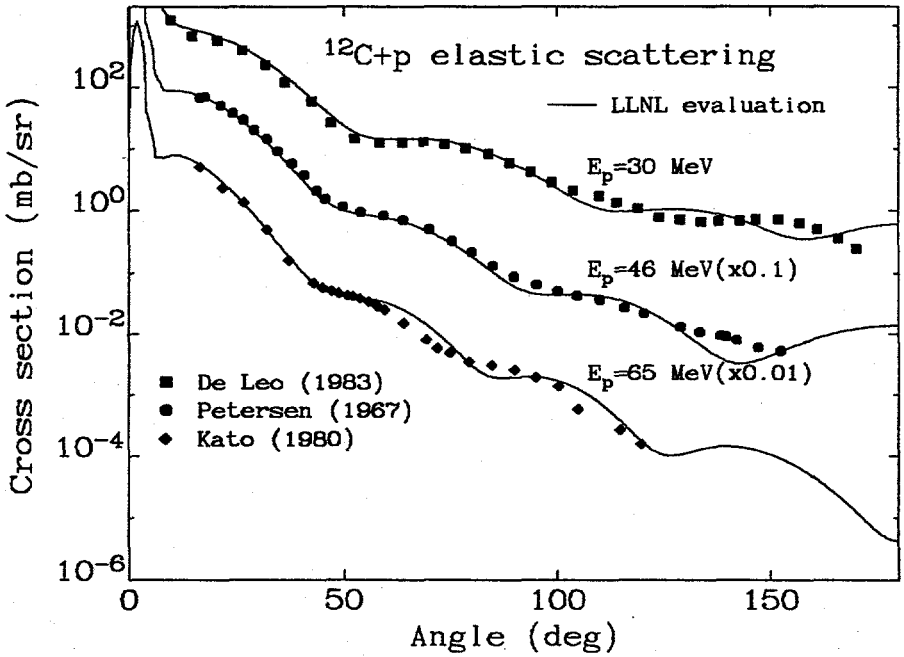

Figure 9: Elastic scattering cross sections (c.m. frame) for protons on carbon, compared with experimental measurements [88, 89, 90].

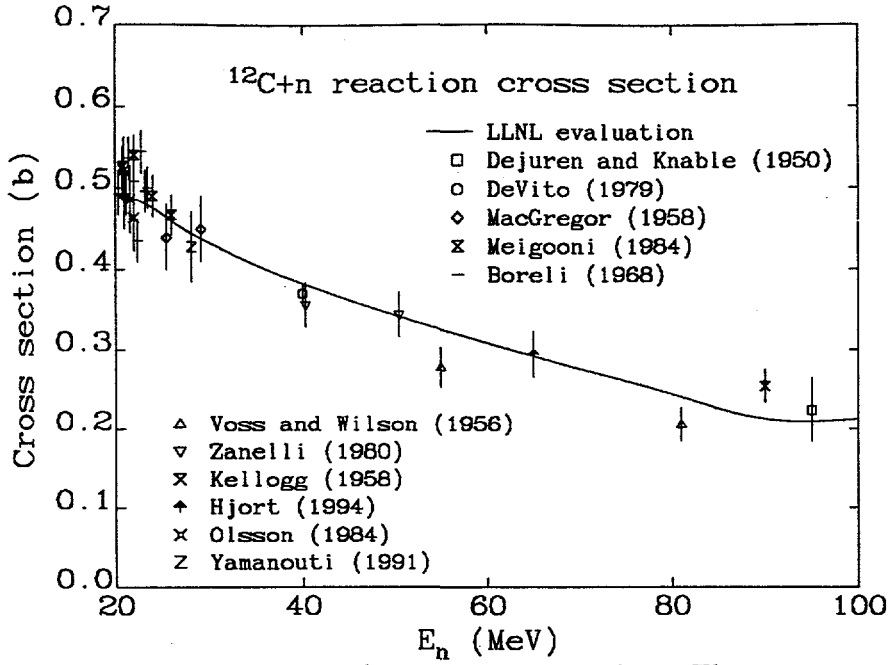

Figure 10: Reaction cross section for neutrons on carbon. The experimental data are given in Table VI.

Reference	Energy (MeV)	Reaction cross section (b)
Boreli *et al.* (1968) [85][a]	20.4, 20.8, 21.2	0.493 ± 26, 0.517 ± 26. 0.493 ± 26
	21.5, 22.0, 22.4	0.536 ± 26, 0.508 ± 26, 0.436 ± 26
	22.8, 23.2, 23.5	0.544 ± 26, 0.496 ± 26, 0.500 ± 26
Dejuren and Knable (1950) [91]	95.0	0.224 ± 0.040
DeVito (1979)[†] [82]	40.0	0.370 ± 0.011
MacGregor *et al.* (1958) [92]	21.0, 25.5, 29.2	0.49 ± 0.04, 0.44 ± 0.04, 0.45 ± 0.04
Meigooni *et al.* (1984)[†] [81]	20.8, 22.0, 24.0,	0.526±0.025, 0.540±0.024, 0.490 ± 0.025,
	26.0	0.467 ± 0.024
Hjort *et al.* (1994) [83][†,b]	65.0	0.294 ± 0.029
Kellogg (1958) [93]	90.0	0.254 ± 0.021
Olsson (1989)[†] [80]	20.9, 21.6, 22.0	0.522 ± 0.040, 0.486 ± 0.041, 0.464 ± 0.041
Voss and Wilson (1956) [94]	55.0, 81.0	0.278 ± 0.025, 0.206 ± 0.021
Zanelli *et al.* (1981) [95]	40.3, 50.3	0.356 ± 0.028, 0.344 ± 0.028
Yamanouti *et al.* (1991) [84][†,b]	28.15	0.428 ± 0.043

[†] inferred from measured elastic cross section
[a] digitized from published figure
[b] optical model fit used to obtain integrated elastic cross section

Table VI: Experimental reaction cross section measurements. Some of the values were inferred from elastic scattering measurements, as noted in the key (see text).

6.2 Inclusive production Cross Sections

In Table VII we present our calculated production cross sections and average kinetic energies for the light ejectiles. Fig. 11 shows graphically the variations in these production cross sections with incident neutron energy, from 20 to 100 MeV.

Energy	$\sigma(n)$	$E_{av}(n)$	$\sigma(p)$	$E_{av}(p)$	$\sigma(d)$	$E_{av}(d)$	$\sigma(\alpha)$	$E_{av}(\alpha)$	$\sigma(\gamma)$	$E_{av}(\gamma)$
20	421	6.66	36	4.07	13	3.23	887	2.55	144	4.02
23	423	7.53	48	4.80	28	5.17	907	2.95	137	3.84
27	376	8.87	66	6.50	54	7.46	766	3.42	135	3.78
30	361	9.87	83	7.59	52	8.32	700	3.87	140	3.71
35	335	11.52	109	9.55	59	10.46	579	4.42	150	3.56
40	324	12.97	126	11.10	62	12.49	495	4.83	145	3.46
50	323	16.04	142	13.29	68	16.06	399	5.30	140	3.35
60	313	19.96	148	16.43	68	19.11	328	5.40	129	3.43
70	300	20.84	158	19.38	79	20.72	293	6.02	109	3.49
80	280	23.57	156	23.36	71	23.50	250	6.41	95	3.42
90	273	25.65	153	24.41	71	25.33	229	6.97	81	3.61
100	305	26.03	172	22.41	81	25.19	236	7.48	73	4.20

Table VII: Evaluated production cross sections (in mb) and average energies (in MeV) in the n+^{12}C reaction, for various laboratory neutron energies (in MeV).

The large cross section for alpha production at low energies seen in Fig. 11 is due to the importance of the 3α break-up mechanism. This follows from the large multiplicty (3) for this reaction. As the incident energy increases, other decay processes become increasingly important, and alpha production falls. For instance, following preequilibrium emission of a particle other than a neutron, 3α break-up cannot occur. Our results support Brenner and Prael's view [41] that the ENDF/B-V evaluated alpha production at 20 MeV is too high.

The variations of the production cross sections with incident energy seen in Fig. 11 are fairly similar to the results obtained by Young *et al.* (Fig. 61 of Ref. [12]). Note that the abrupt discontinuities in their neutron and gamma productions seen at 36 MeV is due to their including scattering to the 4.4 MeV state in their production libraries only above 36 MeV (below this energy it is tabulated separately). Since we include scattering to this state in our neutron production files at all energies we do not see such discontinuities. The exact variation of the production cross sections seen in Fig. 11 depends in a complicated manner on the different competing reaction mechanisms. These cross sections do not increase strongly with incident energy for two reasons: firstly, the reaction cross section decreases by over a factor of two between 20 and 100 MeV; and secondly, at a relatively low incident energy significant fragmentation of carbon occurs, and so an increasing incident energy does not result in a significant increase in particle production.

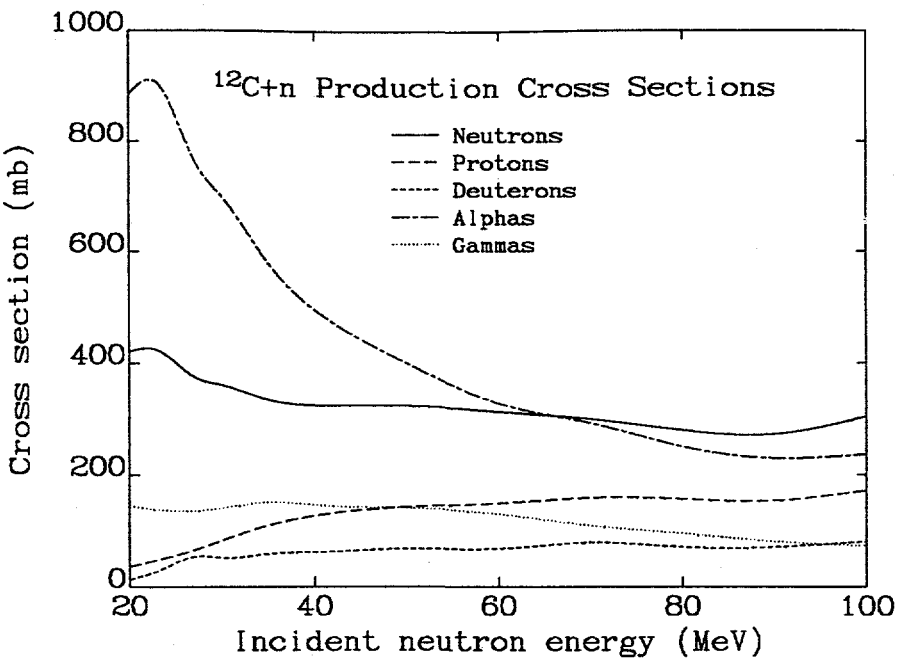

Figure 11: Inclusive production cross sections for ejectiles with $A \leq 4$ in the ^{12}C+n reaction, for incident energies between 20 and 100 MeV

In Fig. 12 we show our calculated production cross sections compared with experimental data. Both the Louvain-la-Neuve and the UC-Davis experiments were not able to detect low-energy emitted particles below their detector thresholds. To obtain the total production cross sections, the low-energy behavior of the various spectra have to be estimated, and a variety of approaches for this have been reported in the literature. Such estimates in the original UC-Davis report [18] assumed a constant differential cross section from the lowest measured energy to zero. However, this approach may significantly underestimate the low-energy cross section in some cases, particularly for alpha emission. In 1986 Romero [78] modified these UC Davis results based on the Brenner and Prael INC calculations at low-energies, resulting in increased cross sections (and kerma factors). Similarly, the recent Louvain-la-Neuve experiments used the Brenner and Prael calculations to extrapolate below their experimental threshold energy [28].

In the next section we show how our calculated emission angle-integrated spectra compare with the measurements. Since our results generally describe the measured spectra somewhat better than those of Brenner and Prael, we have used our calculations to extrapolate the experimental measurements to low-energies. Generally our results do not show as great a low-energy rise as those of Brenner and Prael. Therefore our threshold corrections are smaller than those in Refs. [78, 19], but still exceed corrections resulting from a constant-magnitude assumption. In Table VIII

below we show the raw experimental data, our threshold correction estimates, and the total experimental production cross sections that result. We have assigned an uncertainty of 30% to our threshold corrections, estimated by comparing our corrections with those obtained from the Brenner and Prael calculations [10]. Note that the detector thresholds in the Louvain-la-Neuve experiments are fairly high, so that the total experimental production cross sections here are less reliable. Also, in both the UC-Davis and the Louvain-la-Neuve experiments the threshold corrections for alpha-particle emission often exceed the uncorrected experimental results – and therefore the term "experimental" for the total cross sections we obtain here is rather tenuous. Our estimated total experimental production cross sections are fairly consistent with those presented by Slypen *et al.* [19], though ours are slighly smaller since the low-energy corrections from our calculations are generally somewhat smaller than those from Brenner and Prael. Agreement between our evaluation and the UC Davis and Louvain-la-Neuve measurements seen in Fig. 12 is fairly good, and our results are also consistent with the older measurements by Kellogg at 90 MeV [96].

It is worth noting that the total production cross sections that we obtain are different to those found by Axton [8] when integrating the UC-Davis data. He integrated double-differential data, assuming a constant cross section from the lowest measured emission energy to zero. As mentioned above, we take the angle-integrated spectra provided by the original authors, and obtain total production cross sections using our calculated threshold corrections. These differences account for the different results we obtain compared to Axton. For instance, at 27.4 MeV we obtain an experimental alpha production cross section of 777 mb, compared to Axton's 431 mb. The importance of accounting for the large alpha emission cross section at low emission energies is clear. This resolves the discrepancy noted by Axton: his evaluated alpha production cross section here (760 mb) differed significantly from his integrated "experimental" UC-Davis result (431 mb).

UC-Davis measurements:					
Reaction	Incident energy (MeV)	Detector Threshold (MeV)	Experimental measurement (mb)	LLNL threshold correction (mb)	Total Production (mb)
$^{12}C(n, x\alpha)$	27.4	3.0	290.8 ± 3.1	486.0 ± 145.8	776.8 ± 145.8
	39.7	2.9	216.5 ± 2.3	239.0 ± 71.7	455.5 ± 71.7
	60.7	3.2	166.5 ± 2.4	148.0 ± 44.4	314.5 ± 44.4
$^{12}C(n, xp)$	27.4	3.0	57.2 ± 1.5	13.3 ± 4.1	70.5 ± 4.4
	39.7	1.8	93.9 ± 2.1	13.9 ± 4.2	107.8 ± 4.7
	60.7	2.1	126.7 ± 2.4	13.1 ± 3.9	139.8 ± 4.6
$^{12}C(n, xd)$	27.4	3.7	55.5 ± 1.5	8.1 ± 2.4	63.6 ± 2.8
	39.7	2.7	52.5 ± 1.2	5.9 ± 1.8	58.4 ± 2.2
	60.7	2.1	63.7 ± 1.2	3.8 ± 1.2	57.6 ± 1.7
Louvain-la-Neuve measurements:					
$^{12}C(n, x\alpha)$	42.5	12.0	25.9 ± 2.6	452.0 ± 135.6	477.9 ± 135.6
	62.7	15.0	19.2 ± 1.9	309.0 ± 92.7	328.2 ± 92.7
	72.8	9.0	43.4 ± 4.3	239.0 ± 71.7	263.5 ± 71.7
$^{12}C(n, xp)$	42.5	4.0	110.2 ± 5.5	28.3 ± 8.6	138.5 ± 10.2
	62.7	6.0	116.4 ± 5.8	43.0 ± 12.9	159.4 ± 14.1
	72.8	6.0	141.8 ± 7.1	37.7 ± 11.3	179.5 ± 13.3
$^{12}C(n, xd)$	42.5	6.0	63.6 ± 3.1	16.0 ± 4.8	79.6 ± 5.7
	62.7	10.0	46.1 ± 2.3	22.3 ± 6.8	68.4 ± 7.2
	72.8	8.0	62.4 ± 3.1	20.6 ± 6.2	83.0 ± 6.9

Table VIII: Experimental charged-particle production cross sections together with the low-energy LLNL threshold corrections, and the resulting total production cross sections

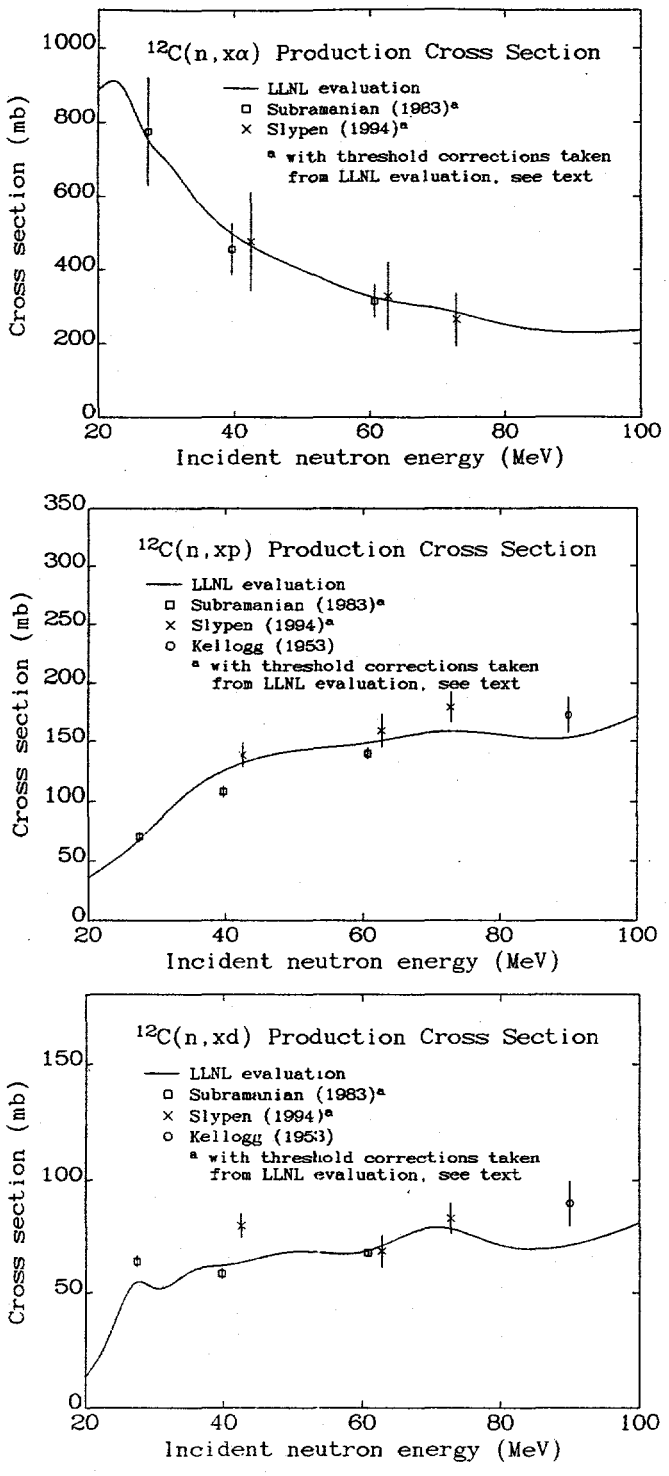

Figure 12: Total production cross sections for alphas, protons, and deuterons in the n+^{12}C reaction compared with measurements [26, 28, 27].

Before moving on to discuss our evaluated differential emission spectra, we show one more type of production cross section compared with our calculations: yields of $A > 4$ residual nuclei following neutron bombardment on carbon at 75 MeV. Such cross section measurements are often referred to as spallation yields, and while there is no data at this energy for neutron reactions, experimental data by Harrison *et al.* [25] do exist for the proton-induced reaction. Harrison *et al.* argued [25] that the spallation products from proton reactions at 75 MeV ought to be similar to those from neutron reactions since the incident energy far exceeds the Coulomb barrier, and $N = Z$ for the target. In Fig. 13 below we compare our calculated yields as a function of A, compared to the experimental data (which extend only up to $A = 11$). The agreement is seen to be reasonable: modeling of spallation yields is always more challenging than light-particle emission spectra calculations, and while there are some differences, we do represent the general features fairly well. Also, our results appear to describe the data more accurately than the INC with Fermi break-up model in Ref. [25]. As discussed earlier, we do not include these yield cross sections in our evaluated libraries (only the kinetic energy given to these nuclei).

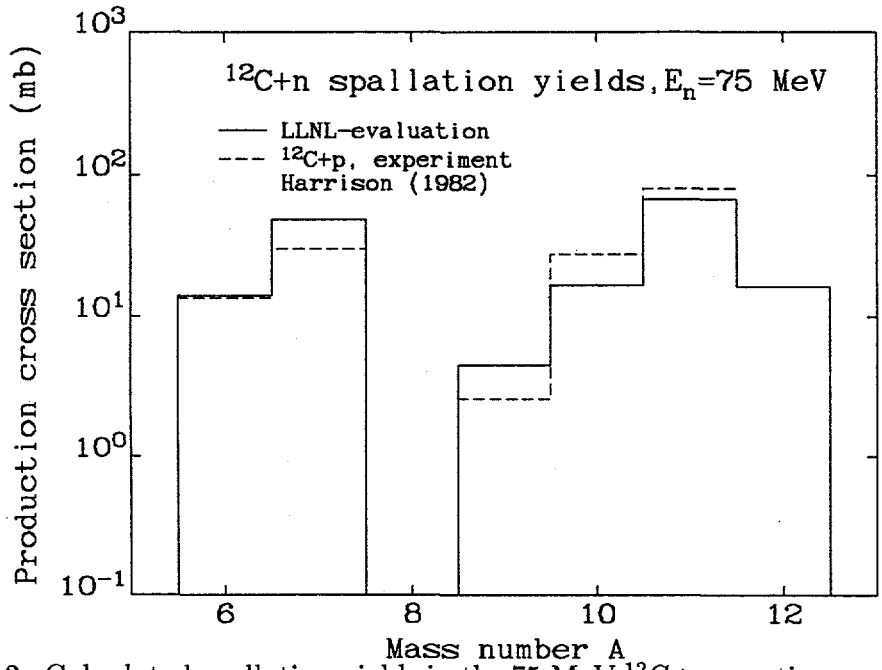

Figure 13: Calculated spallation yields in the 75 MeV ^{12}C+n reaction, compared with experimental *proton*-induced measurements [25].

6.3 Angle-Integrated Charged-Particle Emission Spectra

In Figs. 14-17 we show our calculated angle-integrated emission spectra of protons, deuterons, and alphas, compared with measurements. We show results at incident neutron energies of 27, 40, 60, and 70 MeV, which correspond approximately to the energies measured in the UC-Davis [17] and Louvain-la-Neuve [19] experiments. Generally the consistency between the various experimental measurements is good. Note, though, that the end-points of the Louvain-la-Neuve spectra extend a few MeV further than the other measurements due to the slightly higher incident energies used. In the case of alpha emission, the new Haight *et al.* measurements [27] (incident energies $\leq$ 40 MeV) are in good agreement with the other experiments.

Our results generally describe the full experimental emission spectra well. The only case where we deviate significantly from measurements is the 70 MeV ^{12}C(n, xp) reaction, where we underpredict the Louvain-la-Neuve measurements in the preequilibrium range. However, flux conservation prevented us from increasing the proton emission. If we did so, preequilibrium neutron emission would have had to be reduced to an unphysically small level. This indicates either a problem with the experiment, or possibly that multiple preequilibrium proton emission could be more significant than our calculations suggest. This is an important reaction since it is the main reason for the high Louvain-la-Neuve total kerma factor result at 72.5 MeV, which we underpredict (see Sec. 6.7).

That our angle-integrated calculations account for the measurements is particularly important for absorbed-dose calculations, since partial kerma factors are obtained from the average-energy of these spectra. In this sense a good description of experimental angle-integrated spectra is more important than accurately describing the angular variations. Still, in the next subsection we show how the double-differential emission spectra also agree well with measurements.

The structure seen in the calculations (particularly for deuteron emission) arises from the wide-spacing of low-lying residual nuclear levels – an experimental resolution width has not been folded into the calculations. This structure is even more evident in the double-differential spectra (see the next subsection); in the angle-integrated spectra it is partially washed out since a given channel emission energy corresponds to different laboratory energies for different angles.

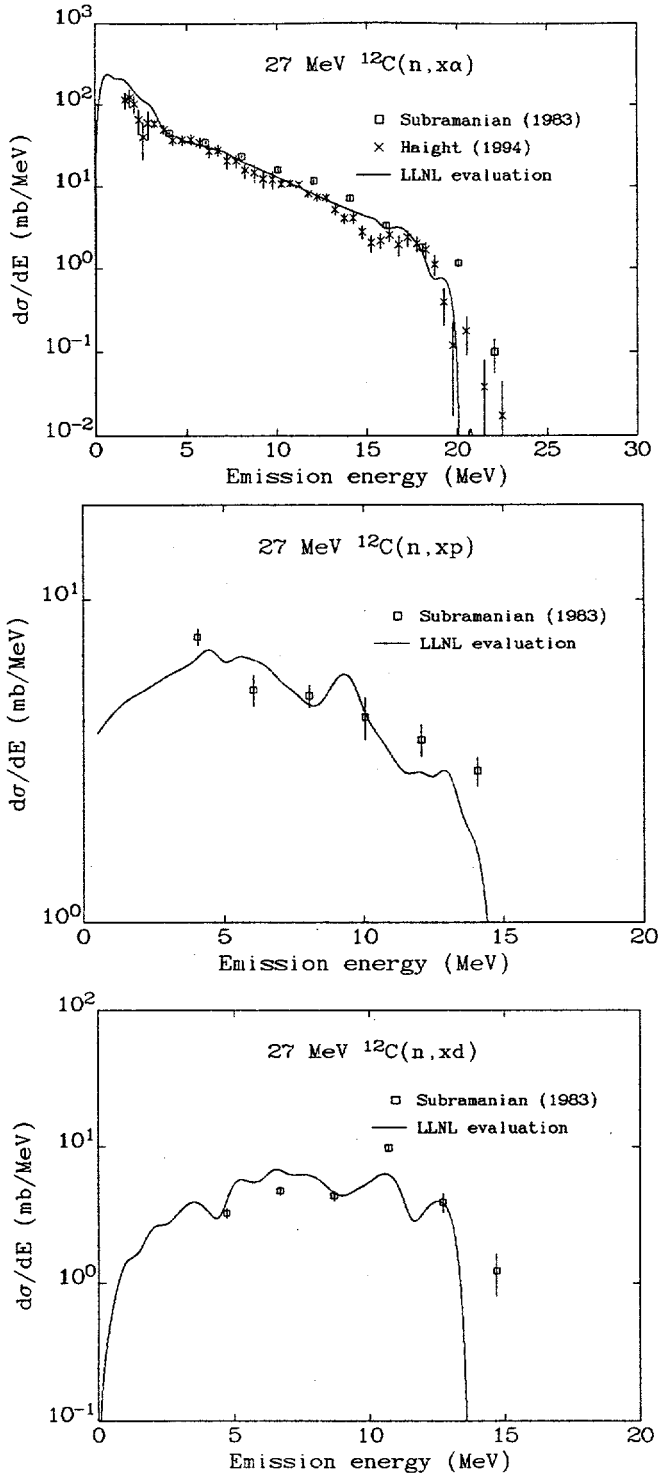

Figure 14: Angle-integrated 27 MeV n+^{12}C inclusive spectra (lab frame) for alpha, proton, and deuteron emission compared with measurements [26, 27].

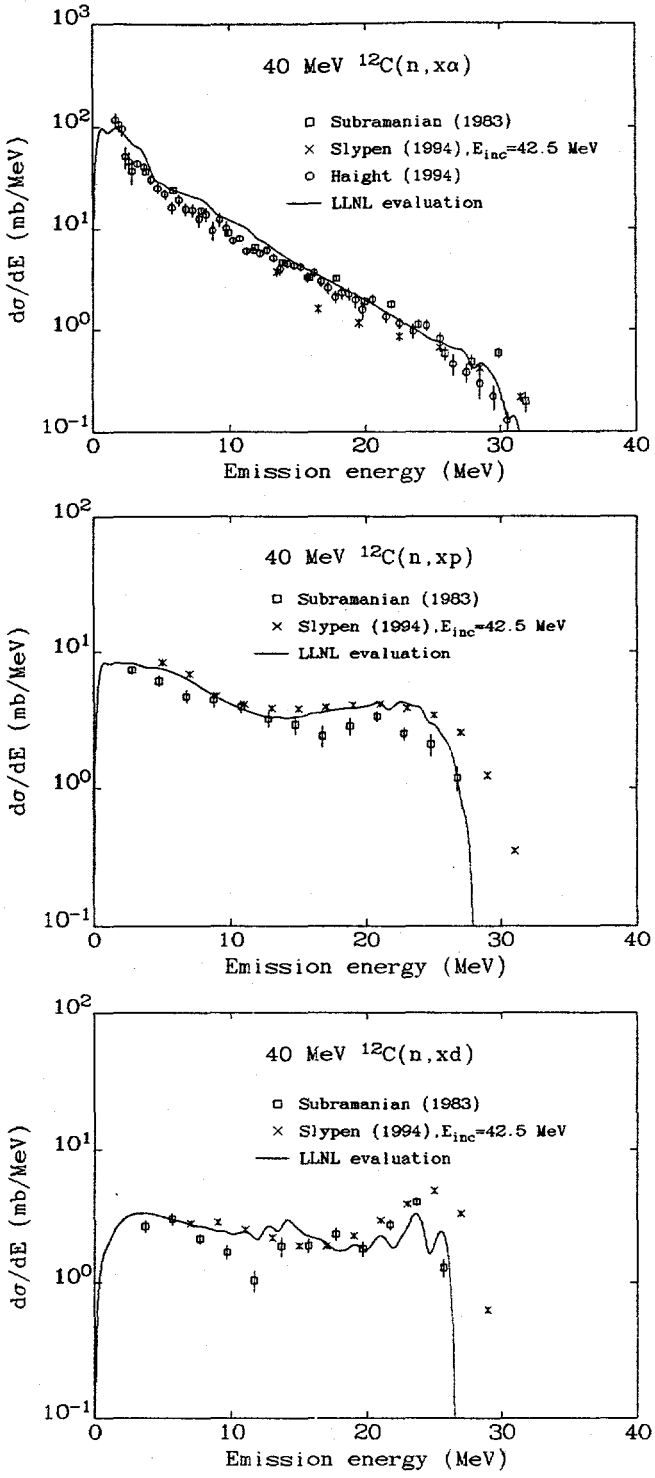

Figure 15: Angle-integrated 40 MeV n+^{12}C inclusive spectra (lab frame) for alpha, proton, and deuteron emission compared with measurements [26, 27, 28].

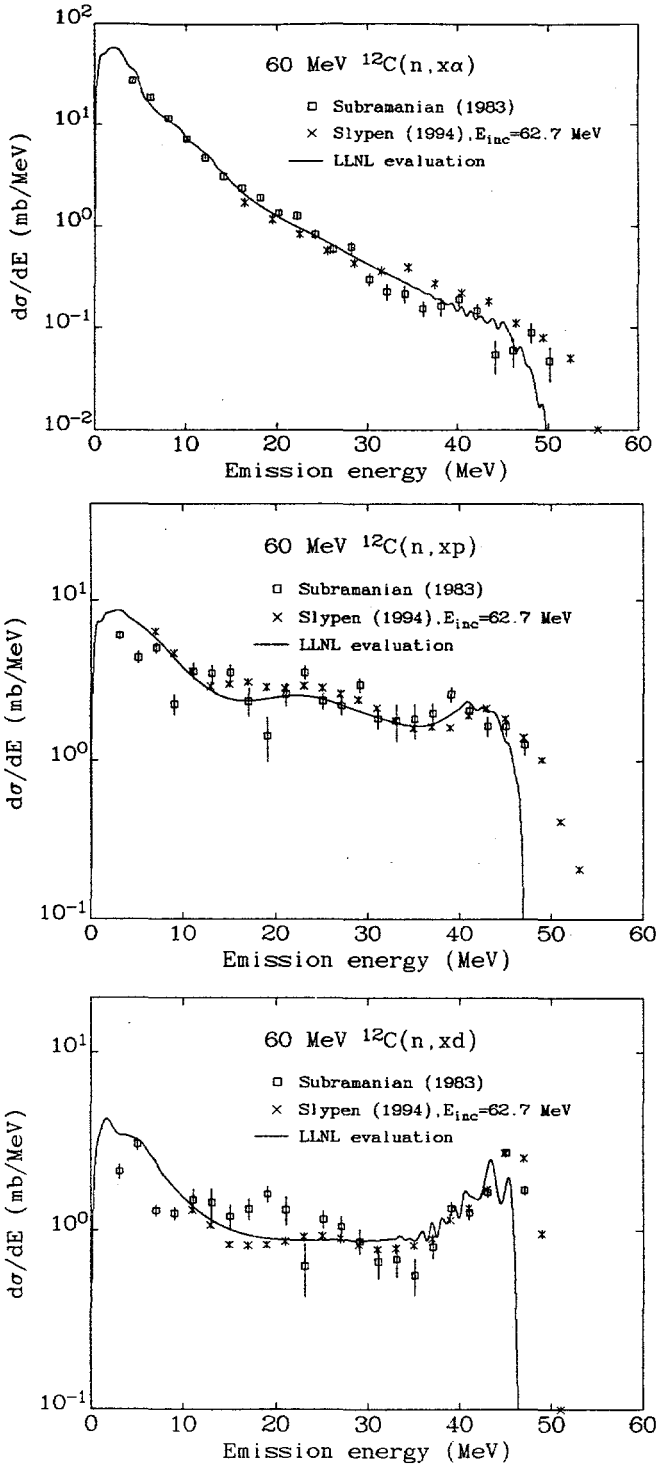

Figure 16: Angle-integrated 60 MeV n+^{12}C inclusive spectra (lab frame) for alpha, proton, and deuteron emission compared with measurements [26, 27, 28].

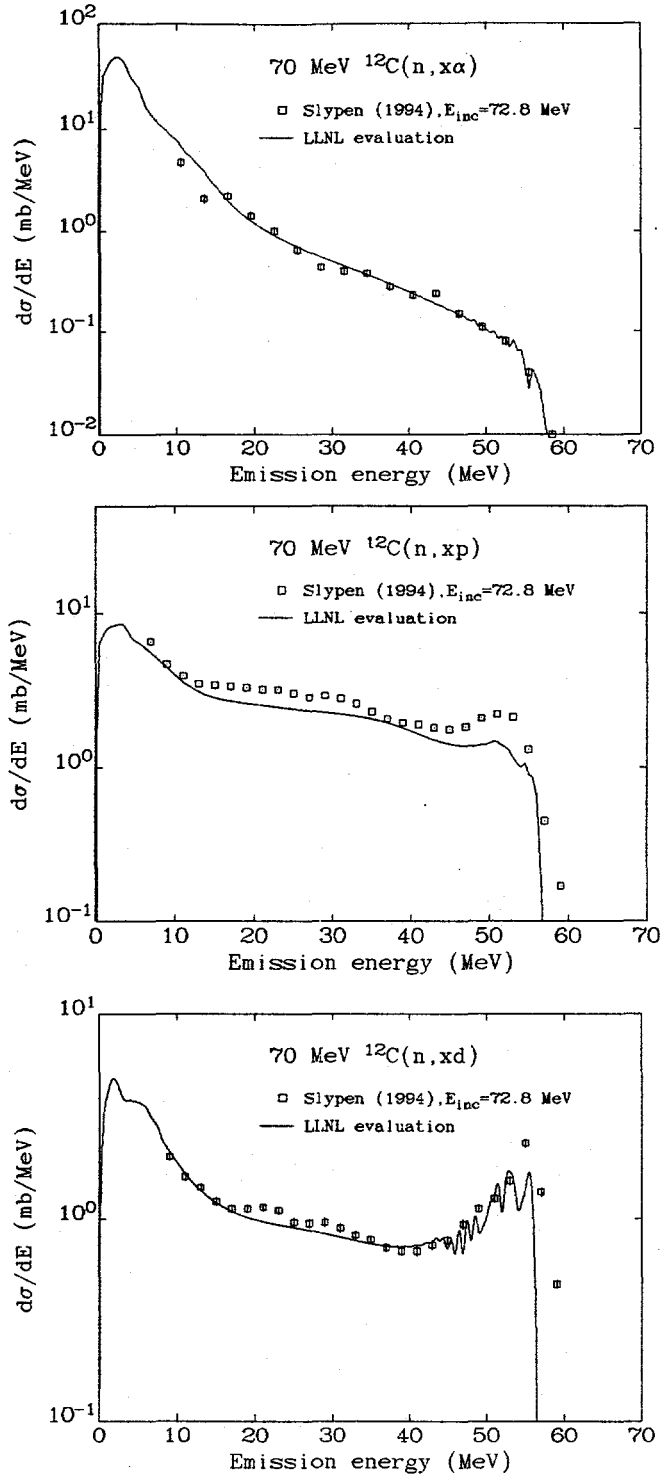

Figure 17: Angle-integrated 70 MeV n+^{12}C inclusive spectra (lab frame) for alpha, proton, and deuteron emission compared with measurements [26, 27, 28].

6.4 Double-Differential Charged-Particle Emission Spectra

In figures 18-20 we compare our calculated double-differential alpha, proton, and deuteron emission spectra against the UC-Davis measurements. The angles that we show are the same as those presented by Subramanian *et al.*, together with Brenner and Prael's calculations, in Ref. [17].

The high-energy structure that is seen in our calculations is due to the spacing of nuclear levels in the residual nucleus after first-particle emission. Our modeling of preequilibrium and direct reactions to these levels is seen to account for the measurements fairly well. A dramatic example of the influence of such nuclear structure is seen in the $^{12}C(n, xd)$ spectra, where the low-lying ^{11}B states populated after high-energy deuteron emission are widely separated in energy. Structure effects are also sometimes seen in the low-energy part of the emission spectra. These are due to particle-unstable excited nuclei decaying by equilibrium emission to low-lying or ground-state residual nucleus levels. For example, the two low-energy peaks seen in the alpha emission spectra at forward angles are due to the ground-state and first excited-state of ^{8}Be decaying to two alpha-particles. Since we have not included the finite widths of these states in our analyses, the structure is more dramatic than is observed experimentally. Likewise, the structure seen in the low-energy deuteron emission in Fig. 18 is due to the decay of the 1st excited state of ^{6}Li into α+ d.

Our calculations generally account for the angular variations that are seen in the data, showing that the phenomenological systematics of Kalbach provide a good representation of angular distributions. There is a tendency, though, for the backward-angles to be underpredicted for the 60 MeV incident energy, though the practical consequences of this underprediction are small. At the higher emission energies the spectra show a dramatic forward peaking, typical of preequilibrium and direct reactions, since the incident projectile's direction of motion is partially preserved. At the lowest energies, the particles are emitted from compound nucleus reactions. In the center-of-mass these are emitted with angular distributions symmetric about 90-degrees (and almost isotropic), but in the laboratory frame there remains a small amount of forward-peaking. Our calculations also clearly show how discrete structure effects in the spectra track with emission angle and energy due to kinematics.

It is instructive to compare our results with the Brenner and Prael calculations [17], which used an INC code with Fermi break-up. Overall, our calculations model the double differential data more accurately than those of Brenner and Prael: for alpha emission, the quality of agreement with data is equivalent; and for proton and deuteron emission our results are generally better. Note that the any structure present in the high-energy Brenner and Prael results is not due to nuclear level effects (they did not include direct reactions to discrete low-lying levels); rather, it is statistical and results from their use of Monte Carlo techniques. Our calculational method is

deterministic so that our results do not show such fluctuations.

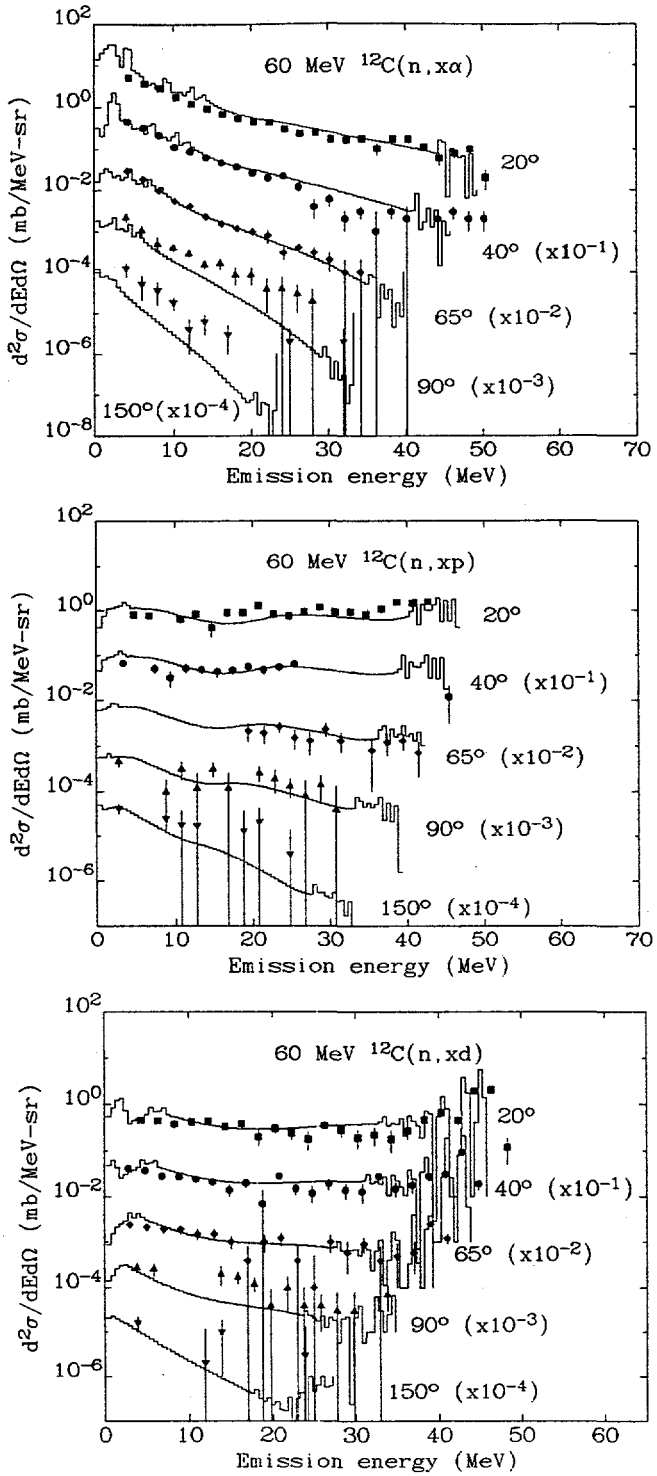

Figure 18: Double-differential 60 MeV n+^{12}C inclusive spectra (lab frame) for alpha, proton, and deuteron emission compared with UC-Davis measurements [17].

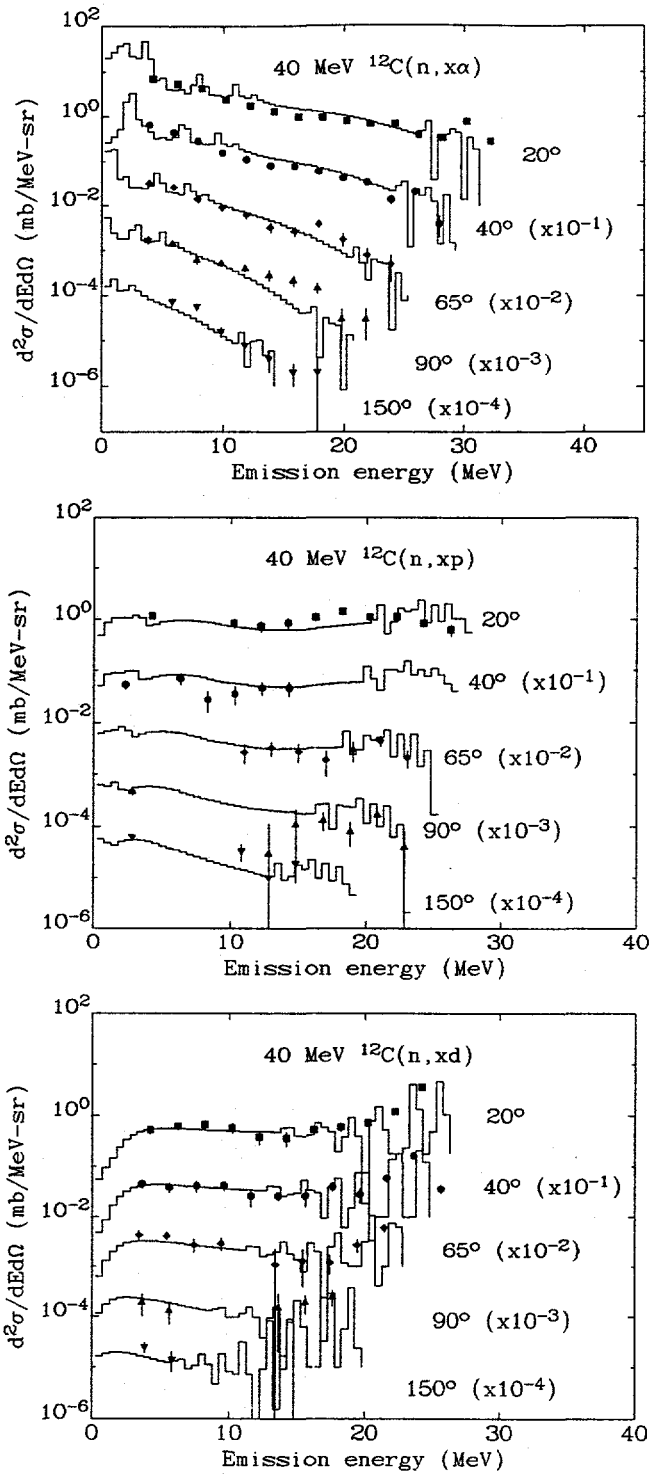

Figure 19: Double-differential 40 MeV n+^{12}C inclusive spectra (lab frame) for alpha, proton, and deuteron emission compared with UC-Davis measurements [17].

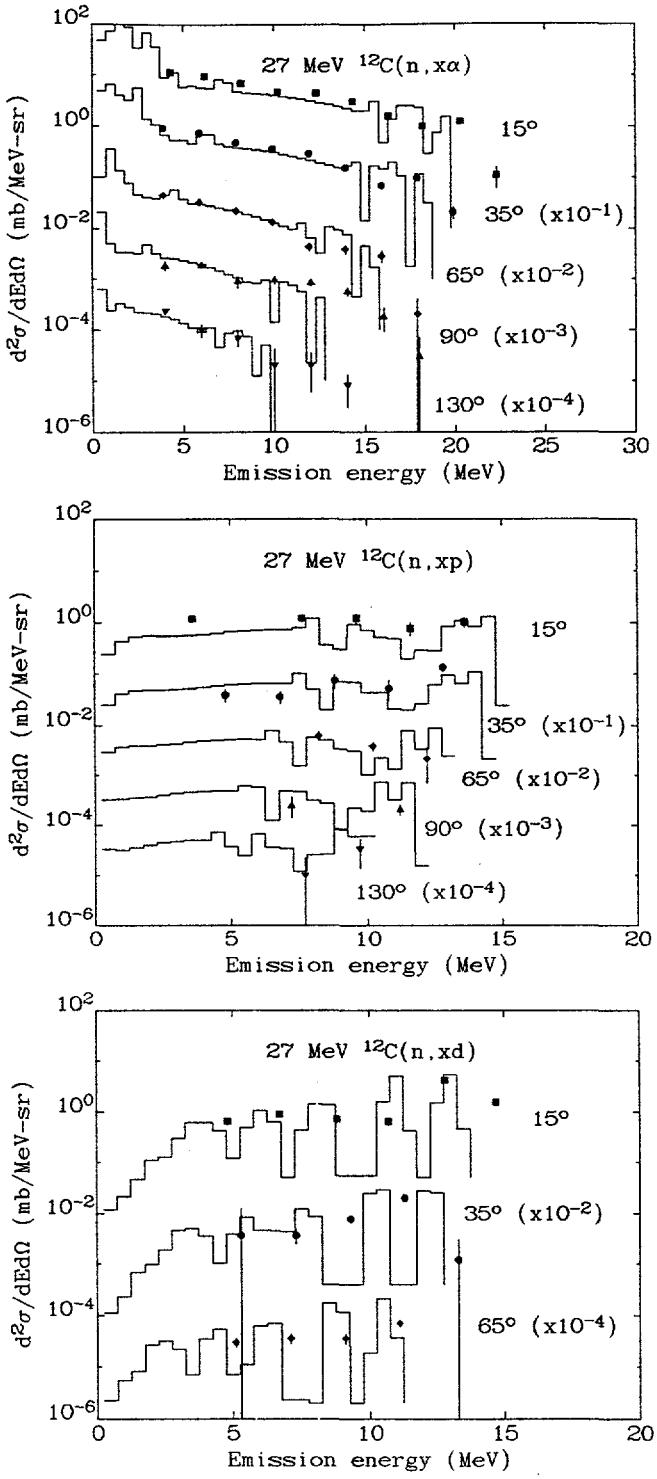

Figure 20: Double-differential 27 MeV n+^{12}C inclusive spectra (lab frame) for alpha, proton, and deuteron emission compared with UC-Davis measurements [17].

6.5 Neutron Emission Compared With (p,xp) Data

Unfortunately there are no experimental measurements of the (n, xn) emission spectra with which we can compare our calculations. However, Bertrand and Peelle have measured $^{12}C(p, xp)$ cross sections at 40 and 60 MeV. It would be expected that $^{12}C(p, xp)$ and $^{12}C(n, xn)$ spectra should be similar, particularly for the higher emission energies where Coulomb effects are negligible. Some differences would be expected due, for instance, to different Q-values in the competing channels in the two cases, but we expect such effects to have a small impact. Therefore we have used the Bertrand and Peelle measurements to benchmark our neutron emission calculations. An example is shown in Fig. 21 below, where we compare our results against the 40 MeV angle-integrated measurements. The calculated emission spectrum agrees very well with data except at the lowest energies, where the calculation lies below the measurements. This could be due to the different multiple compound nucleus decay sequences for these two reactions. The prominent high emission-energy peak is due to the strong excitation of the 4.4 MeV state in carbon inelastic scattering, and Fig. 21 shows that such processes are similar for (n, n') and (p, p') reactions.

For energies where (p, xp) data do not exist we have been guided by systematics, which show that the (n, xn) differential cross section is about twice the (n, xp) cross section in the preequilibrium regime due to phase space factors (see Sec. 2).

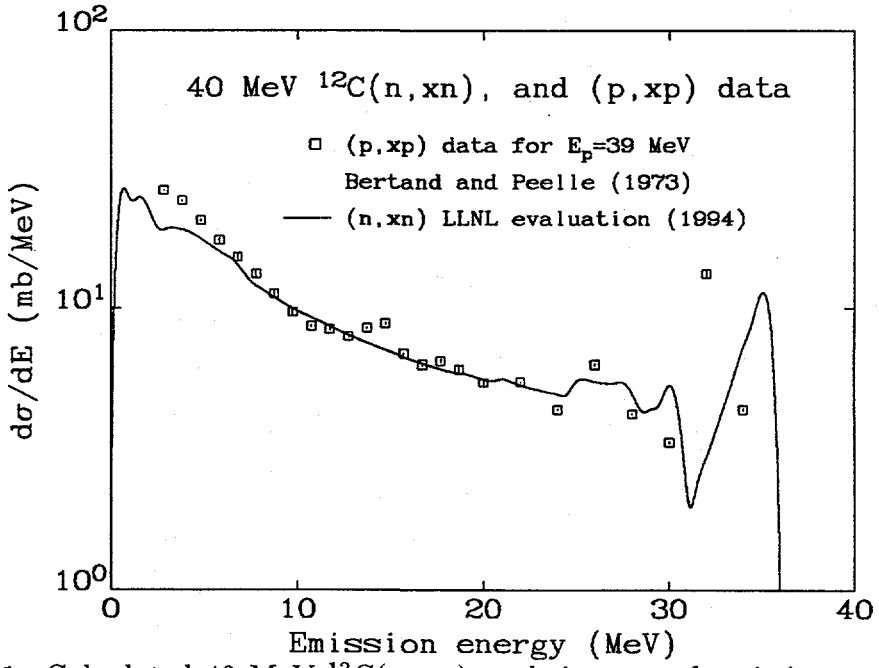

Figure 21: Calculated 40 MeV $^{12}C(n, xn)$ angle-integrated emission spectrum compared with $^{12}C(p, xp)$ data [22]

6.6 Gamma-Ray Production Spectra

A measurement of the gamma-ray emission spectra at 60 MeV by Auchampaugh *et al.* [21] at Los Alamos is compared against our calculations in Fig. 22. These (unpublished and preliminary) experimental results are at an emission angle of 90 degrees, and are seen to agree very well with our calculation.

The structure seen in both the measurements and the calculation is due to the dominance at these energies of discrete gamma-rays from low-lying bound nuclear states. The individual strengths of the various gamma-ray lines are closely related to the production cross sections of the various residual nuclei, and modeling such production cross sections provides a stringent test for the theory. For example, the peak in the spectrum at 4.4 MeV is due in part to the de-excitation of the 4.4 MeV state in ^{12}C following neutron inelastic scattering, and the fact that our calculations describe this measurement well provides support for the accuracy of our coupled-channel calculations.

Similar gamma-production data for neutron reactions on lead, for energies up to 200 MeV, demonstrated the importance of multiple preequilibrium processes, and appropriate high-energy level density formalisms, in the GNASH code [64]. When new LANL results [97] become available for gamma-ray production on carbon and oxygen, they will be useful for further checking our calculations.

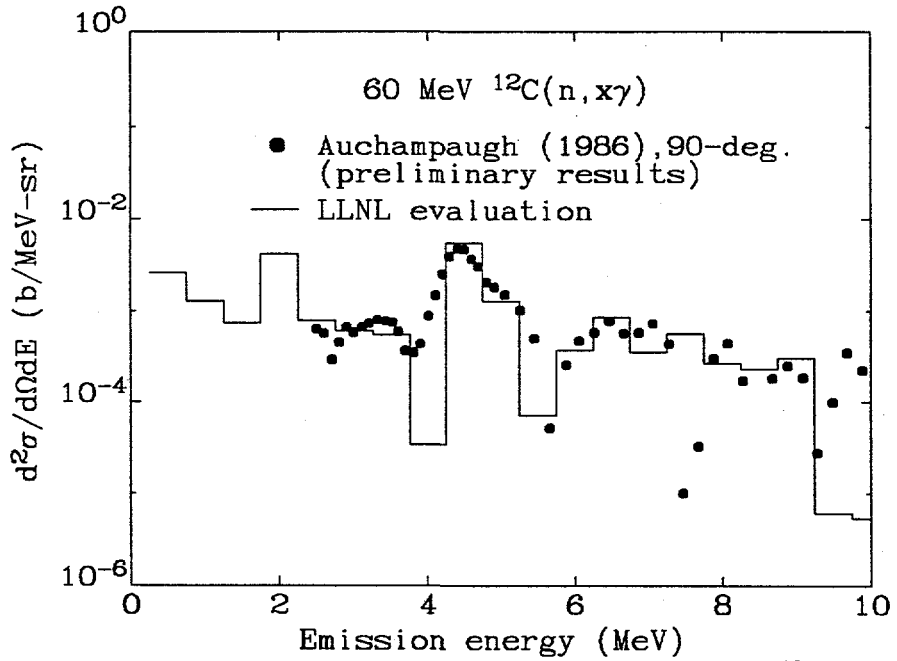

Figure 22: Spectrum of gamma rays emitted in the 60 MeV ^{12}C$(n, x\gamma)$ reaction, compared with measurements at 90-degrees [21]

6.7 Kerma Factors

In Table IX we show our calculated partial and total kerma factors based on our evaluated cross section libraries. As described in Sec. 4, the light charged-particle contributions are derived from the (laboratory frame) evaluated emission cross sections, the elastic recoil kerma from our calculated elastic scattering cross sections using relativistic kinematics, and the nonelastic recoil kerma were evaluated on the basis of results from the energy balance method and model calculations.

Energy (MeV)	p	d	α	nonel. recoils	el. recoils	Total (f Gy m^2)
20	0.12	0.04	1.82	0.65	0.52	3.15
23	0.19	0.12	2.15	0.65	0.44	3.55
27	0.34	0.33	2.11	0.58	0.42	3.78
30	0.51	0.35	2.18	0.55	0.39	3.98
35	0.84	0.50	2.06	0.45	0.35	4.20
40	1.12	0.63	1.92	0.45	0.32	4.44
50	1.52	0.88	1.70	0.47	0.25	4.82
60	1.95	1.04	1.43	0.50	0.21	5.13
70	2.46	1.32	1.42	0.45	0.18	5.83
80	2.93	1.34	1.29	0.40	0.16	6.12
90	3.00	1.44	1.28	0.35	0.14	6.21
100	3.10	1.64	1.42	0.30	0.13	6.59

Table IX: Evaluated partial and total kerma factors for n+^{12}C, for various laboratory neutron energies.

The various calculated partial and total kerma factors given in Table IX are shown in Fig. 23 as a function of the incident neutron energy. It is easy to understand the general variation of the total kerma factor with incident energy. Between 20 and 100 MeV the kinetic energy available to the reaction products increases by a factor of approximately 5 (ignoring nuclear reaction variations in the averaged Q-value with energy). However, the nonelastic cross section decreases by a factor of 2.2 over this energy range. Since nonelastic processes dominate the contributions to the total kerma factor, which is proportional to the average ejectile energy, multiplicity, and the nonelastic cross section, a very rough estimate of the factor change in the total kerma factor between 20 and 100 MeV is $5/2.2 = 2.3$, which is in reasonable agreement with our calculation.

At the lowest energies, the total kerma factor is dominated by the alpha contribution, much of which comes from the 3α beak-up mechanism. The large production cross section for alphas at these energies, which follows from the large multiplicity (three), results in this large partial kerma. As the neutron incident energy increases the 3α break-up cross section falls (since other reaction mechanisms, such as pro-

ton preequilibrium emission, and multiple preequilibrium emission increase in importance), resulting in a decreasing alpha kerma factor. The increasing proton and deuteron partial kerma factors are due to the importance of preequilibrium emission with increasing incident energy. The elastic and nonelastic recoil kerma factors, on the other hand, decrease with increasing energy. This is because the $A < 4$ angular distributions become increasingly forward-peaked with incident energy, resulting in a reduced kinetic energy to the recoils (even though the incident energy is increasing). The decreasing integrated elastic and nonelastic cross sections over the 20-100 MeV energy range also impact upon the kerma factors. We compare our calculated elastic partial kerma factor with experimental measurements in Fig. 24.

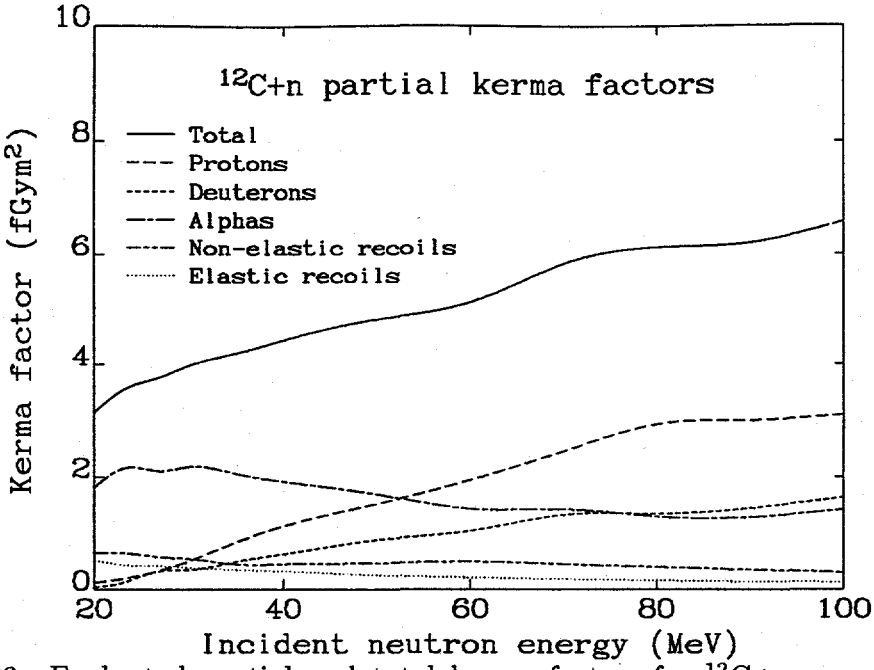

Figure 23: Evaluated partial and total kerma factors for ^{12}C+n, as a function of incident energy.

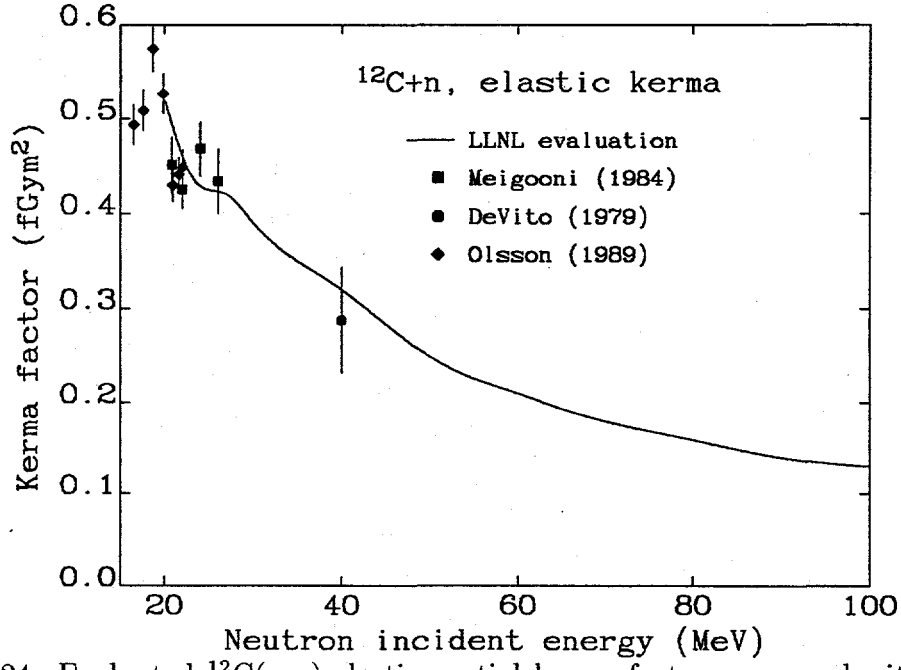

Figure 24: Evaluated ^{12}C(n,n) elastic partial kerma factor compared with measurements [81, 82, 80].

In Fig. 25 we show our evaluated total kerma from 20-100 MeV (obtained from our microscopic cross section libraries) compared with experimental measurements [37, 98, 99, 100, 39, 34, 78, 19]. For comparison we show in Fig. 26 the Livermore total kerma factors obtained by Howerton [6] from the ENDL data libraries below 20 MeV, compared with measurements [101, 102, 103, 104, 98, 105, 106, 107, 100, 108, 109]. At 20 MeV our evaluation matches onto this work. There are two different types of measurements of total kerma factors: direct measurements of the ionization effects of the charged particles using a proportional counter; and indirect determination from cross section measurements. Below we describe these two methods and note some of the uncertainties inherent in them.

The direct kerma measurements recently reported by Schrewe *et al.* [39], for incident energies between 30 and 70 MeV, use a proportional counter to measure the total kerma factors. Such experiments, however, are very difficult to perform and the uncertainties reported are fairly large. Recently, further measurements have been reported by Schrewe *et al.* [40] which are fairly consistent with their earlier results, though a small upward correction to the old numbers was obtained.

Experimental kerma factors obtained from cross section measurements have been presented by the UC-Davis group and the Louvain-la-Neuve group. These experiments measured the inclusive production cross sections of light charged particles, for emission energies above the detector thresholds. To obtain the total kerma factors, additional assumptions have to be made: (1) angle-integrated spectra need to be inferred from the double-differential measurements; (2) the cross sections have to be extrapolated from the threshold energy measured to zero energy; (3) elastic recoil kerma have to be added; and (4) the (unmeasured) contributions from nonelastic recoil fragments have to be estimated. There is some ambiguity in determining the experimental total kerma factors due to uncertainties in these additional corrections. For instance, a range of total kerma factors based upon the UC-Davis measurements have been reported in the literature. Brady *et al.* [18] initially gave experimental total kerma factors based upon the uncorrected experimental measurements. Later, Dimbylow [34] added contributions due to nonelastic recoils, as well as low emission energy threshold corrections, as estimated by Brady *et al.* [18]. In a subsequent work, Romero *et al.* [78] further refined the estimated experimental total kerma factors by assuming an extrapolation to zero emission energy, and a nonelastic recoil contribution, based upon the model calculations of Brenner and Prael. Therefore we believe that there are some significant uncertainties estimating the total kerma factors from the cross section measurements, and the error bars on the UC-Davis results are probably too small. Likewise, the corrections that are added to the "raw" Louvain-la-Neuve results are very large and there are significant uncertainties involved.

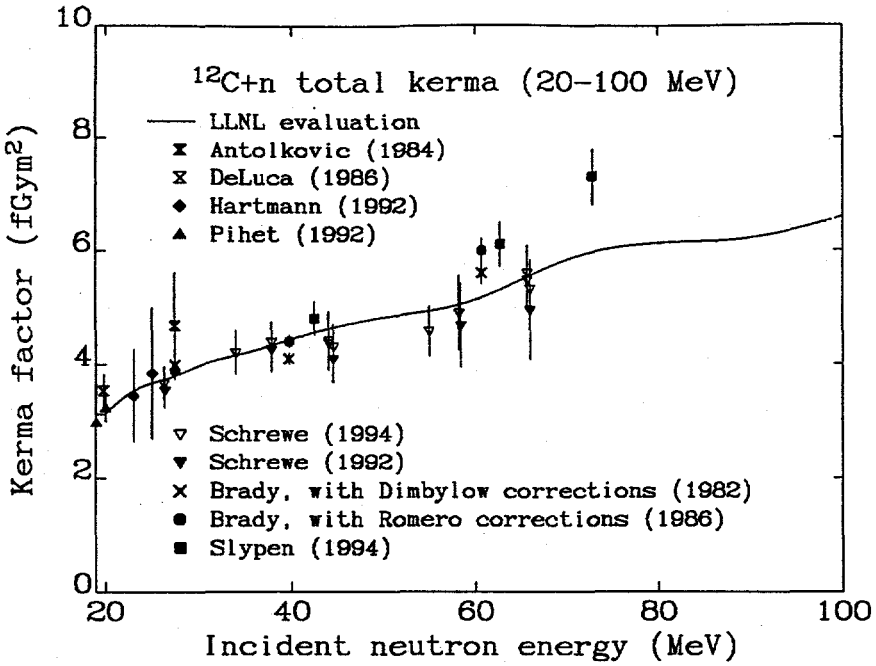

Figure 25: Evaluated total kerma factor, from 20-100 MeV, compared with experimental measurements.

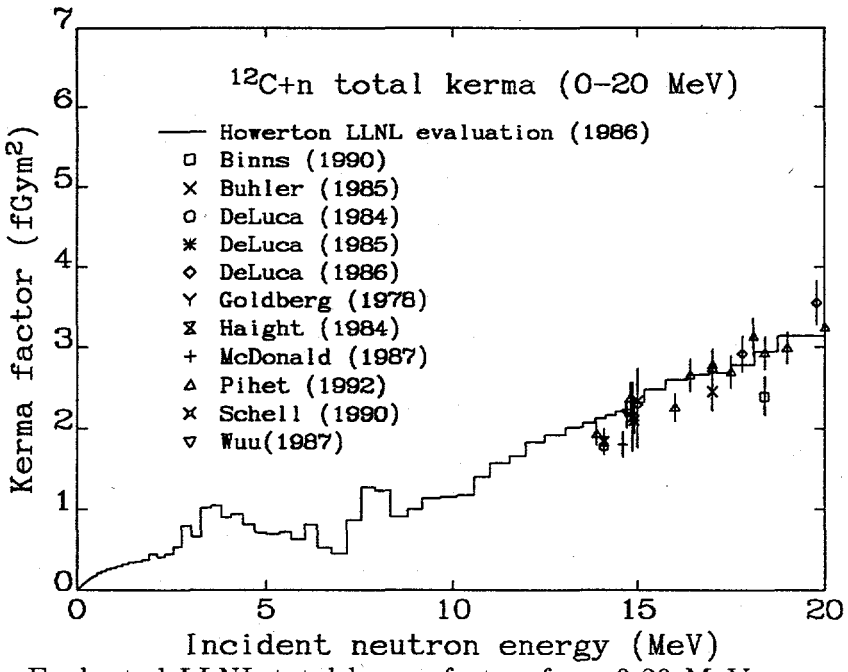

Figure 26: Evaluated LLNL total kerma factor, from 0-20 MeV, compared with experimental measurements.

Figure 25 shows that the kerma factors resulting from our evaluations are in good agreement with the experimental measurements. Above 40 MeV there appears to be a difference between the total kerma factors determined from the cross section measurements (from UC-Davis and Louvain-la-Neuve), and from the proportional counter measurements; the former are somewhat higher. Our evaluation yields kerma factors intermediate in value between these two types of measurements. The general consistency seen in Fig. 25 between our evaluation and the measurements provides an important integral benchmarking of our libraries. The kerma is closely related to the absorbed-dose following neutron interactions with carbon nuclei, and it is important to model it accurately when calculating absorbed dose in radiotherapy. Our calculated kerma factor at 73 MeV is lower than the Louvain-la-Neuve measurement. This is due to the lower differential proton emission cross section calculated, compared to experiment, as seen in Fig. 17. But we were unable to increase the calculated preequilibrium proton emission spectrum without violating systematics generally observed in the partitioning of the reaction flux among fast neutron and proton ejectiles.

There is also a difference between our evaluation and the kinematically-complete emulsion experiment of Antolkovic *et al.* at 27 MeV [37] (see also our discussion in Sec. 7). Instead, our result agrees well with the other kerma factor measurements near this energy by Brady *et al.* [34, 78], Hartmann *et al.* [99], and Schrewe *et al.* [39], as seen in Fig. 25. Antolkovic determined the total kerma factor here by adding her result for the $(n, 3\alpha)$ partial kerma (averaged with Antolkovic's estimate of the UC-Davis value), with the UC-Davis measurements of the other partial kerma factors, and obtained a total kerma factor which is significantly larger than our result (though our result is almost within her assigned uncertainty). The reason for the discrepancy is due to the fact that the partial kerma factor to the $(n, n'3\alpha)$ reaction is significantly higher than our result. This is because (a) her $(n, n'3\alpha)$ cross section exceeds ours; (b) her average alpha-particle kinetic energy exceeds ours. Regarding (a) above, Brenner and Prael [110] have re-estimated the corrections that must be made to obtain this value, and argue for a 15 % smaller $(n, n'3\alpha)$ cross section here. As for (b), our alpha emission spectrum is in good agreement with the measurements from Los Alamos and UC-Davis here (see Fig. 14), which we believe to be probably of higher accuracy than those from the emulsion experiment. Finally we note that since the Antolkovic alpha spectrum at 26 MeV differs so much from the Los Alamos and UC-Davis spectrum at 27 MeV (compare Fig 14 with Fig. 2 of Ref. [37]), the Antolkovic threshold correction to the Davis data is probably too high (our estimate of the UC-Davis alpha partial kerma factor for alpha production is 2.1 compared to Antolkovic's 2.6 fGym62.) If we repeat Antolkovic's procedure for obtaining her total kerma factor at 27 MeV, but use our estimation of the Davis threshold correction, along with the Brenner 15% reduction in the $(n, n'3\alpha)$ cross section, we obtain an average alpha partial kerma factor of 2.2 and a total "experimental" kerma factor of

4.2 fGym62 in better agreement with the other measurements near 27 MeV.

Our calculated total kerma factor is in good agreement with the 1992 evaluation by White *et al.* [7], with our results being slightly higher at the higher energies. In Fig. 27 we show our results compared with other calculations and measurements. The other model calculations we show generally describe the measurements fairly well, though the Brenner and Prael [41] and the Wells [33] calculation appear rather low, and the rapid rise seen in the Behrooz calculation [31] seems unjustified. The results of Alsmiller *et al.* [30], Dimbylow [34], and Watanabe *et al.* [61], agree fairly closely with our work. The spread in the experimental kerma factors above 50 MeV makes it difficult to critically compare the various results from model calculations. Clearly, there remains a need for further total kerma factor measurements at these energies to resolve these discrepancies.

We also note that our kerma evaluation differs significantly from the recent work of Axton [8]. Axton extended the evaluated ENDF data from 20 MeV up to 32 MeV, by making certain assumptions concerning the shape of the partial cross sections up to 32 MeV. Later in Sec. 7 we shall describe in detail the differences between our work and that of Axton. But we note here that differences in total kermas come mainly from two factors: the partial cross sections; and the average energy given to alphas. An example of cross section differences is that we do not find any evidence for the importance assigned by Axton to exotic decay processes such as ^{12}C(^{6}Li,^{7}Li) break-up. At 26 MeV, for instance, Axton assumed that 100 mb (equivalent to about 20% of the nonelastic cross section!) goes into this channel, and contributes to about 10% of the total kerma factor. Regarding the average kinetic energy given to alphas, which determines the alpha partial kerma factor, this is determined in Axton's work by the excitation energy distribution of excited carbon states following inelastic neutron scattering (which decay by 3α break-up), along with the cross section passing through excited ^{9}Be states. Axton's result for the average alpha energy is in good agreement with the Antolkovic emulsion experiment result [37]. However, this measurement differs significantly from the UC-Davis and Los Alamos emission spectrum measurements which are consistent with each other, and which we think are more reliable.

The extent to which non-elastic recoil kerma is important remains an open question. Our results are approximately consistent with the energy-balance estimates of Brady *et al.*. Our estimates suggest that at 60 MeV and 27 MeV, for example, the non-elastic recoil kerma accounts for about 10 % and 15 % respectively of the total kerma. These values are comparable with those calculated by Brenner and Prael [78]. Yet a calculation by Harrison *et al.* [25], using a reaction model very similar to that of Brenner and Prael, gave non-elastic kerma factors which are 2-3 times larger. Such a large non-elastic recoil kerma factor, when considered along with the $A < 4$ kerma measured at UC-Davis and Louvain-la-Neuve, would further increase the discrepancy

with the direct total kerma measurements of Schrewe [40].

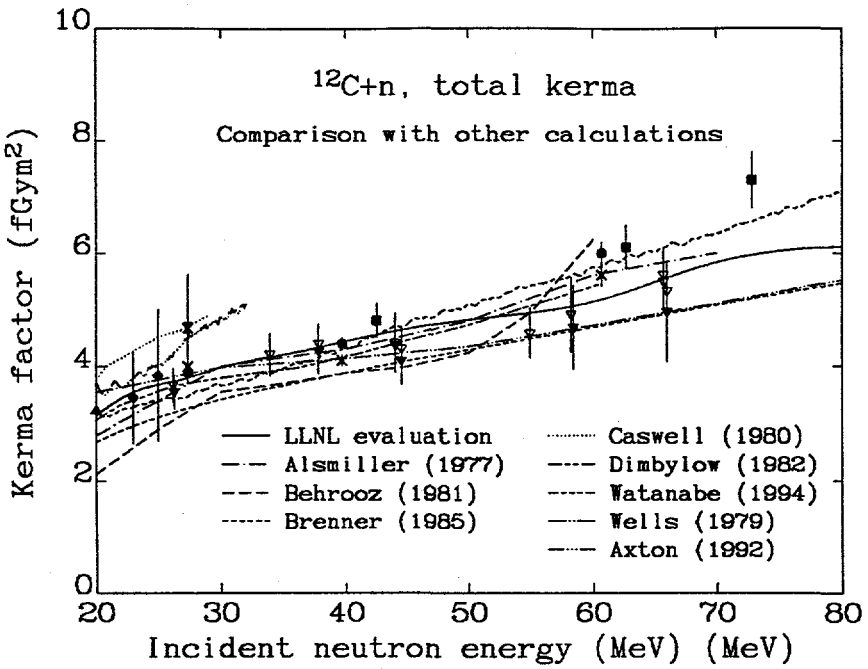

Figure 27: Evaluated total kerma factor, from 20-80 MeV, compared with results from other calculations.

7 Comparison with ENDF/B-VI and Exclusive Data

7.1 Introduction

While the present evaluation represents reactions in terms of inclusive emission spectra, it is useful to compare our calculated exclusive cross sections with measurements and the ENDF/B-VI evaluation, which extends up to 32 MeV. The evaluation of natural carbon for ENDF/B-VI was performed recently by Fu, Axton, and Perey [9], with the extensions from 20–32 MeV being done by Axton [8]. In a NIST report [8], Axton presented a very comprehensive description of his evaluation methodology and results, for both cross sections and kerma factors.

In Table X below we show our calculated exclusive reaction cross sections for the main break-up channels up to 30 MeV. Above this energy the number of such channels becomes too large to practically extract this information from our calculations. As stated earlier we have omitted triton and helium-3 emission processes in our model calculations since their cross sections are small.

Energy (MeV)	(n,n′)	(n,2n)	(n,p)	(n,d)	(n,np)	(n,α)	(n,n'3α)
20	122	0	29	13	7	20	289
23	97	1	23	28	24	12	298
27	69	4	21	52	45	5	252
30	58	8	23	46	55	3	228

Table X: Calculated exclusive reaction cross sections (in mb) for n+^{12}C up to 30 MeV, for the most important reaction channels.

It is particularly important for us to compare our calculations against the ENDF/B-VI evaluation, since our results are significantly different. The various partial (exclusive) cross sections we obtain in the 20-30 MeV region are quite different to those of Axton, and our calculated total kerma factor is dramatically lower (almost 20% lower at 30 MeV). The main reason for these differences is that there exist very limited experimental measurements for inelastic cross sections in this energy range – only $(n, n'3\alpha)$, $(n, 2n)$, and (n, n') inelastic scattering to low-lying levels. The other partial cross sections have to be estimated in some way, and our methods for doing this differ from Axton's.

Below we describe the ENDF/B-VI evaluation in some detail, and the reasons for our differing results. We will argue that Axton underestimated (n, p), (n, d), and (n, np) partial cross sections and the large importance he assigned to the ^{12}C$(n,^{6}$Li$)^{7}$Li channel channel is unjustified. We will also argue that Axton's evaluated total kerma factor is too high in the region 26-32 MeV.

7.2 Comparison with ENDF/B-VI above 20 MeV

7.2.1 Total, elastic, and reaction cross sections

Before discussing inelastic cross sections, we first briefly compare our results for the total, elastic, and reaction cross sections. The total cross section in our work is obtained from the recent high-accuracy measurements by Finlay *et al.* [23], which have a reported uncertainly of less than 1%. This work was published after Axton's evaluation, and has a total cross section lower than Axton's by 1.7 – 2.8 % over the 20 - 30 MeV range. Our elastic cross section is within 5% of Axton's. But our reaction (nonelastic) cross section deviates more significantly, with differences ranging from 3 – 16 %. The largest difference in reaction cross section (16 % at 27 MeV) is due to 2 reasons: (1) Since the Finlay total cross section at 27 MeV is 38 mb lower than Axton's, our inferred reaction cross section (i.e. total – elastic) is lower. This accounts for about half of the 16 % difference; (2) the other half of the difference is because our elastic cross section exceeds Axton's by 33 mb at 27 MeV. As we described earlier, our reaction and elastic cross sections are taken from a coupled channel optical potential calculation, and are not the result of an evaluated fit to integrated data. Still, as seen in Fig. 10 our results do agree fairly well with the data.

7.2.2 The case against the ENDF/B-VI ^{12}C(n,^{6}Li)^{7}Li channel

It is the Axton inelastic partial cross sections which differ most significantly from our results. In the 20-30 MeV range we obtain much larger (n,p), (n,d), and (n,np) cross sections compared to Axton, and find no evidence for the ^{7}Li – ^{8}Li break-up that Axton introduced. In order to understand why our inelastic exclusive cross sections and kerma factors deviate so greatly from Axton's evaluation, it is necessary to describe his evaluation methodology: Where experimental data exist ($(n,n'3\alpha)$, $(n,2n)$, and (n,n') inelastic scattering to low-lying levels), they were used. However, the sum of these cross sections added up to less than the nonelastic cross section (which was inferred from the total – elastic cross section), and therefore cross section to other energetically-allowed channels had to be found. He introduced a procedure for estimating the energy-dependence of unmeasured partial cross sections: assign a peak energy position a few MeV above threshold, and then assume an exponentially decaying excitation function, with peak cross sections and decay exponents based upon some systematics. Axton appreciated the uncertainties inherent in this approach – and use of this procedure yields very different results compared to our model calculations: we think this method significantly underestimates (n,p), (n,d), and (n,np) cross sections above 20 MeV.

As well as the above procedure, Axton also used his derived total production cross section from the UC-Davis measurements at 27.4 MeV as a guide. However,

our results indicate that this led to problems too (we obtain larger "experimental" UC-Davis production cross sections), since Axton used these total production cross sections as a guide to the upper limits on partial cross sections involving protons and deuterons. To obtain total "experimental" production cross sections, one has to provide threshold corrections to the UC-Davis data. Axton did this by assuming a constant differential cross section from the lowest measured emission energy to zero. We, however, use our model calculation low-energy results for this and obtain very different results: at 27.4 MeV we obtain (see Table VII) total "experimental" UC-Davis production cross sections for p, d, and α emission of 71,64, and 736 mb, compared to Axton's 52, 35, and 431 mb. The large difference in our alpha production cross section is due primarily to the fact that our model calculation gives a large amount of low-energy alpha emission from ground-state and low-lying state decays of ^{8}Be nuclei (see Fig. 14). But threshold corrections cannot account for the proton and deuteron differences, since Fig. 14 suggests that our threshold corrections here would be *smaller* than Axton's. These differences must be due to differences in the energy and angle integrations. As described in Sec. 6.2, we have relied on the UC-Davis (unpublished) integrations [26]; the reason for the discrepancy with Axton here is not understood.

Perhaps the most controversial consequence of Axton's evaluation methodology is the large importance assigned to the ^{12}C(n,^{6}Li)^{7}Li channel. At 26 MeV he assigned a peak cross section of 100 mb here, about 20 % of the nonelastic cross section. We shall explain how Axton arrived at this result, and argue why we believe it incorrect. In the region 20-26 MeV 7 new channels open up including (n,^{6}Li)^{7}Li. But since Axton extrapolated such small cross sections for channels such as (n, np), (n, p), and (n, d) beyond 20 MeV, he assigned a large cross section to the (unmeasured) ^{7}Li – ^{8}Li break up, to reproduce the total nonelastic cross section. Where we differ from Axton is mainly in the (n, p), (n, d), and (n, np) channels, which our calculations indicate to be far more important than he supposed. The importance of the first two of these comes directly from our preequilibrium calculations, which are supported by the UC-Davis data (Fig. 14). The large cross section for preequilibrium and direct proton and deuteron emission seen in Fig. 14 is the reason for the large (n, p) and (n, d) cross sections, since following a high-energy primary emission there is often insufficient energy left in the residual nucleus for secondary particle emission. Since the cross sections for primary proton and neutron decay are so significant, it is no surprise that (n, np) should also be important at these energies. Also, these large cross sections are consistent with the total production cross sections from UC-Davis, since our determination of these values gave numbers significantly higher than those obtained by Axton, as described above. Our results are also approximately consistent with the Brenner and Prael model calculations. For instance, in Ref. [17] Brenner and Prael quote a production cross section for $A = 11$ nuclei at 30 MeV of 131.3 mb.

We obtain 105 mb here, whereas the ENDF/B-VI evaluation gives only 31 mb.

To summarize, we quote Axton's comments on this situation and reiterate our solution. Regarding the "controversial ^{12}C(n,^{6}Li)^{7}Li reaction, with its 100 mb", Axton stated (Axton [8], p. 27) that "If the reaction is eliminated, another home has to be found for this 100 mb at 26 MeV. There appears to be nowhere to go without conflicting with the available evidence upon which the evaluated cross sections are based." The "available evidence" here is, primarily, Axton's values for the UC-Davis total production cross sections of protons and deuterons. But since we have argued that his extrapolated values here are too small, we have opened up the possibility for more cross section to deuteron and proton emission. In particular, we have shown that cross section to the ^{12}C(n,^{6}Li)^{7}Li reaction can be completely ignored, and reassigned mainly to the (n,np), (n,p), and (n,d) channels, without any inconsistencies. This is certainly what our calculations indicate. Moreover we noted that the UC-Davis emission spectra themselves support significant cross section to these channels, due to the observed importance of preequilibrium proton and deuteron emission.

7.2.3 Kerma factors

Between 20 and 25 MeV the Axton ENDF/B-VI kerma evaluation agrees fairly well with our evaluation and with experimental measurements. But above 25 MeV his total kerma is higher than most of the experimental measurements and model calculations, as seen in Fig. 27.

The lower kerma factor that we obtain compared to the ENDF/B-VI evaluation is due, in part, to the above differences in cross sections. For instance, at 27 MeV over 10 % of the total kerma comes from the controversial ^{12}C(n,^{6}Li)^{7}Li channel. In all of Axton's kerma calculations he assumes that residual nuclei are produced in their ground states, which tends to overestimate the calculated kerma (Axton assessed that the overestimate is about 2.5% at 28 MeV).

In addition to the above differences, we think that the procedure used by Axton to determine energy depositions gives an overestimate for the alpha average-energy, and hence the alpha kerma factor. This can be shown by considering the situation at 27 MeV, where there are alpha production spectrum measurements from UC-Davis and Los Alamos, and a $(n,n'3\alpha)$ alpha spectrum measurement by Antolkovic *et al.* [37]. Here Axton's evaluation is consistent with the Antolkovic measurement, but inconsistent with the Los Alamos and UC-Davis results.

At 27 MeV, Axton's evaluation for the (n,α) and $(n,n'3\alpha)$ cross sections are 7 and 254 mb respectively, while we obtain 5 and 252 mb respectively (in close agreement). The partial kerma factors for these two exclusive reactions obtained by Axton are 0.13 and 2.84 f Gy m^2 respectively, and other reactions involving alphas are small and can be omitted here. We want to convert these results into inclusive alpha production

kerma, to compare them with our results and with the UC-Davis measurement. In the case of $(n, n'3\alpha)$ there is no heavy recoil, but for the (n, α) reaction only a fraction of the 0.13 f Gy m^2 kerma will go to the alpha, the rest going to the ^{9}Be recoil. Still, we can approximately say that the Axton evaluation predicts an alpha production inclusive kerma factor in the range 2.84-2.97 f Gy m^2. However, our calculations show an inclusive partial kerma factor to alphas of 1.97 f Gy m^2, in reasonable agreement with the UC-Davis measurement [78] of 2.11 f Gy m^2. This is to be expected since in Fig. 14 it is evident that our calculated spectral shape agrees with the Los Alamos and UC-Davis experimental data. The fact that the Axton partial kerma to alphas is so much higher indicates that his evaluated alpha emission spectrum must be too hard.

We note, though, that another experimental measurement by Antolkovic [24] gives a larger partial kerma to the $(n, n'3\alpha)$ channel, in closer agreement to the Axton evaluation. However, the uncertainties in this emulsion experiment are large (as indicated by the large reported error-bars [24]). Since the direct measurements of the alpha spectrum from Los Alamos and UC-Davis are in close agreement, and are consistent also with the Brenner and Prael and the present Livermore calculations, we think the Antolkovic result is too high. For instance, the 26 MeV neutron-induced differential emission spectrum of alphas shown in Fig. ? of Antolkovic's paper [37] shows a large excess of low-energy alphas compared to the UC-Davis and Los Alamos measurements at 27 MeV. The fact that the latter two measurements are of inclusive alpha production, while the former is just for the $(n, n'3\alpha)$ meachanism does not invalidate the comparison, since the ^{12}C$(n, \alpha)^9$Be contribution to alpha production only effects the spectrum at high-energies.

In summary, we believe that the Axton ENDF/B-VI total kerma factor evaluation in the region 26-32 MeV is too high for the following reasons: (1) the alpha emission spectrum shape is too hard, being inconsistent with the UC-Davis and Los Alamos measurements at 27.4 MeV; (2) unjustified reaction channels (in our view) such as ^{12}C$(n,^6$Li$)^7$Li and Axton's "spare" cross section result in kerma factors that are too high; and (3) the assumption that residual nuclei are produced in their ground states leads to a small overestimate.

7.3 Comparison With Experimental Measurements

7.3.1 Comparison with $(n, n'3\alpha)$ measurements

The partial cross section for the $(n, n'3\alpha)$ reaction is shown in Fig. 28, compared with the emulsion measurements by Antolkovic [24] with the Brenner and Prael corrections [110]. The good agreement that is seen between our calculations and the measurements is important since this reaction channel makes up such a large fraction of the

total nonelastic cross section. Our calculation of this channel agrees with the data better than that of Brenner and Prael [41], which lies below the measurements. This is the main reason for the fact that our total nonelastic cross section at 20 MeV is 7 % higher than Brenner and Prael's [41]. The Antolkovic measurement also provided information on the extent to which the $(n, n'3\alpha)$ reaction proceeds via the ground-state of ^{8}Be. Antolkovic concluded that this fraction ranged from about 0.3 at 20 MeV to about 0.2 at 35 MeV, with the rest of the reaction flux passing mainly through the first excited state (2.9 MeV). Over this energy range our calculation yields fractions 0.56 to 0.26. Such differences are not surprising given the assumptions inherent in our statistical model calculations. The practical consequences of these differences are minor, though, since they would result in small changes to the shape our alpha production spectra at very low energies, where the contribution to the kerma is small.

7.3.2 Comparison with $(n, 2n)$ measurements

Experimental data also exists for the $(n, 2n)$ reaction channel. There are a number of measurements below 34 MeV [111, 112, 113, 115] in addition to the (old) measurement at 90 MeV by Mcmillan and York [114]. Our calculated cross section is approximately two times smaller than these measurements. Fortunately the small cross section to this channel means that these differences do not have a large impact on our evaluation neutron production spectra. The decrease in the calculation from 60-70 MeV is due to the fact that our evaluated primary preequilibrium spectra show an increase in proton emission here, since we attempted to improve the agreement with the Louvain-la-Neuve proton emission data at 73 MeV. At the higher energies it is the emission of two high-energy neutrons in direct knockout-type processes that produce ^{11}C nuclei in the $(n, 2n)$ reaction. This mechanism is included in our calculations using our multiple preequilibrium (MPE) model. The failure of our calculation here is linked to our modeling of such processes, along with the relative emission of neutrons and protons. But the general success of our modeling for other (more important) decay channels, along with the fact that our MPE model has worked well in many other analyses [43, 65], makes us reluctant to adjust calculation parameters to try to improve our $(n, 2n)$ calculation.

7.3.3 Comparison with (n, n') measurements

In Figures 30 and 31 we show our calculated coupled-channels inelastic scattering to the 2+ (4.4 MeV) and 3- (9.6 MeV) states in carbon, compared with measurements. Scattering to the 4.4 MeV state is followed by gamma decay to the ground state, whereas the 9.6 MeV state decays by alpha emission. We include in Fig. 31 the Antolkovic [24] kinematically-complete nuclear emulsion experimental results for the

$^{12}C(n,n'3\alpha)$ reaction via the 3– state. Since the probability for the break-up of the 3– state into 3α is 0.99, these cross sections are equivalent to those measured directly in the neutron inelastic scattering experiments at Ohio and Uppsala Universities. We also show experimental data from proton inelastic scattering, which should be similar to the neutron values at these energies (these angle-integrated values were taken from Meigooni's thesis [87]). The various experimental measurements are fairly consistent with each other, and our calculations describe them well.

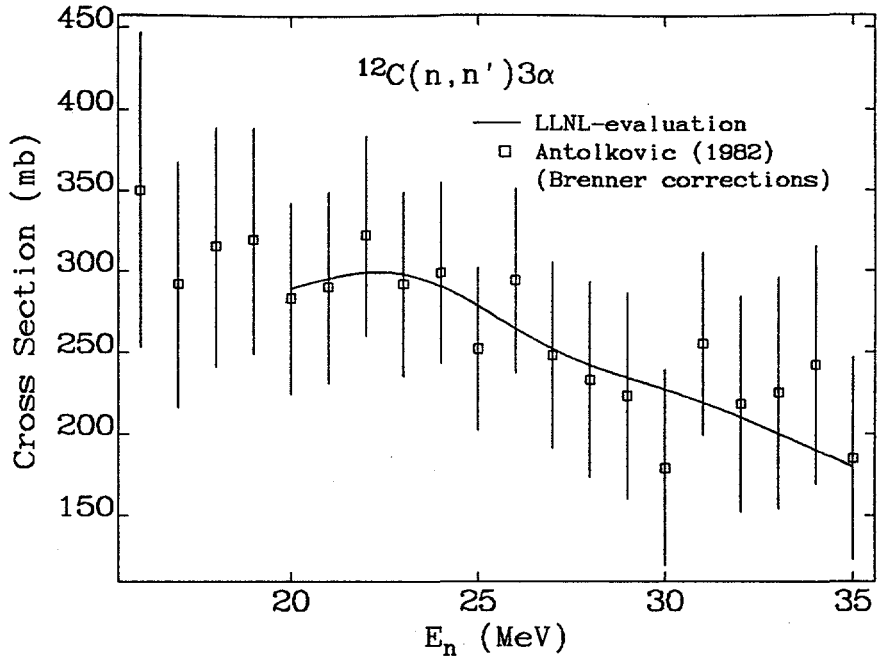

Figure 28: Calculated $(n, n'3\alpha)$ cross section compared to experimental measurements [24, 110]

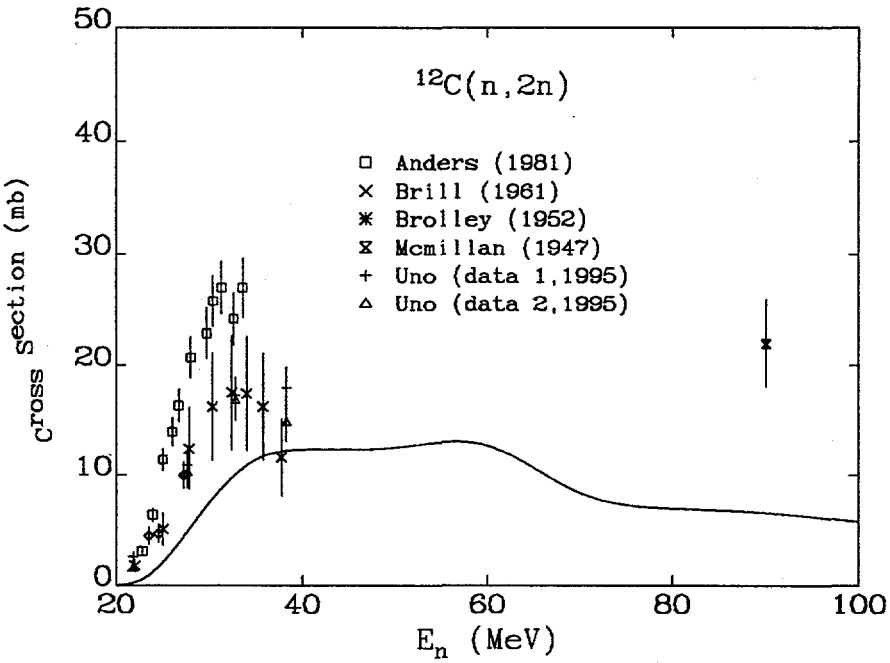

Figure 29: Calculated $(n, 2n)$ cross section compared to experimental measurements [111, 112, 113, 114]

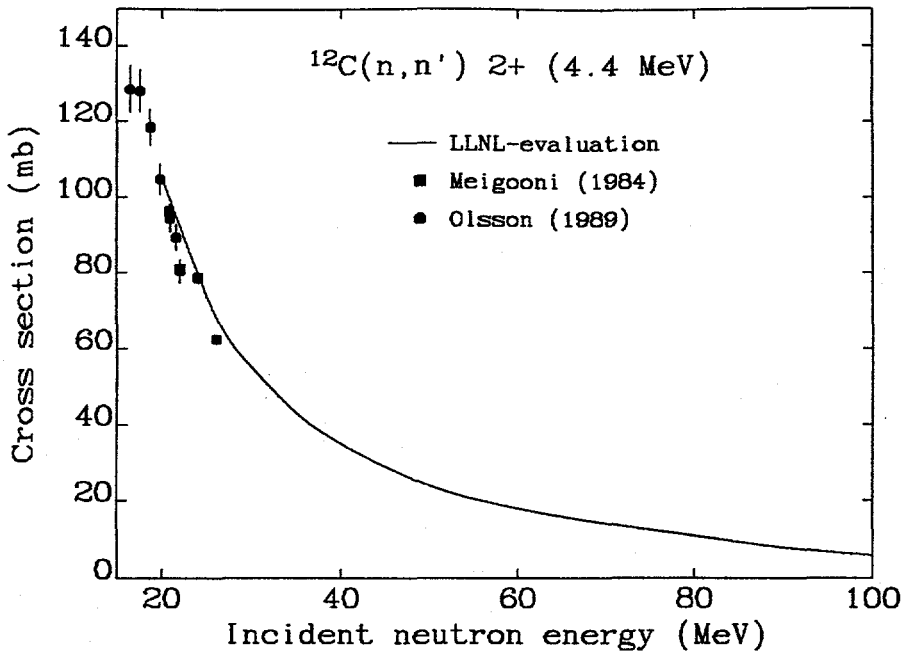

Figure 30: Angle-integrated inelastic scattering to the 2+ (4.4 MeV) state compared with measurements [81, 80]

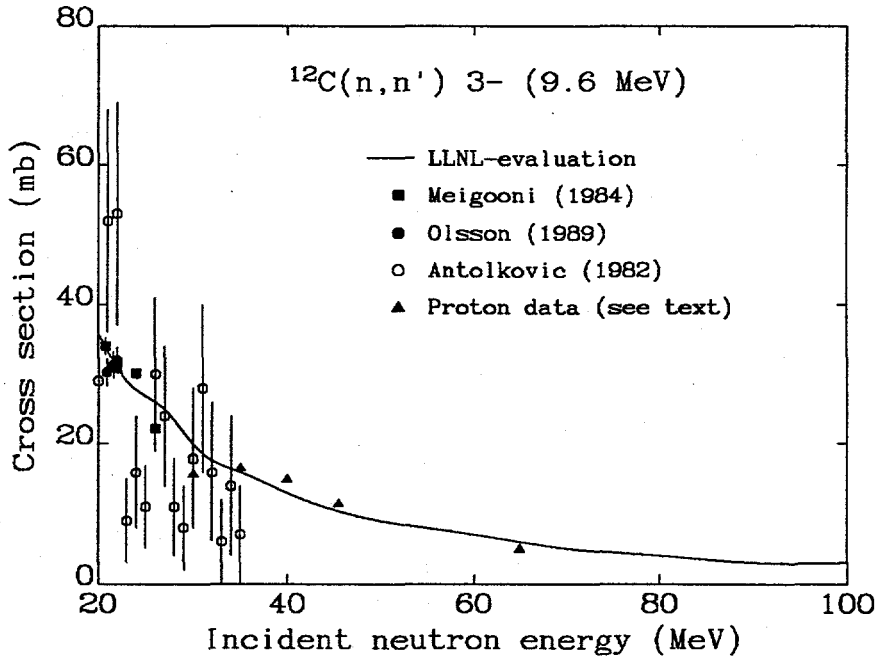

Figure 31: Angle-integrated inelastic scattering to the 3- (9.6 MeV) state compared with measurements [81, 80, 24]

8 Conclusions

We have produced an evaluated nuclear data base for neutrons incident on carbon with energies up to 100 MeV, and matched it to the existing ENDL carbon library at 20 MeV. This is the first step in a program being carried out at Lawrence Livermore National Laboratory to produce evaluated data files for biologically-important elements, for use in neutron and proton therapy applications. The evaluation rests upon recent cross section measurements from Louvain-la-Neuve, Los Alamos, and UC-Davis, and new nuclear modeling capabilities we have developed for high-energy reactions, particularly in the preequilibrium, direct, level density, and optical model calculations.

We have extensively benchmarked our results to experimental measurements of total production cross sections, emission spectra, and angular distributions, and obtained an excellent representation of these measurements. Our coupled-channel optical model analysis provides a good description of the total, elastic, and reaction cross sections, as well as measured neutron and proton elastic scattering angular distributions. The evaluated total cross section has an uncertainty of less than 1%, while that of the reaction cross section is about 5% at the lower energies, increasing to about 10% at 100 MeV. Our evaluated emission spectra, which come from our model calculations of Hauser-Feshbach, preequilibrium, and direct reaction processes, compare well with the measurements where they exist.

We have also devoted particular attention to ensuring that our evaluation is consistent with measured kerma factors. We have achieved a good description of experimental partial kerma factors for elastic scattering and inelastic charged-particle emission, with one notable exception: the 72.8 MeV proton emission data from Louvain-la-Neuve. Here our model calculations were unable to account for the large measured proton cross section, due to theoretical restrictions arising from flux conservation and known systematics for the relative amounts of preequilibrium neutron and proton emission. This resulted in our evaluated total kerma factor agreeing well with the various experimental measurements in most cases, but underpredicting the Louvain-la-Neuve result at 72.8 MeV. However, unfortunately the status of the experimental total kerma factor measurements above 50 MeV remains somewhat unclear, since the direct measurements are systematically lower than those inferred from the UC-Davis and Louvain-la-Neuve cross sections. Our evaluated total kerma factor lies in between experimental results from these two types of measurements.

We have compared our cross section and kerma calculations with the results from other analyses. The two previous works which have presented the most detailed comparisons with cross section measurements are those by Brenner and Prael [17], and Dimbylow [34]. Compared to Brenner and Prael's calculated cross sections, ours generally agree more closely with the data for proton and deuteron emission, and

the quality is comparable for alpha emission. Additionally, our total kerma factor describes the existing experimental results somewhat better, though as mentioned above there are still some uncertainties in the experimental situation at the higher energies. Our total kerma factor is fairly similar to Dimbylow's, and our cross section calculations describe experimental emission spectra significantly better. Also, our work is suitable for direct use in radiation transport calculations since it contains details of all reaction processes which contribute significantly at these energies.

Since the libraries have been generated with the GNASH nuclear modeling code, it will be easy to update them when new experimental measurements (such as the 20-90 MeV data currently being measured by Baba *et al.* at JAERI [116]) and new modeling capabilities become available.

9 Acknowledgments

We wish to thank Drs. William Chandler, Christine Hartmann-Siantar, Robert Howerton, Jim Rathkopf, David Resler, and Roger White, for many useful discussions on experimental and evaluated cross sections and kerma factors, evaluated nuclear data formats, and the requirements of evaluated files for implementation in radiation transport applications. We acknowledge the useful guidance provided to this project by the LLNL Medical Applications Program Advisory Committee (Prof. Heinz Barschall, Dr. Anthony Carrano, Prof. Paul DeLuca, Jr., Prof. T. Rockwell Mackie, Prof. Richard Maughan, Prof. Daniel Miller, Prof. Lynn Verhey, Prof. Andre Wambersie, and Dr. Sandra Zink). We thank Prof. Juan Romero for useful discussions and for providing tabulations of the UC-Davis angle-integrated data. We also thank Prof. Jean-Pierre Meulders for making his angle-integrated charged-particle emission spectra from Louvain-la-Neuve available to us prior to publication. We thank Drs. Robert Haight, Tim Lee, and Steven Sterbenz, of Los Alamos, for numerous useful discussions and for providing us with experimental data prior to publication. We are also grateful to Profs. Mamoru Baba, Takashi Nakamura, and Hikonojo Orihara for providing us with unpublished data. We have benefitted from helpful discussions on nuclear reaction mechanisms and nuclear level densities with Drs. Frank Dietrich, Roger Finlay, Arthur Kerman, and Gianni Reffo. We are also grateful to Dr. R.T. Perry of Los Alamos for kindly providing detailed documentation of the LANL high-energy transport library calculations. Finally, we acknowledge useful discussions with Drs. S. Chiba and Y. Watanabe regarding the status of similar evaluation work being performed in Japan, and Dr. S. Pearlstein regarding his recent high-energy evaluation.

References

[1] R.M. White, M.B. Chadwick, C.L. Hartmann Siantar, W.P. Chandler, invited paper to the *Symposium on Nuclear Chemistry, American Chemical Society*, San Diego, March 14 (1994); Lawrence Livermore National laboratory document UCRL-JC-117412 (1994).

[2] R.M. White *et al.*, invited paper to the *Seventh Symposium on Neutron Dosimetry*, Berlin, Germany, October 14-18 (1992); Rad. Prot. Dos. **44**, 11 (1992).

[3] P.G. Young, E.D. Arthur, and M.B. Chadwick, Los Alamos National Laboratory document LA-MS-12343 (1992).

[4] M. Blann, Lawrence Livermore National Laboratory document UCRL-JC-109052 (1991).

[5] M.B. Chadwick, M. Blann, P.G. Young, and G. Reffo, in *Proccedings of the International Conference on Nuclear Data for Science and Technology*, Gatlinburg, Tennessee, May 9-13 1994, edited by K. Dickens (American Nuclear Society, 1994) p. 658.

[6] R.J. Howerton, Lawrence Livermore National Laboratory document UCRL-50400 **27** (1986)*revised.*

[7] R.M. White *et al.*, invited paper to the *Seventh Symposium on Neutron Dosimetry*, Berlin, Germany, October 14-18 (1992); Rad. Prot. Dos. **44**, 11 (1992).

[8] E.J. Axton, National Institute of Standards and Technology report NISTIR 4838 (1992).

[9] C.Y. Fu, E.J. Axton, and F.G. Perey, *Description of Evaluation for Natural Carbon Performed for ENDF/B-VI*, Oak Ridge National Laboratory (1989); *Evaluated Data for 0-32 MeV neutrons on elemental carbon*, Oak Ridge National Laboratory (1989).

[10] D.G. Brenner and R.E. Prael, At. Data and Nucl. Data Tables **41**, 71 (1989).

[11] S. Pearlstein, Health Physics **65**, 185 (1993); See also Pearlstein's high-energy ENDF/B-VI evaluation available from the Brookhaven NNDC.

[12] P.G. Young, E.D. Arthur, M. Bozoian, T.R. England, G.M. Hale, R.J. LaBauve, R.C. Little, R.E. MacFarlane, D.G. Madland, R.T. Perry, and W.B. Wilson, Los Alamos National Laboratory document LA-11753-MS (1990).

[13] A.J. Koning, Nuclear Energy Agency document NEA/NSC/DOC(93)6 (1993).

[14] J. Raynal, *ICTP*, Trieste (1971).

[15] O. Bersillon, Bruyeres-le-Chatel progress report CEA-N-2037, p. 111 (1978).

[16] M.B. Chadwick and P.G. Young, Phys. Rev. C **47**, 2225 (1993)

[17] T.S. Subramanian, J.L. Romero, F.P. Brady, J.W. Watson, D.H. Fitzgerald, R. Garrett, G.A. Needham, J.L. Ullmann, C.I. Zanelli, D.J. Brenner, and R.E. Prael, Phys. Rev. C **28**, 521 (1983).

[18] F.P. Brady and J.L. Romero, *Final Report to the National Cancer Institute*, University of California, Davis, (1979).

[19] I. Slypen, V. Corcalciuc, A. Ninane, and J.P. Meulders, Nucl. Instr. Methods in Phys. Res. A **337**, 431 (1994); I. Slypen, V. Corcalciuc, A. Ninane, and J.P. Meulders, Phys. Med. Biol. **40**, 73 (1995); I. Slypen, V. Corcalciuc, and J.P. Meulders, Phys. Rev. C **51**, 1303 (1995).

[20] R. Haight, S. Sterbenz, T. Lee, in *Proccedings of the International Conference on Nuclear Data for Science and Technology*, Gatlinburg, Tennessee, May 9-13 1994, edited by K. Dickens (American Nuclear Society, 1994) p. 311.

[21] See experimental data shown in Fig. 30 of Ref. [12].

[22] F.E. Bertrand and R.W. Peelle, Phys. Rev. C **8**, 1045 (1973).

[23] R.W. Finlay, W.P. Abfalterer, G. Fink, E. Montei, T. Adami, P.W. Lisowski, G.L. Morgan, and R.C. Haight, Phys. Rev. C **47**, 237 (1993)

[24] B. Antolkovic, I. Slaus, D. Plenkovic, P. Macq, and J.P. Meulders, Nucl. Phys. **A394**, 87 (1983); B. Antolkovic, M. Turk, and K. Kadija, in *Nuclear Data for Basic and Applied Sciences*, Santa Fe, New Mexico, 13-17 May, 1985, edited by P.G. Young (Gordon and Breach, 1986), p. 183.

[25] G.H. Harrison *et al.*, in *Proc. 8th Symposium in Microsdosimetry*, 27 Sept. - 1 Oct. 1982, Julich, Germany (Commission of European Communities, Luxembourg, 1983) p. 325.

[26] J.L. Romero, private communication (1994).

[27] R.C. Haight, S. Sterbenz, T. Lee, private communication (1994).

[28] J.P. Meulders, private communication (1994).

[29] C. Kalbach, Phys. Rev. C **37**, 2350 (1988).

[30] R.G. Alsmiller Jr., and J. Barish, Health Physics **33**, 98 (1977).

[31] M.A. Behrooz and D.E. Watt, in *Proc. 4th Symp. on Neutron Dosimetry,* EUR-7448 (Luxembourg, CEC) 353-360 (1981).

[32] K. Morstin, A. Dydejczyk, and J. Booz, Rad. Prot. Dos. **23**, 35 (1988).

[33] A.H. Wells, Radiat. Res. **80**, 1 (1979).

[34] P.J. Dimbylow, Phys. Med. Biol. **27**, 989 (1992).

[35] G.H. Herling, R.H. Bassel, J.H. Adams, and W.A. Frazer, Naval Research Report 8441, Washington, D.C., (1981).

[36] Y. Watanabe *et al.*, M.B. Chadwick, M. Blann, P.G. Young, and G. Reffo, in *Proccedings of the International Conference on Nuclear Data for Science and Technology*, Gatlinburg, Tennessee, May 9-13, 1994, edited by K. Dickens (American Nuclear Society, in press).

[37] B. Antolkovic, I. Slaus, and D. Plenkovic, Radiat. Res. **97**, 253 (1984).

[38] R.S. Cawsell, J.J. Coyne, M.L. Randolph, Radiat. Res. **83**, 217 (1980).

[39] U.J. Schrewe, H. J. Brede, S. Gerdung, R. Nolte, P. Pihet, P. Schmelzbach, and H. Schuhmacher, Rad. Prot. Dos. **44**, 21 (1992).

[40] U.J. Schrewe, W.D. Newhauser, H. J. Brede, V. Dangendorf, P.M. DeLuca, Jr., S. Gerdung, R. Nolte, P. Schmelzbach, H. Schuhmacher, and T. Lim, in Chalk River Conference, 1994, to be published in Rad. Prot. Dos.

[41] D.G. Brenner and R.E. Prael, in *Nuclear and Atomic Data for Radiotherapy and Related Radiobiology*, ed. K. Okamoto (IAEA, Vienna, 1985) p. 205.

[42] M. Blann, H. Gruppelaar, P. Nagel, and J. Rodens, Nuclear Energy Agency of the OECD (OECD, Paris, 1994).

[43] M.B. Chadwick, P.G. Young, D.C. George, and Y. Watanabe, Phys. Rev. C **50**, 996 (1994).

[44] M.B. Chadwick, P.G. Young, P. Oblozinsky, Phys. Rev. C **49**, R2885 (1994).

[45] H. Feshbach, A. Kerman, and S. Koonin, Ann. Phys. (N.Y.) **125**, 429 (1980).

[46] M.B. Chadwick and P.G. Young, invited paper to the *Symposium on Nuclear Data Evaluation Methodology*, Brookhaven National Laboratory, Upton, New York, 12-16 October (1992), edited by C.L. Dunford (World Scientific, Singapore, 1993), p.424.

[47] M.B. Chadwick and P.G. Young, invited paper to the *Workshop on Simulating Accelerator Radiation Environments*, Santa Fe, New Mexico, 11-15 January 1993 (World Scientific, in press); Lawrence Livermore National Laboratory document UCRL-JC-113412 (1993).

[48] M.B. Chadwick, P.G. Young, and F.S. Dietrich, invited paper to the *Specialist Meeting on Intermediate Energy Nuclear Data*, organized by the Nuclear Energy Agency of the OECD, Paris, May 30 - June 1 1994 (OECD document, in press).

[49] P.E. Hodgson and M.B. Chadwick, invited paper to the *International Conference on Nuclear Data for Science and Technology*, Gatlinburg, Tennessee, May 9-13 1994, edited by K. Dickens (American Nuclear Society, in press).

[50] R.L. Bach and R.S. Caswell, Rad. Res. **35**, 1 (1968).

[51] A.S. Meigooni, R.W. Finlay, J.S. Petler, and J.P. Delaroche, Nucl. Phys. **A445**, 305 (1995).

[52] E.D. Arthur, Los Alamos National Laboratory progress report LA-9841-PR (1983).

[53] P.J. Dimbylow, Phys. Med. Biol. **25**, 637 (1980).

[54] A.M. Lane, Phys. Rev. Lett. **8**, 171 (1962); Nucl. Phys. **35**, 676 (1962).

[55] D.G. Madland, in *Proceedings of a Specialists' Meeting on Preequilibrium Reactions*, Semering, Austria, 10-12 Feb. 1988, edited by B. Strhmaier (NEA Report NEANDC-245, 1988) p. 103.

[56] S. Watanabe, Nucl. Phys. **8**, 484 (1958).

[57] F.C. Williams, Nucl. Phys. **A166**, 231 (1971); E. Betak and J. Dobes, Z. Phys. A **279**, 319 (1976).

[58] H. Gruppelaar, in *IAEA Advisory Group Meeting on Basic and Applied Problems on Nuclear Level Densities*, edited by M.R. Bhat (Brookhaven National Laboratory report, 1983), p. 143.

[59] P.D. Kunz, DWUCK4 code, University of Colorado (unpublished).

[60] M.B. Chadwick and P.G. Young, Los Alamos National Laboratory document LA-UR-93-104 (1993).

[61] Y. Watanabe, A. Aoto, H. Kashimoto, S. Chiba, T. Fukahori, M. Mizumoto, S. Meigo, M. Sugimoto, Y. Yamanouti, N. Koori, M.B. Chadwick, and P.E. Hodgson, submitted to Phys. Rev. C (1994); and in proceedings of the *International Conference on Nuclear Data for Science and Technology*, Gatlinburg, Tennessee, May 9-13 1994, edited by K. Dickens (American Nuclear Society, in press).

[62] P. Demetriou, P. Kanjanarat, and P.E. Hodgson, in proceedings of the *International Conference on Nuclear Data for Science and Technology*, Gatlinburg, Tennessee, May 9-13 1994, edited by K. Dickens (American Nuclear Society, in press).

[63] P.G. Young and M.B. Chadwick, invited paper to the *Specialist Meeting on Intermediate Energy Nuclear Data*, organized by the Nuclear Energy Agency of the OECD, Paris, May 30 - June 1 1994 (OECD document, in press).

[64] H. Vonach, A. Pavlik, M.B. Chadwick, R.C. Haight, R.O. Nelson, S.A. Wender, and P.G. Young, Phys. Rev. C **50**, 1952 (1994).

[65] M.B. Chadwick and P.G. Young, Lawrence Livermore National Laboratory document UCRL-JC-?? (1994). (MPE report)

[66] C. Kalbach, Z. Phys. **A 283**, 401 (1977).

[67] A.M. Kalend *et al.*, Phys. Rev. C **28**, 105 (1983).

[68] M. Blann and H. Vonach, Phys. Rev. C **28**, 1475 (1983).

[69] A.V. Ignatyuk, G.N. Smirenkin, and A.S. Tishin, Sov. J. Nucl. Phys. **21**, 255 (1975).

[70] A.H. Wapstra and K. Bos, At. Data and Nucl. Data Tables **19**, 175 (1977).

[71] R. Howerton, private communication (1994).

[72] F. Ajzenberg-Selove, Nucl. Phys. **A490**, 1 (1988); Nucl. Phys. **A506**, 1 (1990).

[73] J. Kopecky and M. Uhl, Phys. Rev. C **41**, 1941 (1990).

[74] D.M. Brink, D. Phil. thesis, Oxford University (1955).

[75] E.G. Fuller, Physics Reports **127**, 185 (1985).

[76] J. Ahrens *et al.*, Nucl. Phys. **A251**, 479 (1975).

[77] M.B. Chadwick and P. Oblozinsky, Phys. Rev. C ? (1994).

[78] J.L. Romero, F.P. Brady, and T.S. Subramanian, in *Nuclear Data for Basic and Applied Sciences*, Santa Fe, New Mexico, 13-17 May, 1985, edited by P.G. Young (Gordon and Breach, 1986) p. 687.

[79] R. MacFarlane, private communication (1994).

[80] N. Olsson, B. Trostell, and E. Ramstrom, Phys. Med. Biol. **34**, 909 (1989).

[81] A.S. Meigooni, J.S. Petler, and R.W. Finlay, Phys. Med. Biol. **29**, 643 (1984).

[82] R.P. Devito, Ph.D. thesis, Michigan State University (unpublished) (1979).

[83] E.L. Hjort, F.P. Brady, J.L. Romero, J.R. Drummond, D.S. Sorenson, J.H. Osborne, B. McEachern, and L.F.Hansen, Phys. Rev. C **50**, 275 (1994).

[84] Y. Yamanouti, M. Sugimoto,S. Chiba, M. Mizumoto, K. Hasegawa, and Y. Watanabe, in *Nuclear Data for Science and Technology*, May 13-17, 1991, Julich, Germany, edited by S. Qaim (Springer-Verlag, 1992), p. 717.

[85] F. Boreli, B.B. Kinsey, and P.N. Shrivastava, Phyical Review **174**, 1147 (1968).

[86] H. Orihara, private communication to MBC (1995); T. Niizeki, H. Orihara, K. Ishii, K. Maeda, M. Kabasawa, Y. Takahashi, K. Miura, Nucl. Instr. Meth. **A287**, 455 (1990).

[87] A.S. Meigooni, Ph.D. thesis, Ohio University (1984).

[88] R. De Leo, G. D'Erasmo, A. Pantaleo, M.N. Harakeh, E. Cereda, S. Micheletti, and M. Pignanelli, Phys. Rev. C**28**, 1443 (1983).

[89] E.L. Petersen, I. Slaus, J.W. Verba, R.F. Carlson, and J.R. Richardson, Nucl. Phys. **A102**, 145 (1967).

[90] S. Kato *et al.*, Nucl. Instr. Meth. **169**, 589 (1980).

[91] J. Dejuren and N. Knable, Phys. Rev. **77**, 606 (1950).

[92] M.H. Macgregor, W.P. Ball, and R. Booth, Phys. Rev. **111**, 1155 (1958).

[93] D.A. Kellogg, Phys. Rev. **99**, 224 (1958).

[94] R.G.P. Voss and R. Wilson, Proc. Royal Soc. **A236**, 41 (1956).

[95] C.I. Zanelli, P.P. Urone, J.L. Romero, F.P. Brady, M.L. Johnson, G.A. Needham, J.L. Ullmann, and D.L. Johnson, Phys. Rev. C **23**, 1015 (1981).

[96] D.A. Kellogg, Phys. Rev. **90**, 224 (1953).

[97] R. Nelson, private communication (1994); R. Nelson and S. Wender, in *Proccedings of the International Conference on Nuclear Data for Science and Technology*, Gatlinburg, Tennessee, May 9-13, 1994, edited by K. Dickens (American Nuclear Society, in press).

[98] P.M. DeLuca Jr., H.H. Barschall, M. Burhoe, and R.C. Haight, Nucl. Sci. Eng. **94**, 192 (1986).

[99] C.L. Hartmann, P.M. DeLuca Jr., and D.W. Pearson, Radiat. Prot. Dosim. **44**, 25 (1992).

[100] P. Pihet, S. Guldbakke, H.G. Menzel, and H. Schuhmacher, submitted to Phys. Med. Biol. (1992).

[101] P.J. Binns and J.H. Hough, NAC Annual Report. Technical Report NAC/AR/90-01 (National Accelerator Center, Faure, RSA), (June 1990).

[102] G. Buhler, H. Menzel, H. Schuhmacher, and S. Guldbakke, in *Proc. of 5th. Symposium on Neutron Dosimetry*, EUR-9762 (Luxembourg: CEC) p. 309 (1985).

[103] P.M. DeLuca Jr., H.H. Barschall, R.C. Haight, and J.C. McDonald, Radiat. Res. **100**, 78 (1984).

[104] P.M. DeLuca Jr., H.H. Barschall, R.C. Haight, and J.C. McDonald, in *Proc. of 5th. Symposium on Neutron Dosimetry*, EUR-9762 (Luxembourg: CEC) p. 193 (1985).

[105] E. Goldberg, D.R. Slaughter, and R.H. Howell, Lawrence Livermore National Laboratory report UCID-17789 (1978).

[106] R.C. Haight, S.M. Grimes, R.G. Johnson, and H.H. Barshall, Nucl. Sci. Eng. **87**, 41 (1984).

[107] J.C. McDonald, Radiat. Res. **109**, 28 (1987).

[108] M.C. Schell, D.W. Pearson, P.M. DeLuca Jr., and R.C. Haight, Med. Phys. **17**, 1 (1990).

[109] C.S. Wuu and L.R. Milavickas, Med. Phys. **14**, 1007 (1987).

[110] D.J. Brenner and R. Prael, Nucl. Sci. Eng. **88**, 97 (1984).

[111] B. Anders, P. Herges, and W. Scobel, Z. Phys. **301**, 353 (1981).

[112] O.D. Brill, N.A. Vlasov, S.P. Kalinin, L.S. Sokolov, Sov. Phys. Dokl. **6**, 24 (1961).

[113] J.E. Brolley, J.L. Fowler, and L.K. Schlacks, Physical Review **88**, 618 (1952).

[114] E. McMillan and H. York, Physical Review **73**, 262 (1948).

[115] Y. Uno, Y. Uwamino, T.S. Soewarsono, and T. Nakamura, Nucl. Sci. Eng. (in print, 1995).

[116] M. Baba *et al.* in *Proccedings of the International Conference on Nuclear Data for Science and Technology*, Gatlinburg, Tennessee, May 9-13 1994, edited by K. Dickens (American Nuclear Society, 1994) p. 658.